Mass Ratios for $^{117,118,119}I$

A Thesis

Submitted to the Faculty of Graduate Studies

University of Manitoba

In partial fulfillment

of the requirements for the degree

Master of Science

by

Philip Peter Unger

Winnipeg, Manitoba, Canada

ISBN 0-315-99000-7

Name Philip P. Unger

Dissertation Abstracts International is arranged by broad, general subject categories. Please select the one subject which most nearly describes the content of your dissertation. Enter the corresponding four-digit code in the spaces provided.

PHYSICS / NUCLEAR

SUBJECT TERM

0610

SUBJECT CODE

UMI

Subject Categories

THE HUMANITIES AND SOCIAL SCIENCES

COMMUNICATIONS AND THE ARTS
Architecture 0729
Art History 0377
Cinema 0900
Dance 0378
Fine Arts 0357
Information Science 0723
Journalism 0391
Library Science 0399
Mass Communications 0708
Music 0413
Speech Communication 0459
Theater 0465

EDUCATION
General 0515
Administration 0514
Adult and Continuing 0516
Agricultural 0517
Art 0273
Bilingual and Multicultural 0282
Business 0688
Community College 0275
Curriculum and Instruction 0727
Early Childhood 0518
Elementary 0524
Finance 0277
Guidance and Counseling 0519
Health 0680
Higher 0745
History of 0520
Home Economics 0278
Industrial 0521
Language and Literature 0279
Mathematics 0280
Music 0522
Philosophy of 0998
Physical 0523
Psychology 0525
Reading 0535
Religious 0527
Sciences 0714
Secondary 0533
Social Sciences 0534
Sociology of 0340
Special 0529
Teacher Training 0530
Technology 0710
Tests and Measurements 0288
Vocational 0747

LANGUAGE, LITERATURE AND LINGUISTICS
Language
- General 0679
- Ancient 0289
- Linguistics 0290
- Modern 0291

Literature
- General 0401
- Classical 0294
- Comparative 0295
- Medieval 0297
- Modern 0298
- African 0316
- American 0591
- Asian 0305
- Canadian (English) 0352
- Canadian (French) 0355
- English 0593
- Germanic 0311
- Latin American 0312
- Middle Eastern 0315
- Romance 0313
- Slavic and East European 0314

PHILOSOPHY, RELIGION AND THEOLOGY
Philosophy 0422
Religion
- General 0318
- Biblical Studies 0321
- Clergy 0319
- History of 0320
- Philosophy of 0322

Theology 0469

SOCIAL SCIENCES
American Studies 0323
Anthropology
- Archaeology 0324
- Cultural 0326
- Physical 0327

Business Administration
- General 0310
- Accounting 0272
- Banking 0770
- Management 0454
- Marketing 0338

Canadian Studies 0385
Economics
- General 0501
- Agricultural 0503
- Commerce-Business 0505
- Finance 0508
- History 0509
- Labor 0510
- Theory 0511

Folklore 0358
Geography 0366
Gerontology 0351
History
- General 0578
- Ancient 0579
- Medieval 0581
- Modern 0582
- Black 0328
- African 0331
- Asia, Australia and Oceania 0332
- Canadian 0334
- European 0335
- Latin American 0336
- Middle Eastern 0333
- United States 0337

History of Science 0585
Law 0398
Political Science
- General 0615
- International Law and Relations 0616
- Public Administration 0617

Recreation 0814
Social Work 0452
Sociology
- General 0626
- Criminology and Penology ... 0627
- Demography 0938
- Ethnic and Racial Studies 0631
- Individual and Family Studies 0628
- Industrial and Labor Relations 0629
- Public and Social Welfare 0630
- Social Structure and Development 0700
- Theory and Methods 0344

Transportation 0709
Urban and Regional Planning 0999
Women's Studies 0453

THE SCIENCES AND ENGINEERING

BIOLOGICAL SCIENCES
Agriculture
- General 0473
- Agronomy 0285
- Animal Culture and Nutrition 0475
- Animal Pathology 0476
- Food Science and Technology 0359
- Forestry and Wildlife 0478
- Plant Culture 0479
- Plant Pathology 0480
- Plant Physiology 0817
- Range Management 0777
- Wood Technology 0746

Biology
- General 0306
- Anatomy 0287
- Biostatistics 0308
- Botany 0309
- Cell 0379
- Ecology 0329
- Entomology 0353
- Genetics 0369
- Limnology 0793
- Microbiology 0410
- Molecular 0307
- Neuroscience 0317
- Oceanography 0416
- Physiology 0433
- Radiation 0821
- Veterinary Science 0778
- Zoology 0472

Biophysics
- General 0786
- Medical 0760

EARTH SCIENCES
Biogeochemistry 0425
Geochemistry 0996
Geodesy 0370
Geology 0372
Geophysics 0373
Hydrology 0388
Mineralogy 0411
Paleobotany 0345
Paleoecology 0426
Paleontology 0418
Paleozoology 0985
Palynology 0427
Physical Geography 0368
Physical Oceanography 0415

HEALTH AND ENVIRONMENTAL SCIENCES
Environmental Sciences 0768
Health Sciences
- General 0566
- Audiology 0300
- Chemotherapy 0992
- Dentistry 0567
- Education 0350
- Hospital Management 0769
- Human Development 0758
- Immunology 0982
- Medicine and Surgery 0564
- Mental Health 0347
- Nursing 0569
- Nutrition 0570
- Obstetrics and Gynecology .. 0380
- Occupational Health and Therapy 0354
- Ophthalmology 0381
- Pathology 0571
- Pharmacology 0419
- Pharmacy 0572
- Physical Therapy 0382
- Public Health 0573
- Radiology 0574
- Recreation 0575
- Speech Pathology 0460
- Toxicology 0383

Home Economics 0386

PHYSICAL SCIENCES
Pure Sciences
Chemistry
- General 0485
- Agricultural 0749
- Analytical 0486
- Biochemistry 0487
- Inorganic 0488
- Nuclear 0738
- Organic 0490
- Pharmaceutical 0491
- Physical 0494
- Polymer 0495
- Radiation 0754

Mathematics 0405
Physics
- General 0605
- Acoustics 0986
- Astronomy and Astrophysics 0606
- Atmospheric Science 0608
- Atomic 0748
- Electronics and Electricity 0607
- Elementary Particles and High Energy 0798
- Fluid and Plasma 0759
- Molecular 0609
- Nuclear 0610
- Optics 0752
- Radiation 0756
- Solid State 0611

Statistics 0463

Applied Sciences
Applied Mechanics 0346
Computer Science 0984
Engineering
- General 0537
- Aerospace 0538
- Agricultural 0539
- Automotive 0540
- Biomedical 0541
- Chemical 0542
- Civil 0543
- Electronics and Electrical 0544
- Heat and Thermodynamics ... 0348
- Hydraulic 0545
- Industrial 0546
- Marine 0547
- Materials Science 0794
- Mechanical 0548
- Metallurgy 0743
- Mining 0551
- Nuclear 0552
- Packaging 0549
- Petroleum 0765
- Sanitary and Municipal 0554
- System Science 0790

Geotechnology 0428
Operations Research 0796
Plastics Technology 0795
Textile Technology 0994

PSYCHOLOGY
General 0621
Behavioral 0384
Clinical 0622
Developmental 0620
Experimental 0623
Industrial 0624
Personality 0625
Physiological 0989
Psychobiology 0349
Psychometrics 0632
Social 0451

Nom _____

Dissertation Abstracts International est organisé en catégories de sujets. Veuillez s.v.p. choisir le sujet qui décrit le mieux votre thèse et inscrivez le code numérique approprié dans l'espace réservé ci-dessous.

_____ ☐☐☐ U·M·I

SUJET — CODE DE SUJET

Catégories par sujets

HUMANITÉS ET SCIENCES SOCIALES

COMMUNICATIONS ET LES ARTS
Architecture 0729
Beaux-arts 0357
Bibliothéconomie 0399
Cinéma 0900
Communication verbale 0459
Communications 0708
Danse 0378
Histoire de l'art 0377
Journalisme 0391
Musique 0413
Sciences de l'information 0723
Théâtre 0465

ÉDUCATION
Généralités 515
Administration 0514
Art 0273
Collèges communautaires 0275
Commerce 0688
Économie domestique 0278
Éducation permanente 0516
Éducation préscolaire 0518
Éducation sanitaire 0680
Enseignement agricole 0517
Enseignement bilingue et multiculturel 0282
Enseignement industriel 0521
Enseignement primaire. 0524
Enseignement professionnel 0747
Enseignement religieux 0527
Enseignement secondaire 0533
Enseignement spécial 0529
Enseignement supérieur 0745
Évaluation 0288
Finances 0277
Formation des enseignants 0530
Histoire de l'éducation 0520
Langues et littérature 0279
Lecture 0535
Mathématiques 0280
Musique 0522
Orientation et consultation 0519
Philosophie de l'éducation 0998
Physique 0523
Programmes d'études et enseignement 0727
Psychologie 0525
Sciences 0714
Sciences sociales 0534
Sociologie de l'éducation 0340
Technologie 0710

LANGUE, LITTÉRATURE ET LINGUISTIQUE
Langues
- Généralités 0679
- Anciennes 0289
- Linguistique 0290
- Modernes 0291

Littérature
- Généralités 0401
- Anciennes 0294
- Comparée 0295
- Médiévale 0297
- Moderne 0298
- Africaine 0316
- Américaine 0591
- Anglaise 0593
- Asiatique 0305
- Canadienne (Anglaise) 0352
- Canadienne (Française) 0355
- Germanique 0311
- Latino-américaine 0312
- Moyen-orientale 0315
- Romane 0313
- Slave et est-européenne 0314

PHILOSOPHIE, RELIGION ET THÉOLOGIE
Philosophie 0422
Religion
- Généralités 0318
- Clergé 0319
- Études bibliques 0321
- Histoire des religions 0320
- Philosophie de la religion 0322

Théologie 0469

SCIENCES SOCIALES
Anthropologie
- Archéologie 0324
- Culturelle 0326
- Physique 0327

Droit 0398
Économie
- Généralités 0501
- Commerce-Affaires 0505
- Économie agricole 0503
- Économie du travail 0510
- Finances 0508
- Histoire 0509
- Théorie 0511

Études américaines 0323
Études canadiennes 0385
Études féministes 0453
Folklore 0358
Géographie 0366
Gérontologie 0351
Gestion des affaires
- Généralités 0310
- Administration 0454
- Banques 0770
- Comptabilité 0272
- Marketing 0338

Histoire
- Histoire générale 0578
- Ancienne 0579
- Médiévale 0581
- Moderne 0582
- Histoire des noirs 0328
- Africaine 0331
- Canadienne 0334
- États-Unis 0337
- Européenne 0335
- Moyen-orientale 0333
- Latino-américaine 0336
- Asie, Australie et Océanie 0332

Histoire des sciences 0585
Loisirs 0814
Planification urbaine et régionale 0999
Science politique
- Généralités 0615
- Administration publique 0617
- Droit et relations internationales 0616

Sociologie
- Généralités 0626
- Aide et bien-être social 0630
- Criminologie et établissements pénitentiaires 0627
- Démographie 0938
- Études de l' individu et de la famille 0628
- Études des relations interethniques et des relations raciales 0631
- Structure et développement social 0700
- Théorie et méthodes. 0344
- Travail et relations industrielles 0629

Transports 0709
Travail social 0452

SCIENCES ET INGÉNIERIE

SCIENCES BIOLOGIQUES
Agriculture
- Généralités 0473
- Agronomie. 0285
- Alimentation et technologie alimentaire 0359
- Culture 0479
- Élevage et alimentation 0475
- Exploitation des pâturages 0777
- Pathologie animale 0476
- Pathologie végétale 0480
- Physiologie végétale 0817
- Sylviculture et faune 0478
- Technologie du bois 0746

Biologie
- Généralités 0306
- Anatomie 0287
- Biologie (Statistiques) 0308
- Biologie moléculaire 0307
- Botanique 0309
- Cellule 0379
- Écologie 0329
- Entomologie 0353
- Génétique 0369
- Limnologie 0793
- Microbiologie 0410
- Neurologie 0317
- Océanographie 0416
- Physiologie 0433
- Radiation 0821
- Science vétérinaire 0778
- Zoologie 0472

Biophysique
- Généralités 0786
- Medicale 0760

SCIENCES DE LA TERRE
Biogéochimie 0425
Géochimie 0996
Géodésie 0370
Géographie physique 0368
Géologie 0372
Géophysique 0373
Hydrologie 0388
Minéralogie 0411
Océanographie physique 0415
Paléobotanique 0345
Paléoécologie 0426
Paléontologie 0418
Paléozoologie 0985
Palynologie 0427

SCIENCES DE LA SANTÉ ET DE L'ENVIRONNEMENT
Économie domestique 0386
Sciences de l'environnement 0768
Sciences de la santé
- Généralités 0566
- Administration des hôpitaux 0769
- Alimentation et nutrition 0570
- Audiologie 0300
- Chimiothérapie 0992
- Dentisterie 0567
- Développement humain 0758
- Enseignement 0350
- Immunologie 0982
- Loisirs 0575
- Médecine du travail et thérapie 0354
- Médecine et chirurgie 0564
- Obstétrique et gynécologie 0380
- Ophtalmologie 0381
- Orthophonie 0460
- Pathologie 0571
- Pharmacie 0572
- Pharmacologie 0419
- Physiothérapie 0382
- Radiologie 0574
- Santé mentale 0347
- Santé publique 0573
- Soins infirmiers 0569
- Toxicologie 0383

SCIENCES PHYSIQUES
Sciences Pures
Chimie
- Généralités 0485
- Biochimie 487
- Chimie agricole 0749
- Chimie analytique 0486
- Chimie minérale 0488
- Chimie nucléaire 0738
- Chimie organique 0490
- Chimie pharmaceutique 0491
- Physique 0494
- PolymÈres 0495
- Radiation 0754

Mathématiques 0405
Physique
- Généralités 0605
- Acoustique 0986
- Astronomie et astrophysique 0606
- Électronique et électricité 0607
- Fluides et plasma 0759
- Météorologie 0608
- Optique 0752
- Particules (Physique nucléaire) 0798
- Physique atomique 0748
- Physique de l'état solide 0611
- Physique moléculaire 0609
- Physique nucléaire 0610
- Radiation 0756

Statistiques 0463

Sciences Appliqués Et Technologie
Informatique 0984
Ingénierie
- Généralités 0537
- Agricole 0539
- Automobile 0540
- Biomédicale 0541
- Chaleur et thermodynamique 0348
- Conditionnement (Emballage) 0549
- Génie aérospatial 0538
- Génie chimique 0542
- Génie civil 0543
- Génie électronique et électrique 0544
- Génie industriel 0546
- Génie mécanique 0548
- Génie nucléaire 0552
- Ingénierie des systèmes 0790
- Mécanique navale 0547
- Métallurgie 0743
- Science des matériaux 0794
- Technique du pétrole 0765
- Technique minière 0551
- Techniques sanitaires et municipales 0554
- Technologie hydraulique 0545

Mécanique appliquée 0346
Géotechnologie 0428
Matières plastiques (Technologie) 0795
Recherche opérationnelle 0796
Textiles et tissus (Technologie) 0794

PSYCHOLOGIE
Généralités 0621
Personnalité 0625
Psychobiologie 0349
Psychologie clinique 0622
Psychologie du comportement 0384
Psychologie du développement 0620
Psychologie expérimentale 0623
Psychologie industrielle 0624
Psychologie physiologique 0989
Psychologie sociale 0451
Psychométrie 0632

MASS RATIOS FOR $^{117,118,119}_{I}$

BY

PHILIP PETER UNGER

A Thesis submitted to the Faculty of Graduate Studies of the University of Manitoba in partial fulfillment of the requirements of the degree of

MASTER OF SCIENCE

Abstract

We have determined the mass ratios between neutron deficient isotopes of iodine using a mass spectrometric technique with the Chalk River Isotope Separator On-line (ISOL). The mass triplet ^{117}I -^{118}I -^{119}I has been studied. The measured mass ratios are in good agreement with systematics. Our results for the mass ratios are $M(^{117}\mathrm{I})/M(^{119}\mathrm{I})$ = 0.983 211 1 (13) and $M(^{118}\mathrm{I})/M(^{119}\mathrm{I})$ = 0.991 615 6 (12). The deduced masses of ^{117}I and ^{118}I are 116.913 69 (19) and 117.913 07 (17) u, respectively. We have used these measurements to study the local dependence of two particle separation energies on neutron number, and evaluate the predictive capabilities of several mass models. We have also determined that the accepted value for the transition energy for the isomeric decay of ^{118m}I is in error. This energy has been re-evaluated by a γ-ray measurement to be 114.24 (72) keV.

Acknowledgements

I would like to thank my supervisor, Dr. K.S. Sharma for his guidance and support during the course of this research. I would also like to thank Dr. R.C. Barber for his shared insight in the art of precise mass spectrometry.

I would like to extend special thanks to the professional and technical staff of the TASCC division and ISOL group at Chalk River Laboratories. In particular, Dr. E. Hagberg patiently guided me through the mass measurement program at CRL. Dr. J.C. Hardy, Dr. V. Koslowky, Dr. G. Savard, and Dr. H. Schmeing all contributed their time and experience toward the success of this experiment. The smooth operation of the isotope separator and the tandem accelerator is due to the efforts of Mr. M. Watson, Mr. W. Parry and the TASCC operations staff.

The support and comradeship of fellow students, Dr. J. Hykawy, Mr. J. Nxumalo, and Mr. K. Aarts at the University of Manitoba, has been invaluable. Our numerous discussions on technical matters did not expose the relative ignorance of a participant but taught us to think about, and solve problems as physicists.

This research has been supported by the Natural Sciences and Engineering Council of Canada and the University of Manitoba.

Table of Contents

1 Introduction

1.1 Understanding atomic masses

The mass of an atom is one of its most basic properties. Therefore, by studying atomic masses, we can develop an understanding of many atomic properties through the development of theories accounting for the origins of atomic mass.

Early studies of atomic masses by Aston in the 1920's, using mass spectrometry, showed that each nuclear species has a mass nearly equal to an integral number of the proton mass [As20]. From this observation came Aston's 'whole number rule' of atomic masses.

Upon further investigation, slight divergences from the 'whole number rule' for atomic masses became evident. Aston systematically investigated the divergences for several elements and invented the term 'packing fraction' to express the extent of the divergences.

$$\text{packing fraction} = \frac{\text{atomic mass} - \text{mass number}}{\text{mass number}} = \frac{M - A}{A} \tag{1.1}$$

A directly related description of these 'differences', is the binding energy expression given below. The atomic and nuclear binding energies of an atom, $E_{\text{atomic binding}}$ & $E_{\text{nuclear binding}}$, are given as the difference between the mass of an atom, M, and the mass sum of the constituent components

$$E_{\text{atomic binding}} + E_{\text{nuclear binding}} = [\, Z\, M(^1\text{p}) + Z\, M(\text{e}) + N\, M(^1\text{n})\,] - M(N,Z) \quad , \tag{1.2}$$

where Z, N are the proton and neutron numbers, $M(^1\text{p})$, $M(^1\text{n})$, $M(\text{e})$ the masses of a free proton, neutron, and electron. The portion of the equation in square brackets [ ] is analogous to Aston's 'whole number rule'. The masses of the proton, neutron and electron are given with respect to the mass standard, ^{12}C. Nuclear binding energies are much greater in magnitude (~10^4) than atomic binding energies. Both are positive.

Precise mass measurements provide crucial and direct information on the nuclear binding energies of equation (1.2), and indirectly, nuclear properties such as shell and deformation effects, range and the strength of nuclear forces.

Atomic mass data may be presented in a variety of ways. For example, the so-called mass parabola is shown in fig. 1.1. In this instance, the nuclear binding energies of atoms of the isobar $A = 119$ are plotted against proton number, Z. The nuclide at the bottom of the parabola is stable against radioactive decay. Nuclides on the sides of the parabola will radioactively decay. Mass models to describe the value of atomic masses, and consequently the shape of the mass-parabola, have been developed by several researches. These will be discussed shortly.

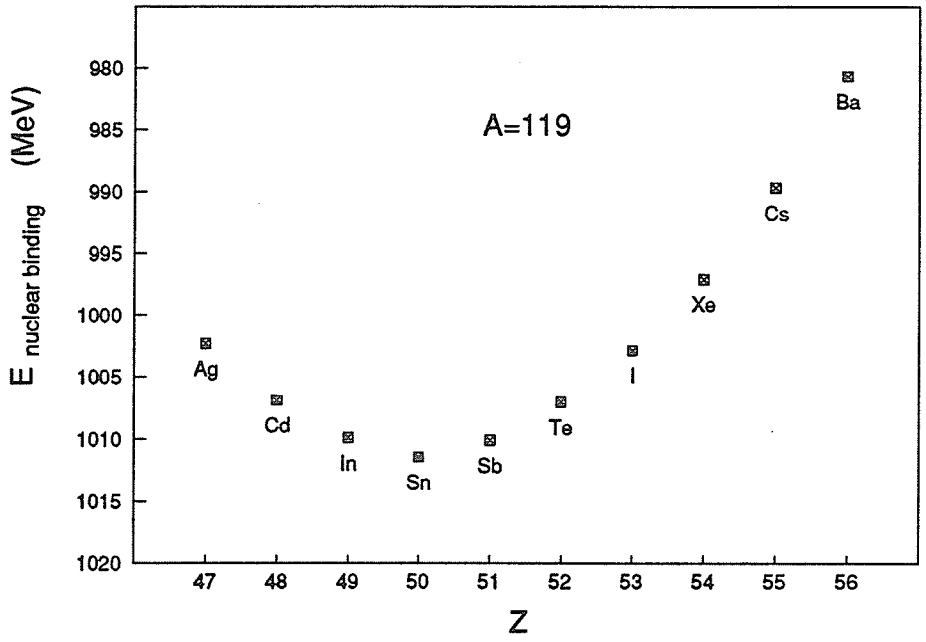

Fig. 1.1. The mass parabola for A = 119. All of the masses, except barium, have been determined experimentally. Several models have been constructed that describe the observed value of masses as well as predicting the mass of unmeasured exotic nuclei.

The nuclei of all isobars may be organized onto a "Chart of the Nuclides" (an arrangement such that the proton number is represented on the x-axis, and the neutron number is represented on the y-axis). The stable nuclides form the "backbone" of the Chart of the Nuclides. Conventional mass spectrometry has measured almost all of the stable nuclides that lie on the backbone. There are a large number of unstable nuclei that lie off the backbone. Most have not been mass spectrometerically analyzed, but this does not indicate a lack of interest on the part of the research community. Rather, it is testimony to the inherent difficulties of performing mass measurements in this region.

If we were to represent the mass of each nuclide on the z-axis on the Chart of Nuclides, we would obtain a so-called "mass surface". It is meaningful to split the mass surface into four different sheets because of the effects of nucleon pairing. The four sheets are comprised of even neutron-even proton, odd neutron-odd proton, even neutron-odd proton, and odd neutron-even proton nuclei. Detailed systematic studies of the mass difference between these four sheets directly reflects the neutron and proton pairing energies as well as the interaction between an odd neutron and an odd proton that originate from nuclear structure effects.

Evidence of nuclear deformations is obtained, for example, from the systematic behavior of double proton or neutron separation energies as a function of N and Z. In general, the separation energy curve decreases slowly with increasing nucleon number. A region of deformity is indicated by a change of slope, creating a broad hump. Shell closure is indicated by a discontinuity in the curve, that otherwise has the same slope on either side of the shell closure. An example of these features is given in fig. 1.2.

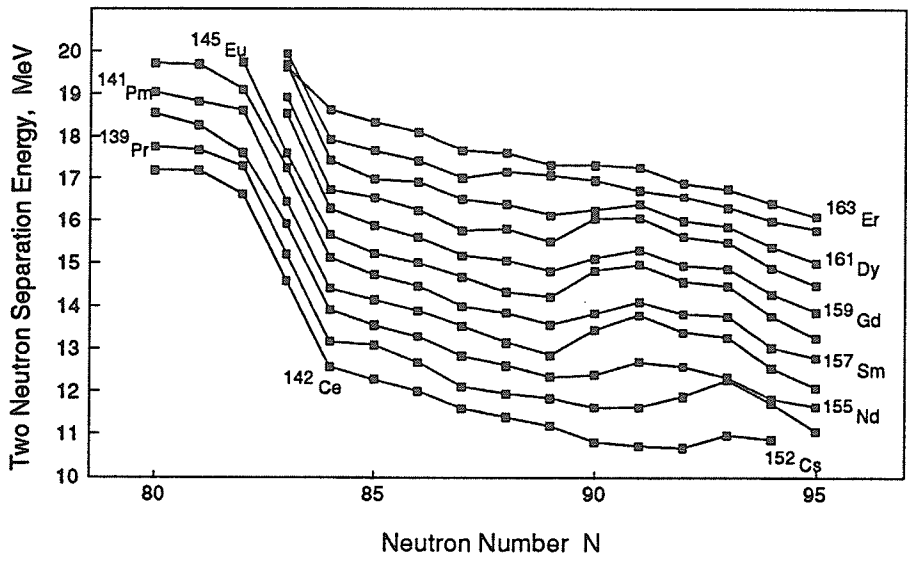

Fig. 1.2. Two neutron separation energies, $S_{2n} = -M(A,Z) + M(A-2,Z) + 2n$, plotted as a function of N in the range $80 \leq N \leq 95$. Isotopes of an element are connected by a line. The neutron shell closure at $N = 82$ is shown clearly. Also, the region around $N = 91$ shows the gradual change in slope that is associated with a region of deformation.

At a fundamental level, an understanding of atomic mass involves an understanding of the microscopic many-body dynamics involving nucleon-nucleon interactions. In principle then, the mass is determined by the general solutions of the many-body Hamiltonian for this system. This is beyond the present scope of physics, and approximations, assumptions, or models must be introduced for any practical purpose.

The models for mass predictions may be considered in the following groups: semi-emperical or phenomenological models, liquid drop or droplet models, mass models based on the shell model, and mass models based on mass relations. In general, mass formulae have become complicated and it is not uncommon for some to contain a fairly large number of parameters (i.e. 100's).

Once a mass model is proposed, a fit to the known masses is carried out. As long as one deals with known masses, a large number of parameters presents no difficulty, since with many parameters, one can always achieve a good fit. However, in the extrapolation to unknown masses there is a risk that the masses will behave in some unexpected way as we move away from the initial fitted region. Thus, precision mass measurements of nuclei far from stability are needed to critically test nuclear mass models.

In some cases, models provide the only knowledge of the mass of exotic species. Thus certain, important astrophysical processes, such as nucleosynthesis, must rely on mass models because the production and measurement of some exotic species far from stability is not possible with present day accelerator facilities.

1.2 Determining atomic masses experimentally

1.2.1 Methods

In general, there are two categories of experimental methods to determine atomic mass. The first category involves mass-spectrometric methods: deflection type mass spectrometers (e.g. Manitoba II at University of Manitoba and Chalk River ISOL), time-of-flight mass spectrometers (e.g. TOFI at LAMFP and SPEG at GANIL), and radio-frequency spectrometers or Penning Traps (CERN). The second category consists of energy measurements in certain nuclear reactions and nuclear decays. Included in this category are reaction energies ((n,γ), (n,p), etc.) as well as Q_α and Q_β measurements.

A reaction energy experiment determines the Q-value, or the energy threshold, of a reaction. Consider the (n, γ) reaction measurement (e.g. ^{204}Pb(n,γ)^{205}Pb [Hu83]). The energy of the emitted photon determines the neutron separation energy, which leads directly to the mass difference between the initial and final nuclei, except for corrections

involving the nuclear recoil. While the precision achieved with (n, γ) reaction measurements often rivals the precision of mass spectrometric measurements (< 100 eV) , the nuclei available to this type of study are close to the backbone of stable nuclei.

Further from stability, the most common method to determine the mass of unstable nuclei is to study the Q-value of their α- or ß-decays (e.g. ß: [Ke84], α: [Sc79][Pl81]). In these measurements, a β or α energy spectrum (usually coincident with a γ-ray of interest) is collected. In the case of a ß decay to the ground state of the daughter, the end point of the ß spectrum determines the mass difference between parent and daughter. Often the decay scheme of the nucleus studied must be known because ground state-ground state decay is not the only branch present. If it were known from the decay scheme that one or more γ-rays depopulates states fed by β decay in the daughter nucleus, the γ-ray energy sum must be included to completely determine the mass difference. This requirement is increasingly harder to satisfy for nuclides further from stability. On the other hand, it is more frequently the case in α decay that the ground state of the daughter is populated. The singular energy of the α spectrum then determines the mass difference between parent and daughter. Q_α measurements are typically more precise than $Q_ß$ measurements (< 30 keV and > 40 kev respectively) although they are not applicable to as many nuclei.

The commonly accepted masses of unstable and stable isotopes are usually determined by a combination of both mass-spectrometric (direct) measurements and nuclear reaction and decay energy measurements. The 1983 Atomic Mass Evaluation [Wa85] includes input data from both types of experiments to obtain adjusted mass values through a least squares adjustment.

1.2.2 Facilities

The two main requirements for a facility performing mass measurements of exotic nuclei are adequate production rates and mass resolution. The mass resolution is given by $\frac{\Delta M}{M}$ where M is the mass of the nuclei under study, and ΔM is the full width of the mass spectral peak at half maximum (FWHM). Sometimes instead of the resolution the resolving power of the instrument is quoted. This is simply $\frac{M}{\Delta M}$.

Early mass measurements of unstable nuclei were performed by two groups, both using deflection type mass spectrometers. Johnson et al. [B179] used a double direction-focusing mass spectrometer with a resolving power of 1,300 to measure neutron-rich rubidium and cesium isotopes. The Orsay group at CERN used a conventional spectrometer of Mattauch-Herzog type (i.e. focusing in energy and direction) to systematically measure short-lived alkali and alkali earth isotopes [Ep80]. This instrument, with a typical resolving power of 10^4, achieved a precision in the final mass values of parts per million.

The Chalk River mass measurement facility uses the Tandem Accelerator Super-Conducting Cyclotron (TASCC) together with the On-Line Isotope Separator (ISOL). In the TASCC energy range, compound nucleus, projectile fragmentation and deep-inelastic reactions occur and result in large isotopic distributions, including a rich variety of nuclei far from stability. The isotope separator routinely achieves a mass resolution of 2×10^{-4} and typical precision in the range of 1 ~ 2 ppm. The Chalk River isotope separator is currently the only separator in the world capable of directly measuring the masses of unstable nuclei. The mass range available to it is between 1 and 300.

There are three other facilities world-wide that are currently performing direct mass measurements on unstable nuclei. They are the Penning trap spectrometer (ISOLTRAP) at CERN in Europe, the Time-of-Flight-Isochronous (TOFI) recoil spectrometer at Los

Alomos Meson Physics Facility (LAMPF) in Los Alomos, U.S.A., and the time-of-flight recoil spectrometer, SPEG, at Grand Accelerateur National d'Ions Lourds (GANIL) in Caen, France.

The tandem Penning trap mass spectrometer represents the third generation mass spectrometer at CERN for directly measuring the mass of unstable nuclei. With the present instrument, ISOLTRAP, the mass of a stored charged particle is determined by its cyclotron frequency in a known magnetic field. The accuracy, at present, is typically 10^{-7} or 100 keV at $A = 100$. Beams are delivered to it from the on-line isotope separator ISOLDE, collected on a rhenium foil, re-ionized, and then introduced into the traps. This currently restricts the available nuclei to be studied to those that are easily surface ionizable. Future plans include positioning an intermediate trap to receive the ISOLDE beam directly, after which, the higher precision penning traps would follow. Essentially, all ISOLDE beams would then become accessible to mass determination.

A recoil time-of-flight-isochronous spectrometer (TOFI) is used for direct mass measurements of exotic light nuclei [Wo85,87]. The spectrometer relies on an isochronous design that directly correlates an ion's time-of-flight through the spectrometer with its mass-to-charge ratio. The mass-to-charge ratio is determined independently of the ion's velocity, so that a precise mass measurement requires only a precision measurement of the time-of-flight. To date, the instrument has measured neutron-rich isotopes from fluorine to iron. Typical mass resolution $\frac{\Delta M}{M}$ is about 3×10^{-4} (FWHM). Typical precision is in the range of 4 ~ 8 ppm.

The high-resolution energy-loss spectrometer SPEG together with the GANIL facility also directly measure the mass of exotic nuclei far from stability [Gi87]. The production of both neutron-rich and deficient nuclei are possible with the energy range available

at the GANIL facility. The spectrometer uses a time-of-flight technique. Isotopes in the region of low Z from boron to phosphorus have been measured with a mass resolution (FWHM) of 5×10^{-4}. Typical precision is in the range of 5 ~ 10 ppm.

1.3 The iodine masses

In this work, we have measured the mass ratio of the proton rich isotopes ^{117}I, ^{118}I, and ^{119}I ($Z = 53$, $N = 64$, 65, and 66 respectively).

A previous experiment to measure the $^{117\text{-}119}$I masses through a ß decay energy experiment was made by E. Beck et al. [Be70]. However, this experiment provided reliable mass data for the isotope ^{119}I only. The results for the other isotopes were not included in the world body of atomic masses [Wa85].

The masses of ^{117}I and ^{118}I are predicted by several models [Ha88]. The uncertainty associated with the predicted mass of ^{117}I is 400 μu (i.e. precision of 3.4 parts per million, ppm) and 216 μu (1.8 ppm) for ^{118}I [Wa88].

The measurement of the masses of some isotopes of iodine extends our systematic study of nuclear masses near the doubly magic ^{100}Sn. Our recent mass measurements near ^{100}Sn are shown in fig. 1.3.

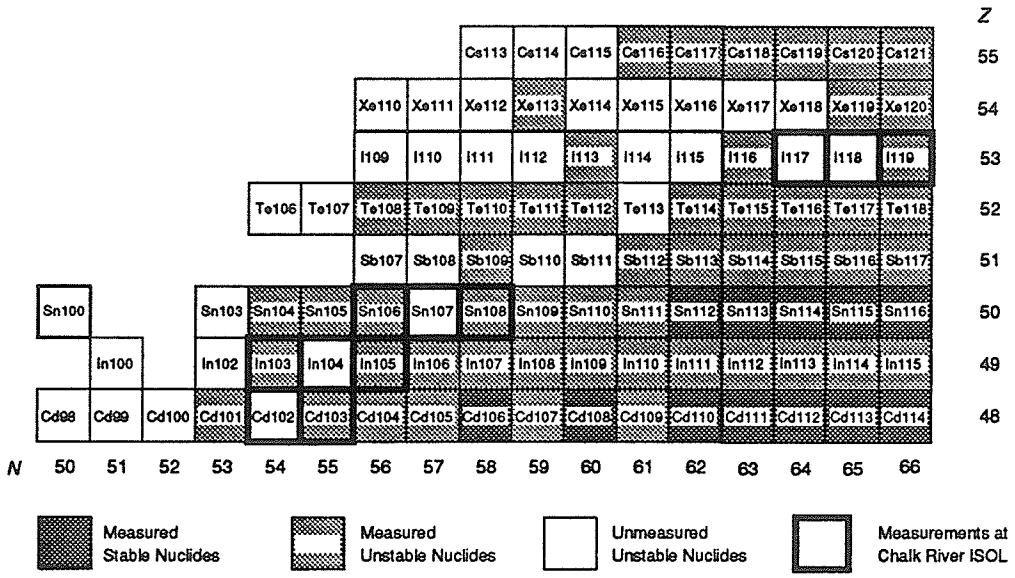

Figure 1.3. Chart of the nuclides in the vicinity of doubly magic ^{100}Sn. The nuclide masses measured with the Chalk River isotope separator are highlighted with a dark border.

2 Instrument and Technique

2.1 The Chalk River On-Line Isotope Separator (ISOL)

2.1.1 General Description

The Chalk River On-Line Isotope Separator (ISOL) is used on-line with the Tandem Accelerator Superconducting Cyclotron Facility (TASCC) to carry out atomic mass measurements on unstable nuclides as well as many other nuclear studies. The general layout of the TASCC facility is shown in fig. 2.1.

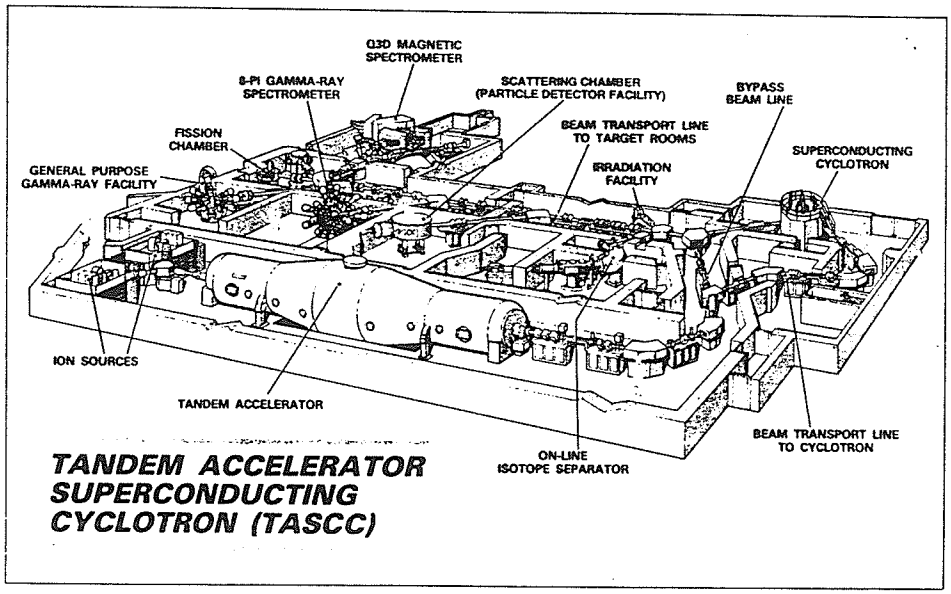

Fig. 2.1. TASCC Facility.

Negative ions ($^{27}Al^-$ for this work) were produced in the ion-source and accelerated in the 15 MV, Tandem van de Graaff accelerator. The energy of the ion beam may be boosted by further acceleration in the newly installed superconducting cyclotron. However, for this work, this was not necessary. The ion-beam, with a nominal energy of 5 MeV / nucleon, was transported to the target-ion source of the isotope separator.

The ISOL facility is shown schematically in fig. 2.2. Here, the beam strikes a target foil (^{natural}Mo, 2.2 mg/cm^2 for this work) located directly in front of the thin Ta entrance window of the ion-source (see fig. 2.3). A variety of reaction products, with lifetimes ranging from milliseconds to days, recoil into the ion source where they are ionized, extracted, and accelerated to a nominal energy of 40 keV. Because the ion energy is constant, the 135° analyzing magnet spatially resolves ions in the beam according to their mass, so that, at the image plane, individual mass components are resolved with a resolving power of 3,000 to 7,000. A narrow slit in the image plane allows ions of only one mass number to continue to detection. The ions of other mass numbers are stopped.

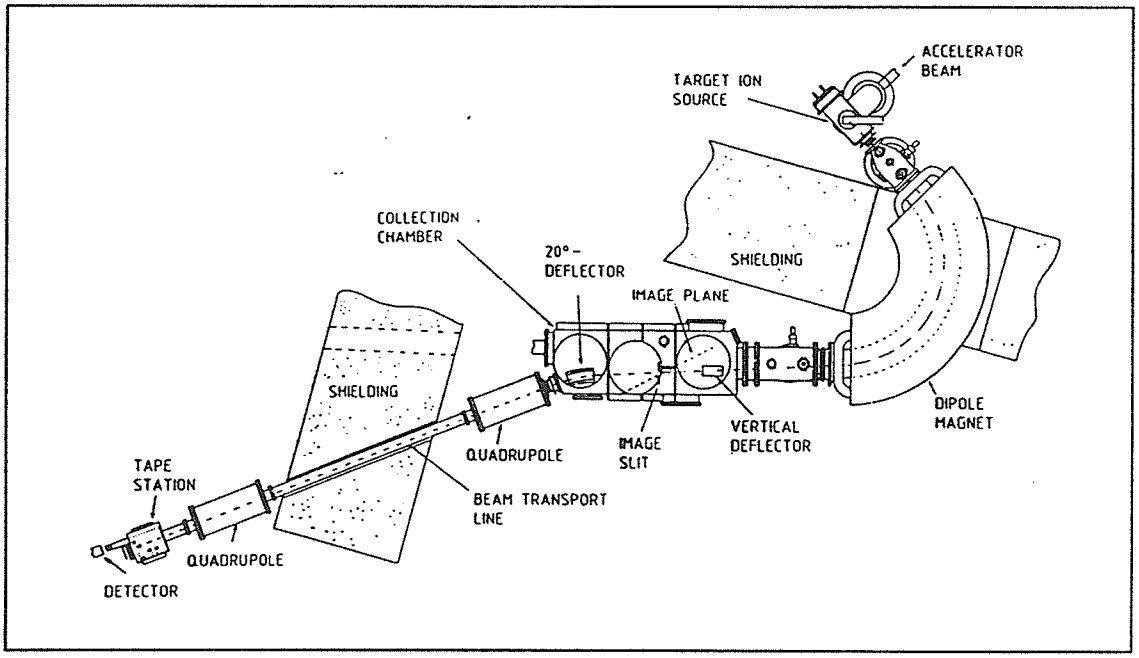

Fig. 2.2. Schematic view of the Chalk River on-line isotope separator.

The mass precision achieved, δM, is limited to a fraction, f, of the width, ΔM, of the detected mass peak signal. That is $\delta M = f \times \Delta M$. The expression for resolution may be used to write $\Delta M = R \times M$. By substitution then, the expression for precision becomes $\delta M = f \times R \times M$. Typical resolution of the separator is about 2×10^{-4} and f is about 1%,

given adequate counting statistics. Thus, the expected precision for the mass of ^{118}I is approximately 210 μu. This uncertainty may be reduced by a factor of $\sqrt{N}$ for N scans of the mass spectral peak. For example, 6 scans reduces the uncertainty to ≈ 100 keV.

The sections that follow highlight the important components of the instrument. A full discussion of the separator is given in references [Sc81], [Sh89].

2.1.2 Ion source and beam acceleration

There are three ion sources available for use with the Chalk River isotope separator. They are the plasma-type Bernas source [Ch67a,b], the helium-jet source [Ko91], and the Forced Electron Beam Induced Arc Discharge (FEBIAD) source [Ki76].

The Bernas source is a high-current (mA), off-line source. It is used primarily in applications using stable nuclides. The He-Jet ion-source is still in a developmental stage and has not yet been used for mass measurements. The FEBIAD ion-source is the source of choice for mass measurements. It has a highly stable output current (μA), which varies very little over the period of a single measurement. Moreover, the "hold-up" time (the time elapsed between the formation of the radioactivity and its subsequent extraction) is on the order of 30 s. This poses no problem since the activities of interest in this work had half lives greater than 190 s. The ion-source is shown schematically in fig. 2.3.

Ionization with the FEBIAD source may occur in two different modes; surface ionization and ionization in the plasma of an arc discharge. The surface ionization mode may be used for studies involving chemical species with low ionization potentials, such as the alkali metals and some alkali earths. Such an ionization method provides a chemical filter so that the extracted ion beams are free of contamination from other chemical families. The plasma ionization mode does not discriminate between chemical species.

In this case, a plasma is maintained in the ion source by means of an arc discharge between the cathode and the anode. A support gas of Xe is used to feed the plasma. Since iodine is not readily surface ionizable we used the plasma mode for this work.

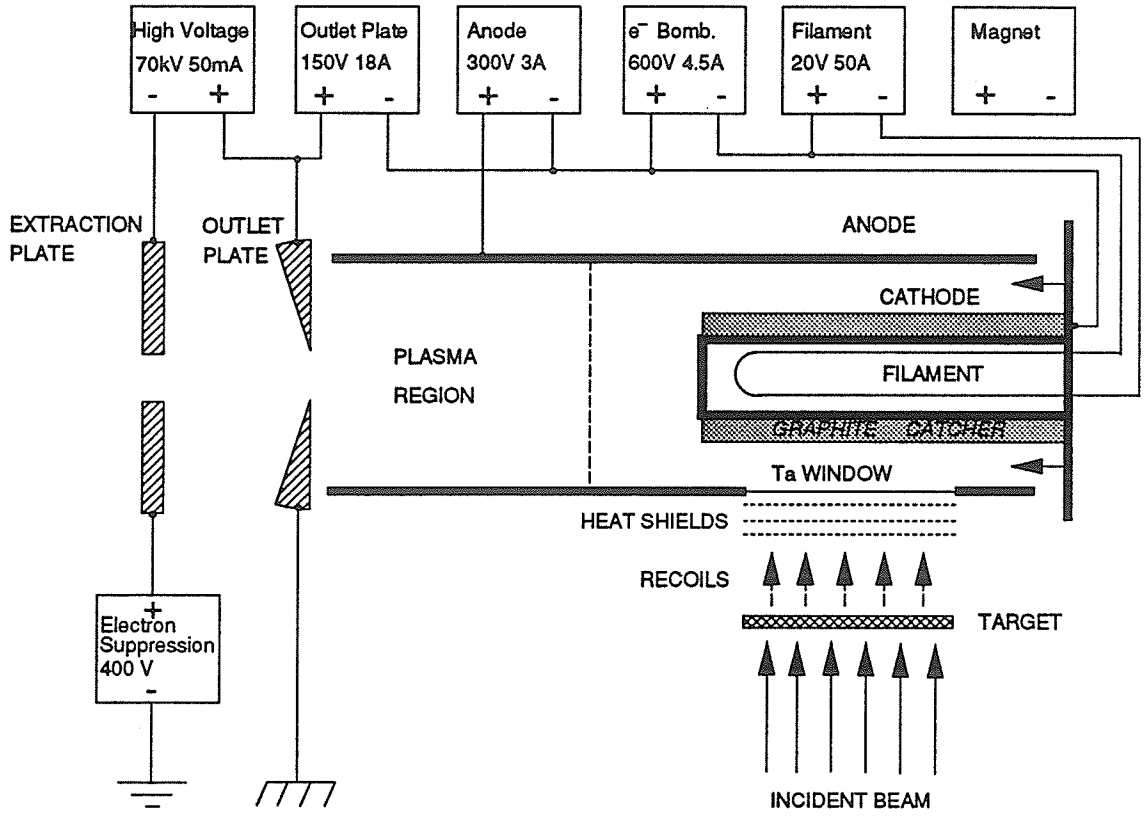

Fig. 2.3. FEBIAD target-ion-source used for the iodine mass measurement.

The FEBIAD source has an outer anode cylinder which is covered at one end with the outlet plate. The cathode cylinder is inserted into the other end. Reaction products (labeled "RECOILS" in the figure) are embedded into the heated catcher, eventually diffuse out and drift toward the plasma region of the source. (Details of the reactions used are given in § 3.1). The plasma, sustained with the support gas via a calibrated leak at a rate of 2×10^{-6} std cm^3/s, produces a Xe beam of 1.5 μA (all isotopes combined) at about 50% ionization efficiency. The source also requires an axial magnetic field to confine the

plasma radially. The magnet (not drawn in the figure) supplies a field of up to 80 mT.

Ions are extracted through a 0.50 mm diameter orifice in the outlet plate by means of a 40 kV accelerating potential applied between the outlet plate and the extraction electrode. The resolving power of the separator may be increased by reducing the diameter of the outlet plate orifice. This increase in resolution comes at the expense of reduced yields from the source. The accelerating potential is measured with a Julie HV-100 precision resistive divider chain and a Fluke 8502 digital voltmeter (DVM).

The electrostatic fields in the gap between the outlet plate and extraction electrode are determined by the applied accelerating potential and the geometry. The position of the extraction electrode is adjustable in position and orientation along the three orthogonal axes. It is positioned about 10-20 mm from the outlet plate. This adjustment in the extraction field, then, allows us to optimize the ion optics for the best focus and resolution at the image plane.

At first glance it would appear the outlet plate orifice of the ion source would define the *geometric object* of the ion optical system. However, a *virtual object* is formed inside the source, behind the outlet plate opening (see fig. 2.4). The plasma boundary acquires a meniscus shape behind the opening due to the local electrostatic fields. Since the plasma is a good electrical conductor, the electrostatic field lines at the plasma boundary are at right angles to its surface. Ions drawn out of the plasma have small kinetic energies, initially, and their paths follow the perpendicular field lines near the boundary. The field lines and the path of the ions quickly straighten out past the outlet plate opening due to the large potential gradient from the extraction plate nearby. The size of the virtual object becomes apparent as we attempt to retrace, from right to left as in fig. 2.4, the origin of the ions from inside the source. The dashed lines retrace a much smaller point of

origin inside the plasma. To an observer outside the ion source this virtual origin appears as the object slit. Thus the virtual object rather than the geometric object determines the resolving power of the separator.

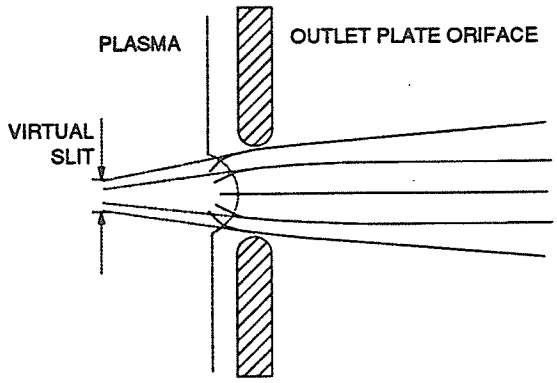

Fig. 2.4. A virtual object of the ion optical system is formed due to the shape of electrostatic field lines at the plasma boundary. The virtual object is defined by tracing the dashed lines back inside the source. The virtual object width rather than the geometrical object width determines the resolving power of the separator.

The energy of the extracted beam from the ion-source for different chemical species at a fixed accelerating potential has been carefully measured. Investigations of these differences, at the one part-per-million level, have concluded that different elements do not emerge from the ion source with significantly different energies [Ha91]. Such differences in energy could result in a systematic bias in the measured mass ratios between peaks corresponding to different elements. However, as a precaution, we have restricted our mass measurements to isotopes of the same element.

2.1.3 Main magnet

After acceleration, the ion beam traverses a 1 m long drift space before entering the main magnet. This dipole has a sector angle of 135° and mean radius of 1.00 m. The field is inhomogeneous with the form $B = B_0 \left(\frac{r_0}{r}\right)^n$ where n is nominally 0.5 and B_0, r_0 refer to the optic axis. As a result of this, the magnet has the property of focussing the

ion beam in both the radial and axial directions (refer to fig. 2.5)[Ca70]. That is, a point object is imaged as a point image. Corrective coils are available to vary both the quadrupole and sextuple components of the field [Ca81]. These coils are used to adjust the position of the focus along the beam axis and also to correct the aberrations of the ion-optical system.

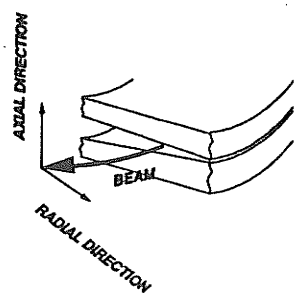

Fig. 2.5. Beam axes definition.

The image plane of the separator is located 1.64 m from the exit boundary of the main magnet. The radial dispersion of the separator, D, is 2250 mm. The dispersion is related to the separation, d, between ion beams of differing mass at their foci. The radial separation of images corresponding to the masses M and $M + \Delta M$, at a focus, is $d = D\left(\frac{\Delta M}{M}\right)$. Thus at mass 118, neighboring mass beams are separated by 19 mm. The vertical magnification is unity. The magnet entrance pole face is shaped concave with a radius of 35.0 cm. The exit pole face is flat. As a result the focal plane is tilted by 25° with respect to the mean beam axis.

A beam monitor consisting of a 32 wire "comb" may be lowered into the beam path at the entrance to the magnet. The current on the wires is scanned to form a one-dimensional signal which is displayed on an oscilloscope. This assists in obtaining the optimum beam injection profile into the magnet.

2.1.4 Collection chamber

The beam is brought to a focus on an image slit (0.25 mm wide, 10 mm high) located in the collection chamber. The dimensions of the beam at the position of the image slit are largely independent of mass. The width of the ion beam b is related to the resolving power R_P and dispersion D by the relationship, $b = D/R_P$. Thus for a resolving power $\frac{M}{\Delta M}$ of 9000, the beam width would be 0.25 mm. (Note: ΔM in this case is defined as the FWHM of the beam. This is not necessarily equal to the FWHM of the observed beam spectral lineshape. Details follow.)

When the beam width and image slit widths are comparable, the optimum resolution and detected beam intensity are obtained simultaneously (refer fig. 2.6). This special case underscores the competing requirements of counting statistics and resolution of a beam detection system. Greater number of detected counts are necessary for reduced statistical errors. Higher resolution allows one to more to more precisely locate the position of a peak. These two considerations dictate that the slit width should be as wide as the beam. In fact, the image slit used in this work was the same width as the FWHM width of the beam.

In addition to the image slit, the collection chamber contains a Faraday Cup and a 10 μm tungsten wire for the purposes of tuning the ion beam profile. They are mounted on a moving carriage whose position may be adjusted along the focal plane. The wire is used to optimize the width of the beam, and thus, the resolution. The mass spectral lineshape detected with the wire is analogous with fig. 2.6.(c) where $w'' = 0$. The Faraday Cup may be fitted with entrance slits of various widths. We fit the Faraday Cup with an entrance slit greater than the beam width in order to read the ion beam current.

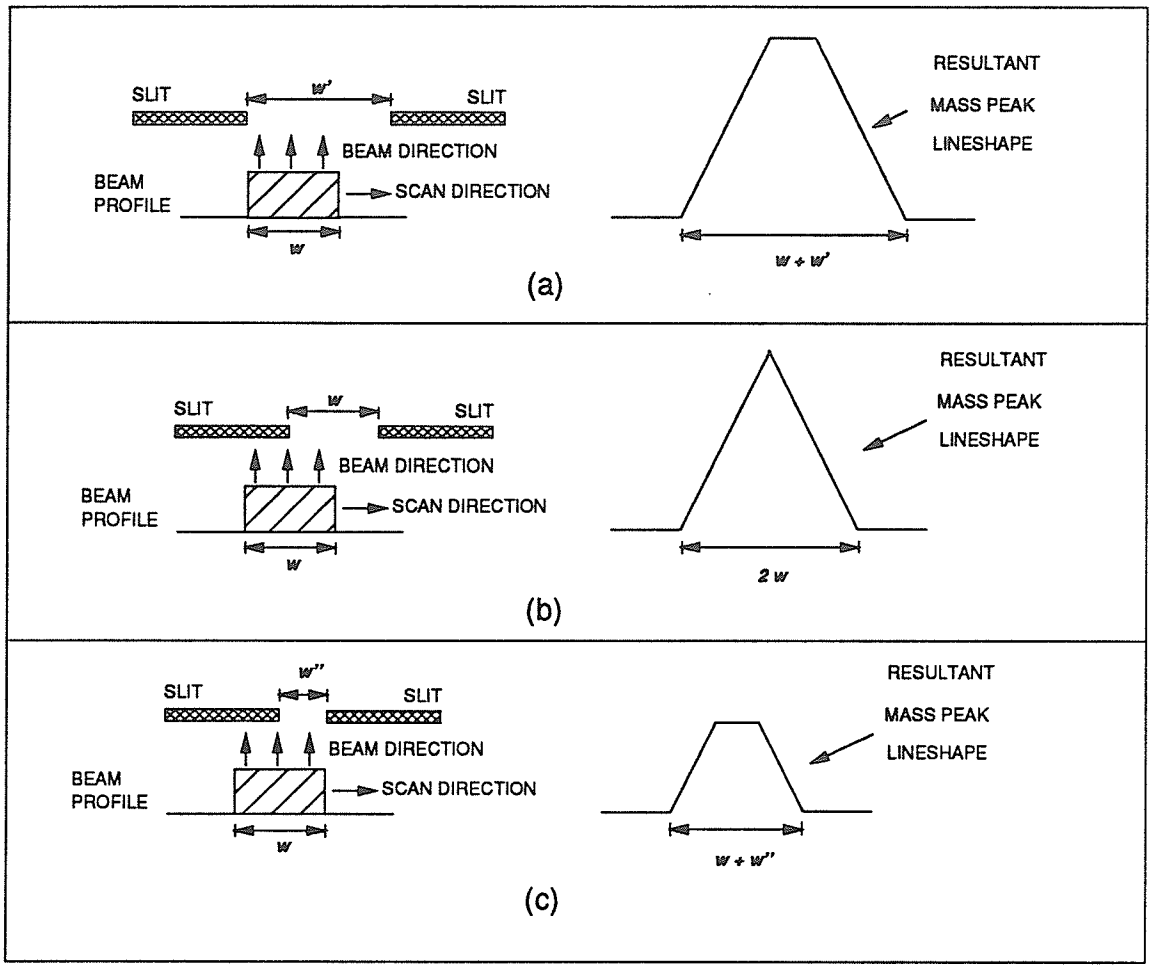

Fig. 2.6. A simple beam profile, of width w, is projected through three different slit widths in frames (a) - (c). The corresponding lineshapes observed by the detection system (not shown) are given beside. In frame (a) the slit of width $w' > w$ yields a line shape of width $w + w'$ and maximum intensity. In frame (b) the slit width is equal to the beam width and yields a line shape of width $2w$ and maximum intensity. In frame (c) the slit width is smaller than the beam width $w'' < w$. The resulting line shape is narrower (i.e. better resolution) but at the expense of intensity.

2.1.5 Beam Transport Line (BTL)

Ions passing through the image slit are directed to a low background counting area by means of the electrostatic beam transport line (BTL). The BTL consists of a 20° deflector and two electrostatic quadrupole doublets. Ions from the beam that have

become electrically neutral during their passage through the separator are removed by the deflector. (Ions neutralized during their passage through the analyzing magnet may contaminate neighboring mass components.) Transmission through the BTL is greater than 98%. For technical reasons, the maximum beam current through the BTL is restricted to less than 1 mA. The BTL is able to focus the transmitted beam into a circular spot not more than 2 mm in size at a distance of 50-70 cm past the last quadrupole.

2.1.6 Counting chamber and tape station

Past the last quadrupole of the BTL, the ion beam is brought to a focus on the aluminized mylar tape of the tape transport system. After a preset time, radioactivities implanted into the tape are moved close to the vicinity of a pair of Hyper-pure germanium (HPGe) detectors located some 75 cm away. The tape moves at a speed of 585 cm / s from the implantation position which is under vacuum, to the detectors at atmospheric pressure, through three stages of differential pumping.

The counting chamber is also equipped with a Faraday cup, with electron suppression, to check the transmission of the BTL.

2.1.7 Summary

Some of the basic properties of the isotope separator are presented in table 2.1. The resolution of the separator is primarily limited by the size of the ion source orifice and the image slit. Smaller slit widths yield higher resolution, but at the disadvantage of reduced efficiency. In the past, the best resolving power achieved off-line is 20,000 for an N_2-CO_2 doublet [Sh89]. The main contributions to the beam width were optical aberrations, energy spreads, and the stability of the accelerating potential power supply.

Table 2.1. Basic properties of the isotope separator.

Property	Definition	Value
Magnet angle		135°
Mean magnet radius		1000 mm
Approximate field index n		0.5
Magnetic field	$(Br_0)_{max}$	62.5 T-cm
Magnet power supply		350A/50V
Dispersion	D	2250 mm
Resolving power, FEBIAD routine	R FWHM	9000 , 0.50 mm orifice
Radial magnification		1.25
Angular magnification		0.77
Vertical magnification		1
Mass range	$\frac{(M_{max}-M_{min})}{M_{min}}$	15%
Extraction voltage, maximum		70 kV
Extraction voltage, typical		40 kV
Stability of magnet current, peak to peak(p-p)		5×10^{-6}
Stability of extraction voltage, long term, (p-p)		5×10^{-6}
Maximum beam current		20 mA
Maximum beam current with FEBIAD source		1.5 μA
Enhancement factor ε		$> 10^6$

2.2 Experimental Procedure

The well known mass spectrometric technique of peak matching is used to measure the spacing between mass peaks [Me72]. This technique is based on a theorem, given by Swann [Sw31] and first applied to mass spectroscopy by Bleakney [Bl36], which states that two masses M_1 and M_2 will follow identical paths through a mass spectrometer if all magnetic fields are held constant and all electrostatic potentials, V_i, applied to the instrument are scaled such that

$$M_1 V_1 = M_2 V_2 \quad . \tag{2.3}$$

The image slit is fixed in place along the image plane and we vary the ion source accelerating potential (and other potentials accordingly) to sweep selected ion beams past the image slit. In this way we form (via off-line analysis) mass peaks which correspond to applied potentials. The theorem as stated above for a doublet peak is extended trivially for a mass triplet of M_1, M_2, and M_3. If we allow M_1 to be the known reference mass, and experimentally determine the voltages corresponding to the centroids of the mass peaks, V_1, V_2, and V_3, then the unknown masses M_2, M_3 may be found by

$$M_2 = M_1\left(\frac{V_1}{V_2}\right) \qquad \text{and} \qquad M_3 = M_1\left(\frac{V_1}{V_3}\right) \quad . \tag{2.4}$$

The experimental procedure also allows for the presence of isobaric contaminants. The production of the iodine isotopes of interest by a fusion-evaporation reaction will also produce xenon, tellurium and other species (see §3.1). The minimum resolving power, $\frac{M}{\Delta M}$ required to just resolve iodine from its isobaric neighbors Te and Xe is as high as 35,000 for the ^{118}Xe-^{118}I case. Obviously these isobaric contaminant components will not be resolved since the separator has a nominal resolving power of 9000 (FWHM).

This problem is solved by the ion detection method employed. We identify the arrival of the desired nuclei by their unique radioactive decay signature instead of a signal from an indiscriminate ion counter. Consequently, we avoid the ambiguities resulting from isobaric and isomeric admixtures. Ion counting by a unique decay signature allows us to precisely determine the mass of a nuclear species without actually spatially resolving it from isobaric neighbors in the separator beam.

It is interesting to note we are using the isotope separator as a mass spectrometer instead of its traditional design mode as a mass spectrograph. A spectrograph holds all fields fixed while beam components are resolved by their relative position on the image plane. A mass spectrometer, on the other hand, is characterized by fixed image and object slits where the electrostatic / magnetic fields are ramped to sweep the beam.

2.2.1 On-line scanning procedure

The separator beam is scanned, under computer control, across the image slit. A block diagram of the control and data acquisition circuitry is provided in fig. 2.7.

The accelerating potential, nominally 40 kV, is controlled by varying the reference potential (~400V) provided to the supply. This reference potential consists of a fixed, stable potential reference summed with a potential supplied by a CAMAC controlled digital to analog converter (DAC). In this way, the accelerating potential may be preset to a value and scanned point by point over a range of 2.5% of its mass. Typically, an experiment is set up such that a mass peak (FWHM) is sampled in 8 scan points, or channels, of a total 25 channel mass spectrum. At a nominal operating potential of 40 kV and a resolution of 2×10^{-4}, the potential steps are approximately 1 V. The applied high potential is measured by two resistive divider chains. A 100:1 divider provides and error signal for the HV supply and a 10 000:1 divider provides a potential level for the DVM.

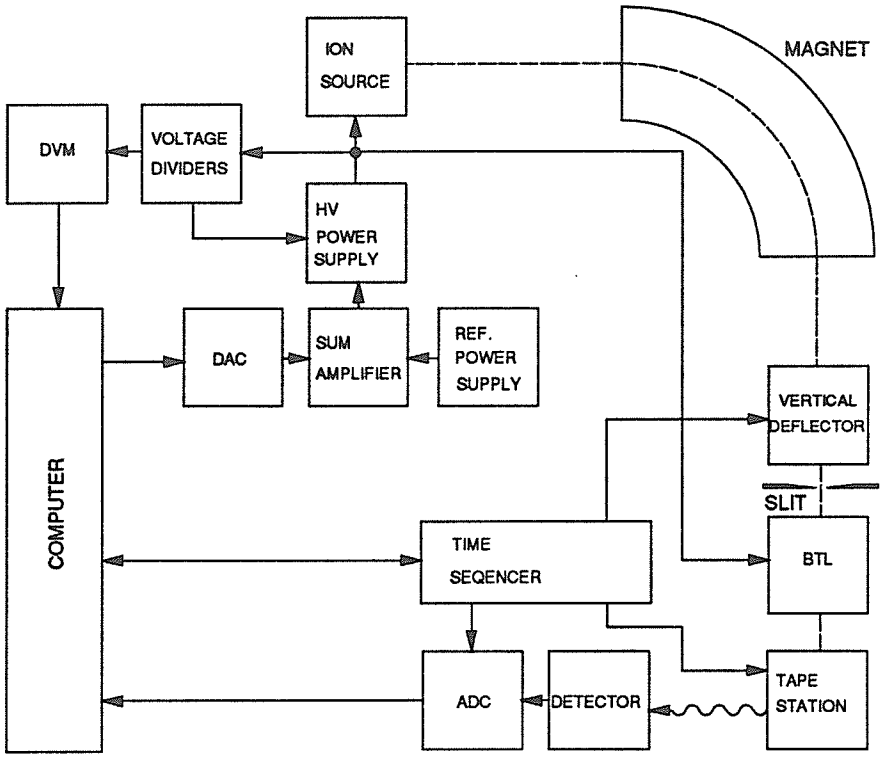

Fig. 2.7. Block diagram of the separator showing the operational relationship between components for a mass measurement using the peak matching technique. The labels are: DVM - digital voltmeter, DAC - digital to analog converter, BTL - beam transport line, ADC - analog to digital converter. The dashed line represents the separator beam.

There are no electrostatic elements between the accelerating gap of the ion source and the image slit. The potentials of the ion optical elements in the BTL are scaled in proportion to the accelerating potential.

At each scan point, the beam is transmitted through the image slit and the BTL and deposited onto the aluminized mylar tape of the tape station. In consideration of instrumental drifts, the time period for each point is usually 1.3 times the lifetime of the species under study or 137 seconds, whichever is smaller. (A time of 137 seconds per scan point, leads to a complete scan over 3x25 points of approximately 3 hours. Detailed studies of the stability of major components have been performed in the past [Sh89] to insure that

instrumental drifts in voltage/current of the many components does not degrade our results. Three hours is a conservative time limit in view of these drifts.) The shortest lifetime of the iodine activities under study is 190 seconds, so we chose the 137s cycle time.

At the end of each scan point the ISOL beam is deflected and the sample on tape is quickly moved in front of the HPGe detectors. The beam deflector consists simply of two electrostatic plates placed above and below the beam in the collector tank. While the tape move is executed the next increment in accelerating potential is applied and a short time is allowed for the potential to settle. The beam deflect is then turned off, and a new beam sample collected. At the end of each scan point, the accelerating potential, observed γ-ray spectra, actual cycle times encountered and various beam setting are saved to magnetic tape for further off-line analysis. The γ-ray spectra are also sorted for on-line inspection of the data. The timing sequence for a scan point is presented in fig. 2.8.

As an added precaution to errors caused by drifts, the order of mass points scanned is not sequential across the mass spectra but interleaved to sample the mass spectra quasi-simultaneously. The first points to be scanned are near the maxima at each mass spectral peak. Following points alternate on either side of the maximum positions until the entire mass spectrum is complete. Fig. 2.9 represents the chronological order of a scanned mass triplet.

Studies of the robustness of these procedures have been done for one hypothetical drift scenario, a systematic decrease in the production rate of the ion species considered. This could be caused by degrading ion source conditions, or possibly a decrease in the heavy ion beam supplied by the tandem accelerator. Fig. 2.10 shows this scenario for a very large decrease of 50% from its starting value. For masses scanned sequentially there

is a corresponding shift in the centroid position of 4 ppm. The interleaved scan is shifted by a factor of 10 less. The net effect of drifts and instabilities contribute an error much less than the accuracy to which we are able to locate the centroid in a single scan.

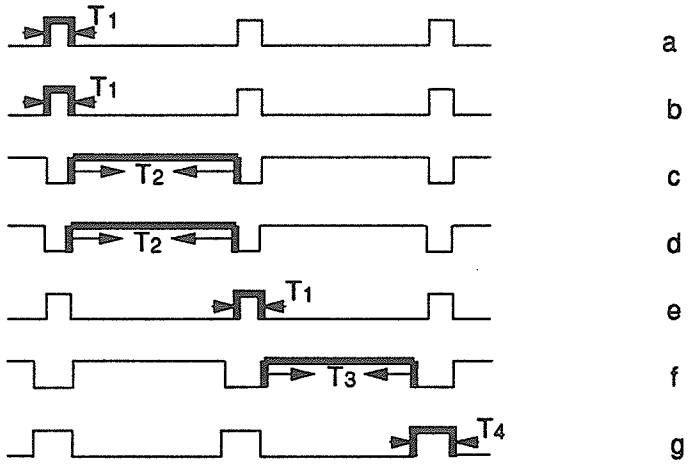

Fig. 2.8. Representation of the time sequence for the stepwise scanning of a mass peak: (a) deflect separator beam ; (b) establish accelerating and BTL voltages; (c) collect sample on tape; (d) measure accelerating voltage; (e) move sample on tape to HPGe detectors; (f) record γ-ray spectrum, and (g) transfer data to magnetic tape. Typical values in this experiment are: $T_1 = 2$ s, $T_4 = 7$ s, and T_2 is 137 s. T_3 is always $T_2 + T_1 - T_4$.

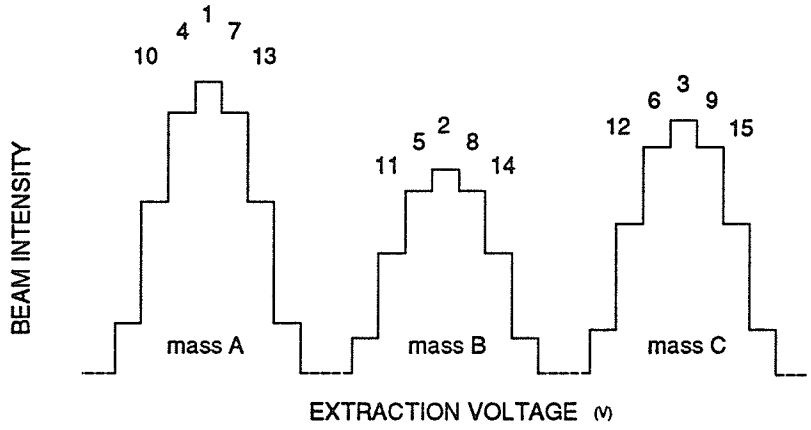

Fig. 2.9. Chronological order of data collection in a mass scan that covers three ion beams, with masses *A,B,C*. The numbers above the peaks indicate the order in which data points are taken. The first voltage point selected corresponds to the maximum transmission of the ion beam corresponding to mass *A*, the second to mass *B*, and the third to the maximum for ion beam *C*.

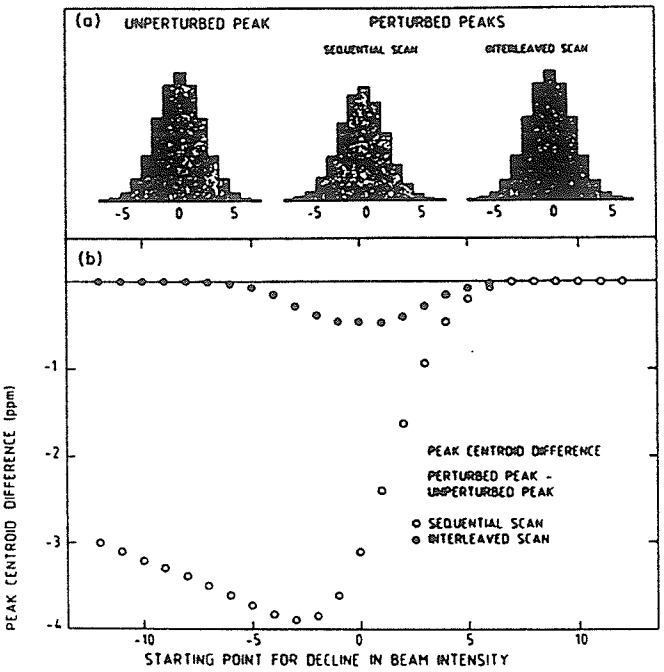

Fig. 2.10. Centroid shift for a beam loss scenario. Simulation of the errors in peak centroid determination resulting from a linear decline with time in the separated radioactive-beam intensity. Typical separator separating conditions have been assumed. The mass peak is centered at an extraction potential of 40 000 V, the resolving power is 6 000, and the mass scan is 25 points (30 V) wide. (a) shows our reference peak, as well as two perturbed peaks resulting from a beam-intensity decline commencing in point - 2 and continuing to the end of the scan where the intensity has dropped to 50% of its initial value. The effect of this intensity change is clearly visible in the mass peak obtained with a sequential scan but is hardly noticeable for that obtained with an interleaved scan. (b) shows the shift in the centroid, defined as the difference in the centroids of the reference and perturbed peaks divided by the reference peak's centroid value. The shift is shown as a function of the point number where the intensity decline begins.

2.2.2 Off-line data analysis

The task of the off-line analysis is to read the magnetic tape record of on-line data and determine the potentials applied to the ion source that correspond to centroids in the respective transmitted iodine isotopes. The voltage ratio of the iodine isotopes so obtained is directly related to their mass ratio through Bleakney's Theorem. We discuss

here the method used to obtain voltage ratios for a single scan of the mass triplet. Chapter three discusses, in detail, how voltage ratios from each scan are combined to give a final result.

The logical structure of the off-line analysis is reduced to three steps. The first is to select the radioactive decay signatures that uniquely identify the iodine isotopes of interest. The second is to generate mass spectra based on these selected decay signatures. The third is to calculate the centroids for each iodine isotope of each mass spectrum.

The three steps of the off-line analysis are carried out by three computer programs; MASSGATE, MASSANAL, AND MASSDIF.

2.2.2.1 Selecting γ-ray energies; MASSGATE

The first step is to detect the presence of specific iodine isotopes in the collected γ-ray spectra. Energy "windows" are set at the energies of the ß-delayed γ-rays emitted during the decay of the iodine isotopes. Up to 30 γ-ray energies may be chosen to identify the activity of the nuclides of a mass triplet.

2.2.2.2 Building voltage, mass and γ-ray spectra; MASSANAL

The second step is to generate voltage and mass spectra, based on the magnetic tape record of the on-line data. The resulting spectra are saved to hard disk in the Holifield Heavy Ion Research Facility .SPK file format. Additionally, the on-line γ-ray spectra are sorted and stored in .SPK file format.

The on-line data is, most simply, a set of separator accelerating potential, for each potential, and a matching γ-ray spectrum. The first spectrum generated is the separator accelerating potential spectrum. The ion accelerating potential is recorded against scan point number. (Note: the scan point number is not chronological in an interleaved mass scan.) An additional spectrum of the point by point accelerating potential differences

serves as a useful diagnostic tool. Ideally this spectrum is flat except at mass number changes. If there are sharp excursions they flag bad data, which may be then excluded from further processing.

An individual mass spectrum is generated for each decay γ-ray specified by MASSGATE. Scaled ion intensity, I_{point}, is recorded against the scan point number where the scaled ion intensity is given by

$$I_{point} = N\, Q_{corr}\, F + 0.5 \tag{2.5}$$

In this equation, N is the number of atoms collected during a time $T_{COLLECT}$ and the charge correction term, Q_{corr}, is intended to compensate for changes in the primary beam current delivered to ISOL over the duration period of a scan. Q_{corr} is normalized to the beam current at the first scan point. The scale factor term, F (typically 10), is included to reduce computing errors introduced by integer math.

The number of iodine ions collected, N, is the product of the rate of arrival (ions/s) for ions of a particular species, P, and the collection time $T_{COLLECT}$. The rate of arrival, P, is assumed to be constant over the collection interval.

However, some of the atoms collected during $T_{COLLECT}$ will decay while the sample was being accumulated. The number of atoms collected on tape after time $T_{COLLECT}$ is given by

$$N_{COLLECT} = \frac{P}{\lambda}\left(1 - e^{-\lambda T_{COLLECT}}\right) \tag{2.6}$$

where λ is the decay constant for the species. During the transport to the detectors, in a time T_{WAIT}, some more will decay. The number that reach the detectors would be

$$N_{transferred} = N_{COLLECT}\, e^{-\lambda T_{WAIT}} \tag{2.7}$$

Of these, N_{COUNT} of the collected atoms would decay in front of the detectors.

$$
\begin{aligned}
N_{\mathrm{COUNT}} &= N_{\mathrm{transferred}}\left(1-e^{-\lambda T_{\mathrm{COUNT}}}\right) \\
&= \frac{P}{\lambda}\left(1-e^{-\lambda T_{\mathrm{COLLECT}}}\right)e^{-\lambda T_{\mathrm{WAIT}}}\left(1-e^{-\lambda T_{\mathrm{COUNT}}}\right)
\end{aligned}
\tag{2.8}
$$

The number of γ-rays detected is

$$
\begin{aligned}
N_{\gamma} &= \varepsilon B\, N_{\mathrm{COUNT}} \\
&= \frac{\varepsilon B\, P}{\lambda}\left(1-e^{-\lambda T_{\mathrm{COLLECT}}}\right)e^{-\lambda T_{\mathrm{WAIT}}}\left(1-e^{-\lambda T_{\mathrm{COUNT}}}\right)
\end{aligned}
\tag{2.9}
$$

where ε is the detector efficiency and B is the absolute branching ratio for the γ-ray transition. Therefore

$$
P = \frac{\lambda N_{\gamma}}{\varepsilon B\,(1-e^{-\lambda T_{\mathrm{COLLECT}}})\,e^{-\lambda T_{\mathrm{WAIT}}}\,(1-e^{-\lambda T_{\mathrm{COUNT}}})}
\tag{2.10}
$$

is the number of ions of the species of interest arriving at the tape station per second. Finally, N, which is needed in equation (2.5), the number of atoms of interest collected during a time $T_{COLLECT}$ is

$$
\begin{aligned}
N &= P\, T_{COLLECT} \\
&= \frac{\lambda N_{\gamma} T_{COLLECT}}{\varepsilon B\,(1-e^{-\lambda T_{\mathrm{COLLECT}}})\,e^{-\lambda T_{\mathrm{WAIT}}}\,(1-e^{-\lambda T_{\mathrm{COUNT}}})}
\end{aligned}
\tag{2.11}
$$

An example of building an individual mass spectrum, accompanied with its voltage spectrum, is given in fig. 2.11.

One "sum mass spectrum" is formed from the individual mass spectra where each mass peak in the sum spectrum is the result of a selective summing of individual spectra. Thus the first 25 points of the sum mass spectrum (the part of the scan that pertains to mass 1), contain all the individual mass spectra for mass 1. Data from other individual mass spectra are rejected. The same procedure is applied for points 26-50 and 51-75 respectively.

Lastly, for diagnostic purposes, the γ-ray data for an entire scan is sorted into four special γ-ray spectra. There are three isobar-specific (or mass-specific) sum spectra formed by adding the corresponding raw γ-ray spectra. The fourth is a cumulative sum of all raw γ-ray spectra over the entire scan.

Fig. 2.11. (Over)

Mass spectral peaks obtained during a single mass scan of the iodine triplet measurement. Part (a) shows the discrete ion accelerating potentials applied at the source. For clarity, the scan point numbers are shown in order of increasing voltage and not in the order of their accumulation. Part (b) represents a sample of the isobaric γ-ray spectra collected at each voltage step. A total of 75 raw γ-ray spectra are accumulated for a triplet scan (according to 75 voltage steps). Iodine specific transitions (darkened) are gated in order to build the mass spectrum of part (c). Part (c) shows the beam intensity for ^{119}I,^{118}I, and ^{117}I as a function of scan point number. The mass and voltage spectra are later correlated (see the next section) to determine each isotope's peak position.

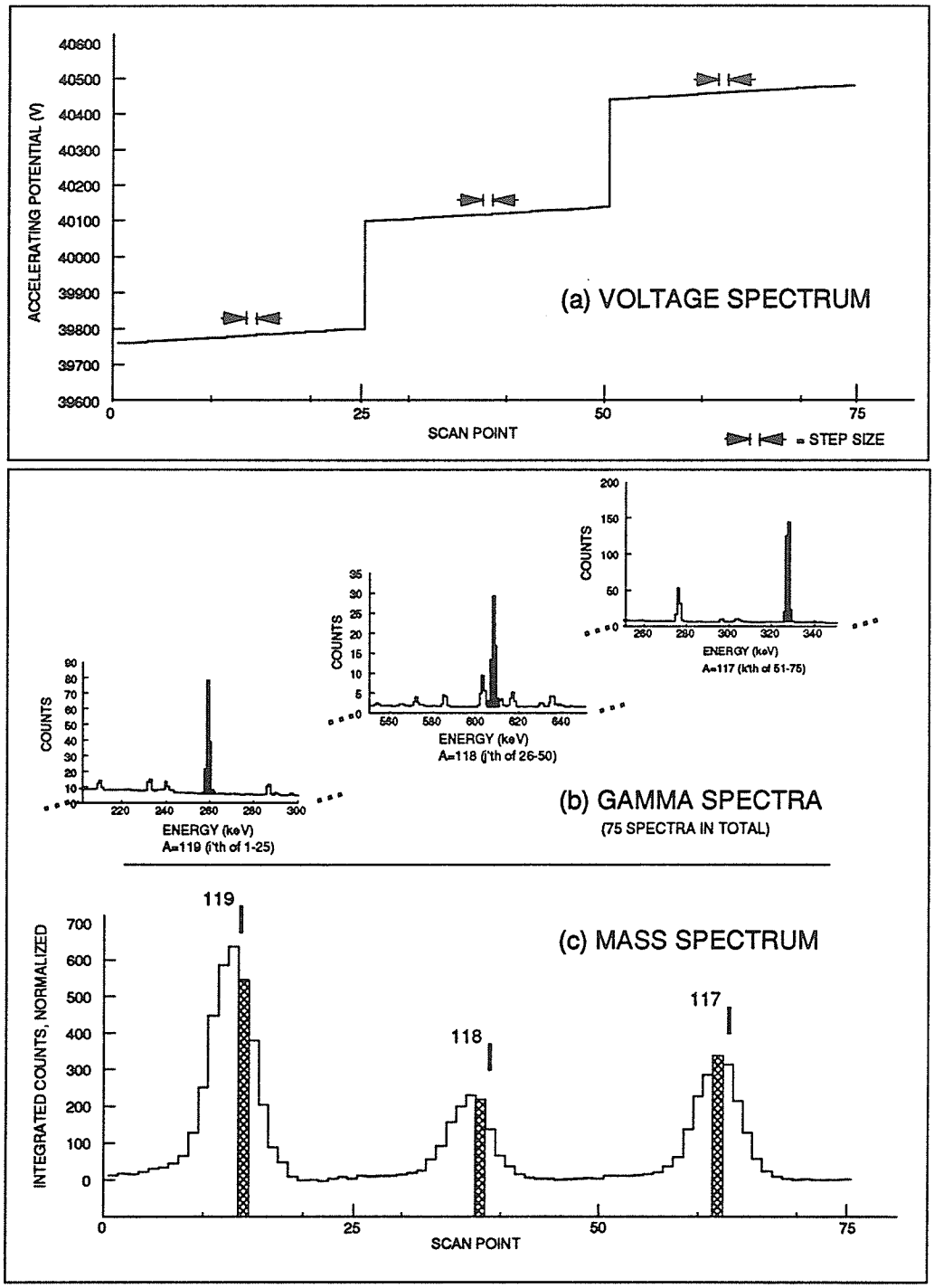
ACCELERATING POTENTIAL (V)
40600
40500
40400
40300
40200
40100
40000
39900
39800
39700
39600
0
25
50
75
SCAN POINT
(a) VOLTAGE SPECTRUM
= STEP SIZE
COUNTS
ENERGY (keV)
A=119 (i'th of 1-25)
ENERGY (keV)
A=118 (j'th of 26-50)
ENERGY (keV)
A=117 (k'th of 51-75)
(b) GAMMA SPECTRA
(75 SPECTRA IN TOTAL)
INTEGRATED COUNTS, NORMALIZED
119
118
117
(c) MASS SPECTRUM
SCAN POINT

2.2.2.3 Determining peak positions; MASSDIF

The MASSDIF program reads the sum mass spectra from the off-line .SPK file produced by MASSANAL, locates the peaks and calculates the centroids, centroid uncertainties, and FWHM. Typically, we must determine the centroid to less than $\frac{1}{10}$ of a channel width. (Recall from §2.1.1 that we locate the peak position to about 1% of its FWHM. The mass peak usually extends over ~8 channels at FWHM). Our algorithm then, requires considerable attention to be given to estimating fractional channel contents.

The analysis begins by locating the peak channel in the sum mass spectrum. The average peak height and average background level, from which a cut-off level at 20% peak height, are then deduced. Fractional channel contents at the cut-off level are estimated by interpolating a straight line between adjacent data points as shown in fig. 2.12.

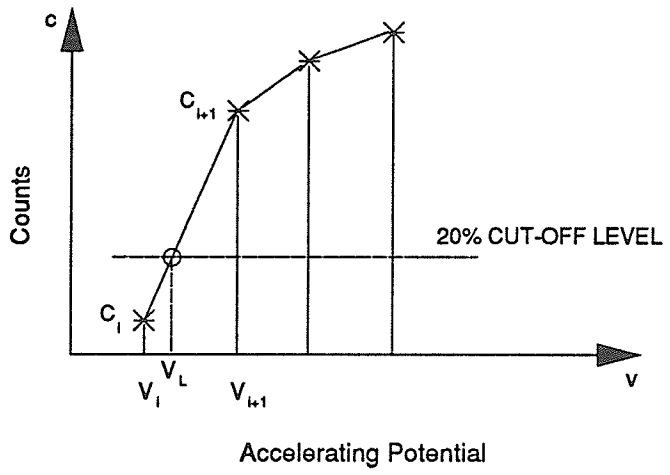

Fig. 2.12. The experimental data consist of the discrete data set $\{V_i, C_i\}$, where the subscript i represents the scan point. The labeling convention for the left fractional channel V_L, at the 20% cut-off level, is shown. The same formalism exists for the right fractional channel V_R.

A centroid evaluation for the portion of the peak lying between the cut-off voltages, V_L and V_R, may be written in the form

$$\text{centroid} \quad = \quad \frac{\int_{V_L}^{V_R} v\, c(v)\, dv}{\int_{V_L}^{V_R} c(v)\, dv} \quad , \tag{2.12}$$

where $c(v)$ is the function describing the mass peak. However, the analytical form of $c(v)$ is unknown, so we continue to use the straight line approximation between data points to construct a series of trapezoids as shown in fig. 2.14.

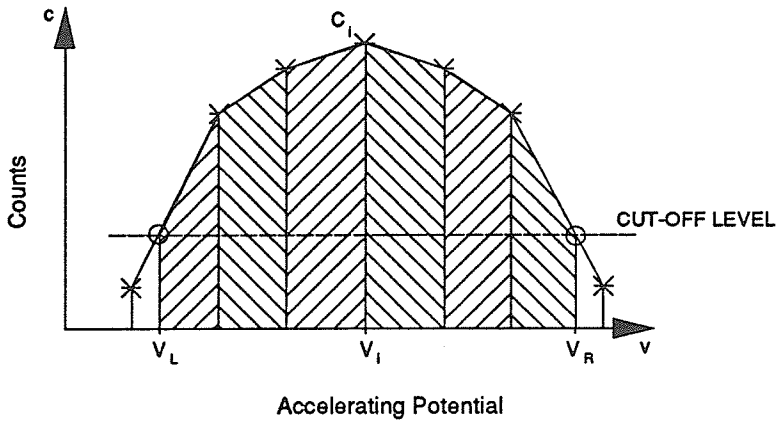

Fig. 2.13. Peak centroid determination. The centroid of each trapezoid is summed to determine the centroid of the entire peak within the cut-off boundaries.

The centroid of a single trapezoid segment, c_i', is given by

$$c_i' \quad = \quad \frac{2\,C_{i+1}\,V_{i+1} + 2\,C_i\,V_i + C_i\,V_{i+1} + C_{i+1}\,V_i}{3\,[\,C_{i+1} + C_i\,]} \tag{2.13}$$

The centroid of the entire peak is found by using the discrete form of the centroid formula given in equation (2.12). That is

$$\text{centroid of the entire peak} = \frac{\sum A_i \circ c_i'}{\sum A_i}$$

$$= \frac{\frac{1}{6}\sum_{i}^{N-1}[2C_{i+1}V_{i+1}+2C_iV_i+C_iV_{i+1}+C_{i+1}V_i][V_{i+1}-V_i]}{\frac{1}{2}\sum_{i}^{N-1}[C_{i+1}+C_i][V_{i+1}-V_i]} \tag{2.14}$$

where A_i is the area of a single trapezoid segment.

The uncertainty in the centroid is expressed in two ways; the statistical uncertainty and voltage uncertainty. The statistical uncertainty is obtained by taking the partial derivative of the centroid with respect to the counts C_i. The voltage uncertainty is similarly obtained by taking the partial derivative of the centroid with respect to voltage V_i.

The statistical uncertainty is related to the counting statistics familiar in any γ-ray counting experiment. The source of voltage uncertainty is the precision achievable by the DVM. Also, in a minor way, the voltage uncertainty is related to the evaluation of fractional channels at the edges of the mass spectral peak. In this evaluation we must recognize the mass peak signal above the level of the background. As mentioned, the mass peak cutoff at 20% above background leads to fractional channels at the peak edges (refer fig. 2.13). Depending on the slope of the spectral "lineshape" at this cutoff, the fractional channels are determined with large or small uncertainties. As expected, the higher the signal-to-noise ratio (i.e. a steeper slope), the more precisely the edges of the peak are located.

3 The Iodine Experiment

3.1 Production of activities

The iodine activities are produced by bombarding a fixed target foil with a heavy ion beam ($E \sim 5$ MeV/u) delivered from the TASCC facility. During collisions, target and beam nuclei fuse together forming a highly excited compound nucleus. This compound nucleus quickly decays, in about 10^{-21}s, by the isotropic emission of γ-rays and nucleons. The process is illustrated in fig. 3.1. The residue remaining after this "evaporation" is fairly energetic and retains nearly the same momentum as the incident beam. The residue recoils through the target material ($\sim 10^{-14}$s for a 2 mg-cm^{-2} target), passes through three 20 μg-cm^{-2} thick carbon heat shields, and the 2 mg-cm^{-2} tantalum entrance window of the target-ion source before coming to a stop in the graphite catcher (refer fig. 2.3). It subsequently diffuses out of the catcher and drifts toward to the ionization region of the target-ion source (refer § 2.1.2).

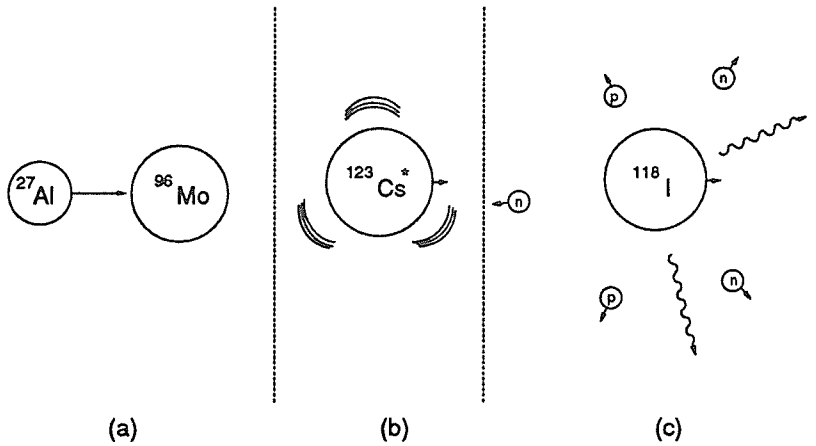

Fig. 3.1. *Fusion-Evaporation Reaction.* (a) A 130 MeV aluminum ion from the accelerator strikes a stationary molybdenum target nucleus. (b) The nuclei fuse to form a highly excited state which recoils through the target. (c) The excited state quickly decays ($\sim 10^{-21}$s) by emitting protons, neutrons, and γ rays. The remaining nucleus continues to recoil with its velocity unchanged but reduced in momentum.

For any given beam / target combination, several activities are produced. Many factors have to be considered in making a choice of beam and target. Firstly, target materials must be able to with stand the impact of the beam and the extreme temperatures (~1500 °C) near the ion-source. Secondly, the cross sections for the reactions which produce the desired residues must be favorable. Estimates of the cross sections were made using the computer code "ALICE OVERLAID" [Bl78]. These estimates (for primary cases) are subsequently tested in a "target run".

The nuclei produced in the target run are listed in table 3.1. In this target run, iodine is only one mass measurement candidate of several. The target run investigation seeks to fulfill two criteria for a candidate mass measurement. The first, of course, is an adequate production rate for nuclei, far from stability, without a known mass. Secondly, we need a neighboring nuclei, with a known mass, that can be used as a reference.

Table 3.1. Beam and target combinations and their expected products for the "target run". The energy of the incident beam is varied from 120 - 150 MeV in 10 MeV intervals. (The mean energy of the beam is reduced by ~12 MeV over the thickness of the target.)

Beam + Target	Compound Nucleus	Products far from Stability
$^{27}Al + {}^{nat}Zr$	I	Te or Sb
$^{28}Si + {}^{nat}Zr$	Xe	I or Te
$^{27}Al + {}^{nat}Mo$	Cs	Xe or I
$^{28}Si + {}^{nat}Mo$	Ba	Cs or Xe

target thickness; ^{nat}Zr: 2.0 mg-cm^{-2}, ^{nat}Mo: 2.1 mg-cm^{-2}.

Here we focus our attention on the results obtained for the production of $^{119,118,117}I$. These iodine activities were observed with ^{28}Si and ^{27}Al beams on ^{nat}Zr and ^{nat}Mo targets. The rates of the iodine activities produced by the various beam and target combinations are shown in fig. 3.2.

We see from fig. 3.2 that the most effective beam / target combination is an ^{27}Al beam and a ^{nat}Mo target. The selection of the beam energy is dictated by the production rate of the low yield odd *Z*-odd *N* nucleus ^{118}I. The ^{118}I production shows a maximum at 130 MeV. Since the other nuclides of interest are also produced at acceptable rates at this energy, this becomes our operating energy for the mass measurement experiment.

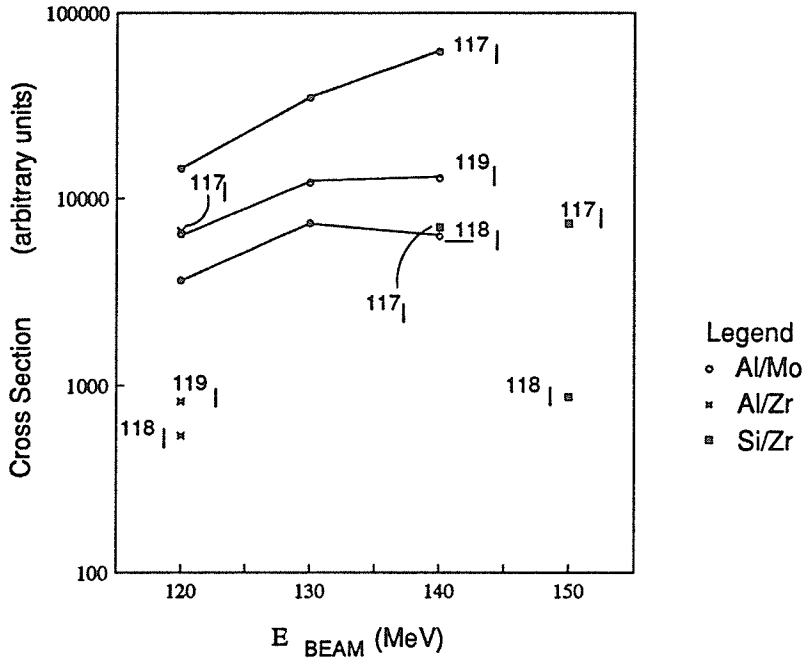

Fig. 3.2. Measured excitation functions for the production of iodine. The observed iodine activities from the target run are normalized to the incident beam current and plotted against beam energy. The cross-sections are given in arbitrary units since we have not corrected for the common efficiency of the ion source, detector, and others.

The target thickness is optimized for maximum ion production, given that the iodine product must still exit the target with enough energy to pass though the heat shields and entrance window of the ion source. A minor change of target thickness from 2.1 mg-cm^{-2} to 2.5 mg-cm^{-2} could have been made. However, the expected improvement in iodine

production did not warrant the effort to manufacture new targets. The molybdenum targets showed no degradation during the four days of the target run and were used for the four day mass measurement experiment.

The mass measurement experiment using the reaction $^{27}Al + {}^{nat.}Mo \rightarrow {}^{117\text{-}119}I + 2p + xn + \gamma$, $E_{Al} = 133$ MeV produced xenon and iodine activities as expected. No cesium activities were observed. However a limit on their production, based on background levels, has been calculated. The production data in table 3.2 are in units of atoms per second, observed at the counting chamber (i.e. the tape station).

Table 3.2. Chart of production of isotopes at the location of the tape station in atoms per second. Cesium is not observed. Its production value is based on a limit from the background level in the γ-ray spectra.

^{117}Cs 8.4s *< 55 /s*	^{118}Cs 17s *< 6.0 /s*	^{119}Cs 43.0s *< 0.4 /s*			
	^{117}Xe 61s *116 /s*	^{118}Xe 6m *143 /s*	^{119}Xe 5.8m *553 /s*		
		^{117}I 2.22m *1450 /s*	^{118m}I 8.5m *264*	^{118}I 13.7m *1270*	^{119}I 19.1m *2232 /s*

3.2 Run summary

We performed 17 mass-triplet scans (runs) over a period of four days, from which a subset of 9 scans were accepted for analysis. Problems such as high voltage discharges in the ion source or interruptions in the primary ^{27}Al beam would disqualify a run.

3.3 Gamma rays

The mass spectra are built from the intensity of selected γ-rays emitted during the decay of the iodine nuclei. The selection of the γ-rays is based on two criteria. The first is that the γ-ray transition energy be unique to the iodine decay. Other activities that would emit a γ-ray of nearly the same transition energy would mis-represent the iodine activity and thus contaminate the iodine mass spectrum. The case for uniqueness was occasionally ever-ridden if the source of the γ-ray is from room background. Such a source would only contribute a flat level to the generated mass spectrum (see §3.7.1). The centroid of the spectrum is not affected, but the uncertainty to which the centroid can be determined is increased due to a decrease in the "signal-to-noise" ratio of mass peak signal to the background level.

The second criteria is to chose the most intense γ-ray transition, or transitions, associated with the decay of the iodine nucleus. The iodine isotopes of interest decay by positron emission (β^+), orbital electron capture (EC), and in the case of ^{118}I, isomeric transition (IT). The process from which the emitted γ-rays arises is not important.

On the basis of the criteria mentioned above, we selected the iodine γ-rays presented in table 3.3. The most intense γ-ray transition available is used in all cases. The main γ-ray characteristic of ^{118}I is unfortunately degenerate with a γ-ray from the iodine isomer ^{118m}I. The next most intense line for ^{118}I occurs with an 8.1% relative branch. This is too low for acceptable counting statistics. In the case of ^{117}I we were able to use two γ-ray transitions in order to improve the counting statistics.

Table 3.3. Selected iodine γ-rays that are used to build the iodine mass spectra. The γ-rays arise from excited states in tellurium that have been populated by β^+ and EC decays of the iodine nucleus. The selection of the γ-rays is based on uniqueness and intensity (see text for details).

Isotope	γ(Te) Energy (keV)	I_γ (relative intensity,%)	Reference
^{119}I	257.5	100	[NN92]
^{118}I	605.6	100	[Ta87]
^{117}I	325.9	100	[Bl87]
	274.4	27	[Bl87]

An off-line sum of all individual experimental γ-ray spectra is compiled in order to inspect the transitions associated with iodine and other activities. Six sum γ-ray spectra are compiled according to the detector (1,2) and mass number (A=119,118,117). Sum γ-ray spectra are presented in figs. 3.3 - 3.5. Regions around the selected transition energies listed table 3.3 have been expanded for detailed inspection.

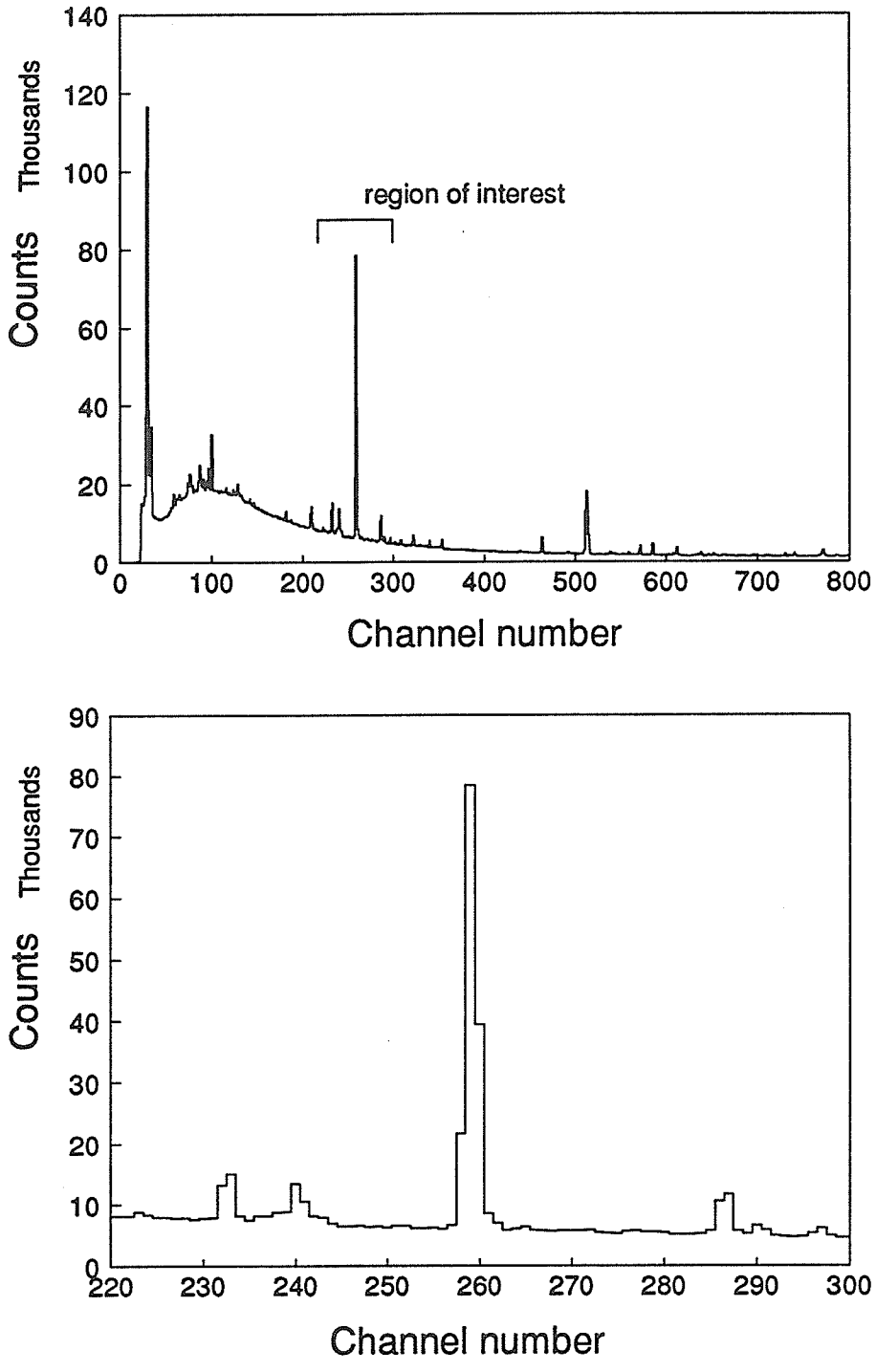

Fig. 3.3. Mass specific γ-ray spectrum for A = 119. The spectrum represents the sum of mass specific γ spectra over 13 runs. The channel axis is set to represent 1 keV per channel (see Appendix B).

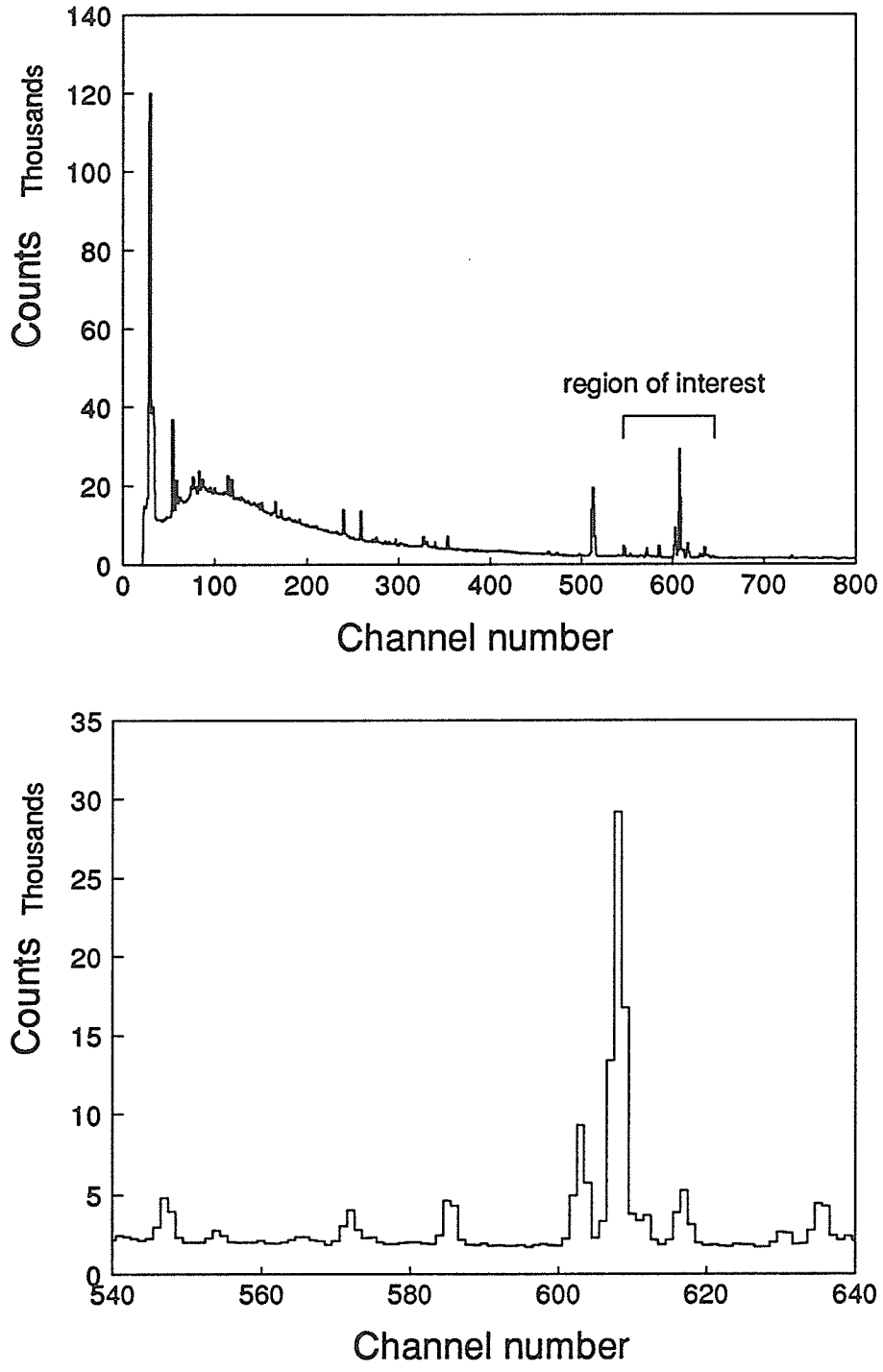

Fig. 3.4. Mass specific γ-ray spectrum for A = 118. The spectrum represents the sum of mass specific γ spectra over 13 runs. The channel axis is set to represent 1 keV per channel (see Appendix B).

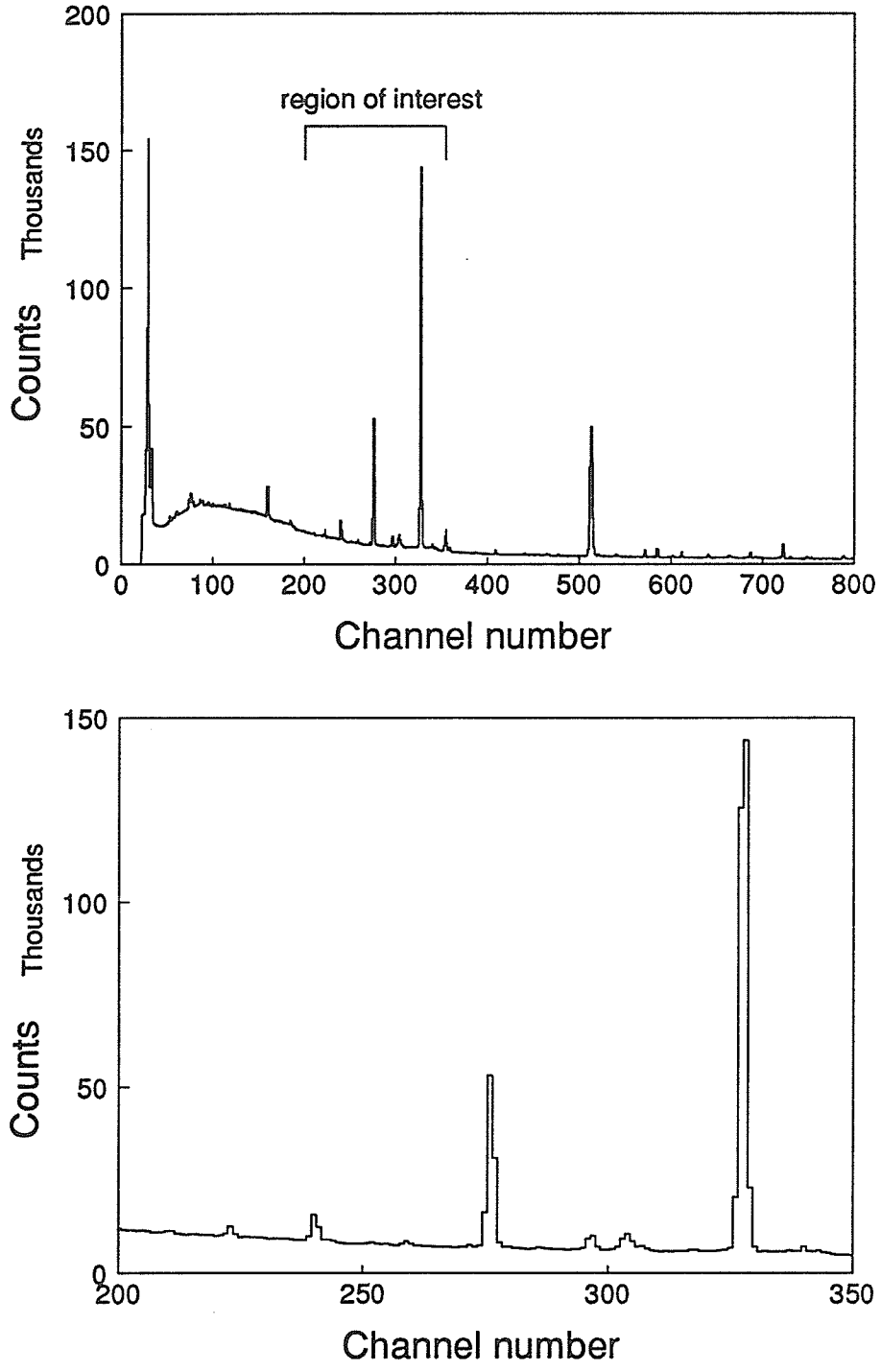

Fig. 3.5. Mass specific γ-ray spectrum for A = 117. The spectrum represents the sum of mass specific γ spectra over 13 runs. The channel axis is set to represent 1 keV per channel (see Appendix B).

3.4 Mass spectra

Using the selected γ-rays (table 3.3), and the γ-ray data acquired during the mass measurement experiment, the iodine mass spectra are generated. The mass spectrum from run 6 is shown in fig. 3.6, as a sample. The observed intensities of the three isotopes reflect the production rates of table 3.1 and the relative efficiency of detection. The observed peaks show some asymmetry on the heavy mass (low energy) side of the peak. However, the shift in the peak position introduced by an asymmetric peak shape is not expected to shift the measured mass ratio by more than one part per million. The shift in the measured mass ratio is less than this. Our present level of precision, by comparison, is about 2 ppm per mass peak (see table 3.4).

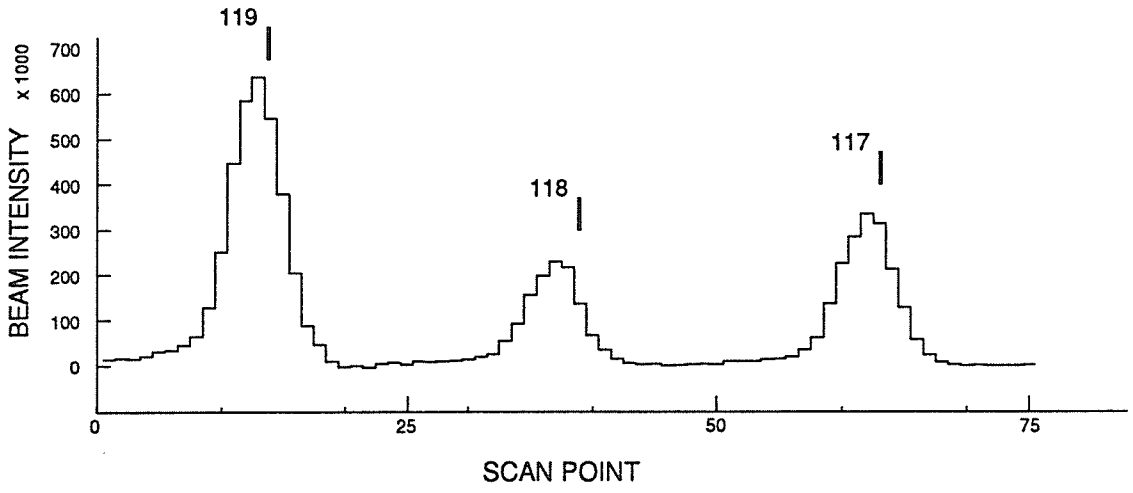

Fig. 3.6. Mass spectrum obtained during run 6. The individual mass spectra from each selected γ-ray energy have been summed to create this spectrum.

3.5 Uncorrected voltage ratios

The peak positions in the mass spectrum corresponding to ^{119}I, ^{118}I, and ^{117}I are found by calculating the centroid of the mass spectrum at each isotope number (refer §2.2.2.3). The peak positions are in the units of volts. (For example, the peak position corresponding to ^{119}I is labeled V_{119}). The peak positions for the iodine isotopes are given in table 3.4, along with their statistical and voltage uncertainties. The overall uncertainty is obtained by summing the statistical and voltage uncertainties in quadrature.

Since the peak positions are expressed in the units of volts, we label the ratios of peak positions "voltage ratios". The voltage ratios of interest are $\frac{V_{119}}{V_{118}}$ and $\frac{V_{119}}{V_{117}}$ (see equation (3.6)). The voltage ratios are calculated for each run and presented in table 3.5. The uncertainty in the voltage ratio is found simply using the fractional error rule for a quotient:

$$\text{e. g.} \qquad \sigma\left(\frac{V_{119}}{V_{118}}\right)=\frac{V_{119}}{V_{118}}\sqrt{\frac{\sigma^2_{\text{overall}}(V_{119})}{V^2_{119}}+\frac{\sigma^2_{\text{overall}}(V_{118})}{V^2_{118}}} \quad . \tag{3.1}$$

Table 3.4. Iodine mass peak positions. The positions are found by calculating the centroid of the mass spectrum at each isotope number. (refer §2.2.2.3; program MASSDIF)

Run	Mass Number	Centroid (volts)	Statistical Uncertainty	Voltage Uncertainty	Overall Uncertainty
3	119	39780.500	0.036	0.080	0.088
	118	40116.750	0.041	0.085	0.094
	117	40459.785	0.016	0.077	0.079
5	119	39779.883	0.021	0.077	0.080
	118	40116.445	0.026	0.085	0.089
	117	40459.207	0.012	0.082	0.083
6	119	39780.238	0.019	0.080	0.082
	118	40116.695	0.025	0.084	0.088
	117	40459.414	0.012	0.080	0.081
8	119	39779.930	0.022	0.077	0.080
	118	40116.309	0.029	0.079	0.084
	117	40459.137	0.013	0.076	0.077
9	119	39780.227	0.020	0.077	0.080
	118	40116.578	0.025	0.080	0.084
	117	40459.359	0.013	0.081	0.082
10	119	39780.227	0.026	0.080	0.084
	118	40116.758	0.028	0.083	0.088
	117	40459.594	0.013	0.076	0.077
13	119	39779.418	0.030	0.082	0.087
	118	40115.844	0.036	0.085	0.092
	117	40458.512	0.017	0.078	0.080
17.1	119	39780.465	0.030	0.079	0.085
	118	40116.973	0.037	0.076	0.085
	117	40459.738	0.016	0.072	0.074
17.2	119	39780.605	0.028	0.080	0.085
	118	40117.027	0.035	0.114	0.119
	117	40459.824	0.016	0.072	0.074

Table 3.5. (A) Voltage ratios calculated from the peak position data of table 3.4. A sample calculation for the error is given in equation (3.1).

(B) Measured voltage ratios from the centroid data. The statistical uncertainty, being the larger of the two uncertainties, is carried forward for future calculations.

(A) Run	$\frac{V_{119}}{V_{118}}$	$\sigma\left(\frac{V_{119}}{V_{118}}\right)$	$\frac{V_{119}}{V_{117}}$	$\sigma\left(\frac{V_{119}}{V_{117}}\right)$
3	0.991 618 2	0.000 003 2	0.983 210 0	0.000 002 9
5	0.991 610 4	0.000 003 0	0.983 209 7	0.000 002 8
6	0.991 613 0	0.000 003 0	0.983 213 4	0.000 002 8
8	0.991 614 9	0.000 002 9	0.983 212 5	0.000 002 7
9	0.991 615 7	0.000 002 8	0.983 214 5	0.000 002 8
10	0.991 611 6	0.000 003 0	0.983 208 8	0.000 002 8
13	0.991 613 8	0.000 003 1	0.983 215 1	0.000 002 9
17.1	0.991 611 2	0.000 003 0	0.983 211 1	0.000 002 8
17.2	0.991 614 0	0.000 003 6	0.983 212 5	0.000 002 8
(B) Weighted Average	0.991 613 61		0.983 212 03	
Statistical Uncertainty		1.02×10^{-6}		0.94×10^{-6}
Estimated Systematic Uncertainty		0.81×10^{-6}		0.70×10^{-6}
χ^2_ν		0.79		0.75

From the data given in table 3.5(A), a weighted average is taken to obtain one voltage ratio for each of $\frac{V_{119}}{V_{118}}$ and $\frac{V_{119}}{V_{117}}$. The weighted average formula is given by equation (3.2). The weighted average results are given in table 3.5(B).

$$\bar{x}_{\text{weighted}} = \frac{\sum w_i x_i}{\sum w_i} \quad , \quad w_i = \frac{1}{\sigma_i^2} \tag{3.2}$$

The uncertainty associated with the weighted average is estimated in two different ways. The first is the *statistical uncertainty*, found by summing the weights associated with each datum, as given by equation (3.3). The statistical uncertainty is sometimes called the internal error. The second is the *estimated systematic uncertainty*, found by examining the dispersion of data points about the weighted average, as given by equation (3.4). The estimated systematic uncertainty is sometimes called the external error. The statistical and estimated systematic uncertainties of the voltage ratios $\frac{V_{119}}{V_{118}}$ and $\frac{V_{119}}{V_{117}}$ are also presented in table 3.5.

$$\sigma^2_{\text{statistical}} = \frac{1}{\sum \frac{1}{\sigma_i^2}} = \frac{1}{\sum w_i} \tag{3.3}$$

$$\sigma^2_{\text{estimated systematic}} = \frac{\sum [\, w_i \, (x_i - \bar{x}_{\text{weighted}})^2 \,]}{(N-1) \sum w_i} \tag{3.4}$$

We calculate the value of the reduced chi-square, χ^2_ν, by dividing the estimated systematic uncertainty by the statistical uncertainty (see equation (3.5)). The numerator of equation (3.5) corresponds to the dispersion of data points. The denominator corresponds to the expected dispersion. Our values of the reduced chi-square, $\chi^2_\nu = 0.79$ for $\frac{V_{119}}{V_{118}}$ and $\chi^2_\nu = 0.75$ for $\frac{V_{119}}{V_{117}}$ indicate that the uncertainty we have assigned each data point is larger than that warranted by the dispersion of the data points. Nevertheless, the statistical uncertainty, the more conservative estimate, is selected as the uncertainty associated with the weighted averages of $\frac{V_{119}}{V_{118}}$ and $\frac{V_{119}}{V_{117}}$.

$$\chi^2_\nu = \frac{\sum w_i \, (x_i - \bar{x}_{\text{weighted}})^2}{(N-1)} \tag{3.5}$$

where $x_i \pm \sigma_i = \left[\frac{V_{119}}{V_{118}}\right]_i \pm \left[\sigma\left(\frac{V_{119}}{V_{118}}\right)\right]_i$ for i=1, ..., 9 (=N). Similar equations follow for the voltage ratio $\frac{V_{119}}{V_{117}}$.

3.6 Uncorrected masses

We are now in a position to determine the mass of ^{118}I and ^{117}I. Experimentally we have measured the voltage ratios $\frac{V_{119}}{V_{118}}$ and $\frac{V_{119}}{V_{117}}$ corresponding to iodine ions beams $^{119}I^+$, $^{118}I^+$, and $^{117}I^+$. Using Bleakney's Theorem (refer §2.2) with the known ^{119}I mass allows us to determine the unknown mass of ^{118}I and ^{117}I. The masses are given by equation (3.6) where the binding energy of the valance electron has been neglected.

$$\begin{aligned} M(^{119}I^+) &= M(^{119}I) - M(e^-), \\ M(^{118}I^+) &= M(^{118}I)_{\text{uncorrected}} - M(e^-), \\ M(^{117}I^+) &= M(^{117}I)_{\text{uncorrected}} - M(e^-). \end{aligned} \tag{3.6}$$

Thus

$$\begin{aligned} M(^{118}I)_{\text{uncorrected}} &= M(^{119}I)\left(\frac{V_{119}}{V_{118}}\right) + M(e^-)\left(1-\frac{V_{119}}{V_{118}}\right) \\ &= 117\,912\,836 \pm 159 \ \mu u \ , \end{aligned} \tag{3.7}$$

and

$$\begin{aligned} M(^{117}I)_{\text{uncorrected}} &= M(^{119}I)\left(\frac{V_{119}}{V_{117}}\right) + M(e^-)\left(1-\frac{V_{119}}{V_{117}}\right) \\ &= 116\,913\,808 \pm 152 \ \mu u \ . \end{aligned} \tag{3.8}$$

where $M(^{119}I) = 118\,910\,057 \pm 103$ μu [Wa88] and $M(e^-) = 548.579\,903(13)$ μu [Co87]. The uncertainty for $M(^{118}I)_{\text{uncorrected}}$ was determined with equation (3.9). The uncertainty for $M(^{117}I)_{\text{uncorrected}}$ follows in a similar way.

e.g.

$$\sigma\left(M(^{118}I)_{\text{uncorrected}}\right) = M(^{118}I)_{\text{uncorrected}} \sqrt{\frac{\sigma^2(M(^{119}I))}{M(^{119}I)^2} + \frac{\sigma^2\left(\frac{V_{119}}{V_{118}}\right)_{\text{Statistical}}}{\left(\frac{V_{119}}{V_{118}}\right)^2}} \ . \tag{3.9}$$

From the production data of table 3.1, we know that the separator beam contains xenon and isomeric iodine activities in addition to iodine nuclides in their ground state. Consequently, the measured iodine voltage ratios require corrections for the presence of these activities.

3.7 Contaminant feeding

3.7.1 Contaminant feeding processes

There are up to four processes which contaminate our mass spectra. The purpose of this section is to introduce these processes and discuss how they affect the generated mass spectra. In all cases it is possible to appraise the level of contamination and apply corrections where necessary.

The mass spectra are influenced whenever the energies of the γ-rays selected to generate the mass spectra coincide with those of γ-rays that are present from other processes. The other processes include room background, the decay of other nuclei that were produced by the separator, the decay of iodine atoms that are produced by the decay of nuclei higher in the ß-decay chain, and the decay of isomeric states of the iodine isotopes themselves.

The first source of contamination to be discussed arises from room background sources. The γ-ray decay energy of a background transition may coincide with a γ-ray selected to generate the iodine mass spectrum. The raw γ-ray spectrum thus contains a background component that accumulates linearly with time, assuming the background level does not fluctuate. Since we acquire each γ-ray spectrum for a nearly identical amount of time (± 0.02%), the effect on the mass spectrum is to evenly raise the background level over all mass spectral channels. Although this marginally decreases the signal-to-noise ratio of the mass peak, it does not affect the centroid determination of the peak position.

The second and third sources of contamination originate from the production of isobaric nuclei other than iodine (refer table 3.2). In the second case, if the γ-ray transition from a decay branch in a contaminant's decay scheme is energetically close to the selected iodine's γ-ray decay signature, the measured mass peak position is shifted in the direction of the contaminant mass. Carefully chosen "unique" iodine γ-ray energies eliminate this form of contamination. However, there are two cases where the use of contaminated iodine γ-ray energies is unavoidable.

The presence of ^{119}Cs among the activities produced by the separator would influence the measured mass of ^{119}I. One of the radioactive decay channels of ^{119}Cs is a 257 keV γ-ray, with a 57% relative branching ratio, $Cs^{beam} \rightarrow Xe + \gamma(257\ keV)$. This would contaminate our 257 keV gate for ^{119}I (refer table 3.3). This particular ^{119}I gate must be used since the next most intense iodine decay, at 320 keV, has only a 2.2% relative branching ratio. Such a low branching ratio is insufficient for use as a single reference of iodine production. However, no trace of the ^{119}Cs activity is visible in the mass-specific γ-ray spectrum corresponding to $A = 119$. It is possible to place an upper limit on the production rate of ^{119}Cs based on the background levels present in the γ-ray spectrum in the vicinity of the expected location of the various Cs γ-ray peaks. This in turn could be used to estimate a limit of the influence of this on the measured masses. The second case of a contaminating γ-ray energy is that from ^{118m}I by the decay, $^{118m}I \rightarrow Te + \gamma(605\ keV)$, with a 100% relative branching ratio and a 109% absolute branching ratio (the 605 keV transition arises from more than one level decay in Te*). This 605 keV decay energy interferes with the ^{118}I decay signature (refer table 3.3). A correction for this source of feeding is successfully applied (see table 3.10).

The third source of contamination arises from parent-daughter and possibly grandparent-daughter feeding to the iodine population. A parent-daughter decay chain feeds the iodine population by a single β^+ decay, $Xe \rightarrow I^* + e^+ + \nu$. The observed iodine population is indistinguishable as to whether it originated from iodine of the separator beam or from β^+ decays of xenon nuclei after xenon is deposited on the same tape sample. The xenon-fed component in the iodine population biases the mass peak centroid toward the heavier mass of xenon. We have assumed that the xenon β^+ decay channel does not populate the isomeric state of iodine [Sh85]. i.e. the isomeric state is populated directly by the reaction used in the decay of compound nuclei $^{127\text{-}119}Cs$. The parent-daughter feeding is common to all the isotopes of iodine studied. A correction is applied at each mass number to the iodine mass in a calculation described in §3.7.2.

A similar scenario could hypothetically exist for grandparent-daughter feeding (i.e.Cs $\rightarrow$ Xe $\rightarrow$ I) through a chain of two β^+ decays. The correction for grandparent-daughter feeding is estimated at each mass number but *not applied* to the iodine mass correction calculation, as no evidence of cesium is found in the γ-ray spectra.

The fourth and final contamination arises from iodine isomeric transitions to the iodine ground state. Similar to parent-daughter feeding, the isomer decays feed the ground state population which biases the resulting mass spectra toward the (heavier) isomeric state mass. Again a correction is successfully applied (see table 3.10). A summary of corrections is presented in the table on the following page.

Table 3.6. Isobaric contaminant summary for the iodine masses at A = 119, 118, 117. No evidence for cesium contamination is found in the γ-ray spectra. The contamination processes that could arise from cesium production are enclosed by brackets.

Mass Number	Description of contaminant feeding processes.	
119	(Cesium grandparent-daughter feeding.	$^{119}Cs^{beam} \rightarrow {}^{119}Xe \rightarrow {}^{119}I$)
	(Cesium contaminant γ-ray.	$^{119}Cs^{beam} \rightarrow {}^{119}Xe + \gamma$)
	1. Xenon parent-daughter feeding.	$^{119}Xe^{beam} \rightarrow {}^{119}I$
118	(Cesium grandparent-daughter feeding.	$^{118}Cs^{beam} \rightarrow {}^{118}Xe \rightarrow {}^{118g}I$)
	1. Xenon parent-daughter feeding.	$^{118}Xe^{beam} \rightarrow {}^{118g}I$
	2. Iodine isomer contaminant γ-ray.	$^{118m}I^{beam} \rightarrow {}^{118}Te + \gamma$
	3. Iodine isomer parent-daughter feeding.	$^{118m}I^{beam} \rightarrow {}^{118g}I$
117	(Cesium grandparent-daughter feeding.	$^{117}Cs^{beam} \rightarrow {}^{117}Xe \rightarrow {}^{117}I$)
	1. Xenon parent-daughter feeding.	$^{117}Xe^{beam} \rightarrow {}^{117}I$

3.7.2 Corrections

Each contaminant will add an extra component to the iodine mass spectrum. An analytical form for the mass spectrum, either as a single iodine component, or a sum of components is very difficult to obtain. Instead we use a weighted centroid average to describe the effect on the peak position of a multi-component mass spectrum. The position of the mass spectral peak, M_A, at mass number A may be written as an intensity weighted mass average,

$$M_A = \frac{\sum_Z [\, C_Z^A \, M({}^A Z)\,]}{\sum_Z C_Z^A} \quad , \tag{3.10}$$

where the coefficients C_Z^A represent the intensity of each component, and $M\,({}^A Z)$, the mass of each component. For example, consider a mass spectrum consisting of three

closely spaced components. The position and intensity for the three mass components is shown schematically in fig. 3.7. Their positions are equally spaced on the mass axis, and the ratio of their intensities is 1 : 2 : 5. The position of the observed mass peak, as determined by a weighted average, is identified by the thick line.

The (contaminated) iodine mass we measure is analogous to the thick line in fig. 3.7. The analogous weighted average is given by equation (3.11). The net shift, or correction on the mass axis, due to contaminants is given in this equation by ΔM_A. The corrections ΔM_{119}, ΔM_{118}, and ΔM_{117} are calculated in the following pages and then applied to the (contaminated) measured mass of iodine in the following section.

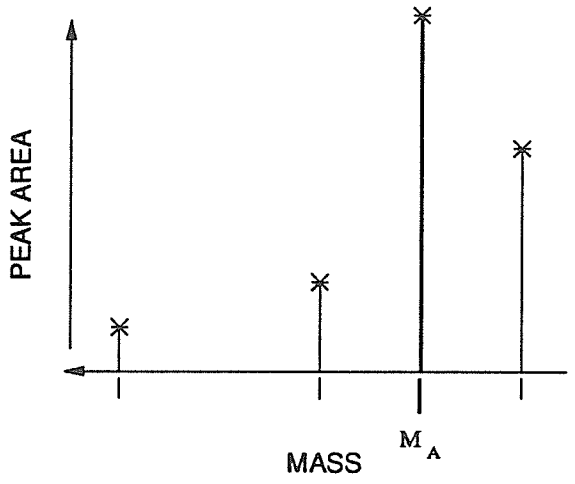

Fig. 3.7. A representation of the position and intensity of iodine and contaminant components that compose the observed mass peak (thick line). The components (for the purposes of this example) are equally spaced on the mass axis (thin tick marks = peak positions). The intensity of the observed mass peak is the sum of the component intensities. Its position on the mass axis, M_A, (thick tick mark) is determined by an intensity weighted mass average of the component peak positions.

$$M_A = \frac{C_{\mathrm{I}}^A\, M(^A\mathrm{I}) + C_{\mathrm{Xe}}^A M(^A\mathrm{Xe}) + \ldots}{\sum_Z C_Z^A} \tag{3.11a}$$

or

$$M_A = M(^A\mathrm{I}) + \Delta M_A \quad , \quad \text{where} \quad \Delta M_A = \frac{\sum_Z C_Z^A\, [\, M(^A Z) - M(^A\mathrm{I})\,]}{\sum_Z C_Z^A} \quad . \tag{3.11b}$$

The coefficients, C_Z^A, are determined from the off-line summary of experimental γ-ray data (refer §3.3). In table 3.7 we summarize the contaminant and iodine activities found in this γ-ray data. A unique γ-ray decay signature is used to identify cesium, xenon, and iodine activities. In the table, the observed number of decays at the signature γ-ray energy are recorded and then corrected for absolute branching ratio and detector efficiency in order to find the number of decays of the parent population.

For example, the sum of coefficients term, $\sum_Z C_Z^A$, represents the total number of observed decays at the iodine decay energy, irrespective of their origin. That is, most of these decays originate from iodine of the separator beam, C_{I}, and some arise from parent-daughter feeding, C_{Xe}. The C_Z coefficients are labeled in the γ-ray contamination decay schemes in figs. 3.8, 3.9, 3.10.

Table 3.7. Observed activities of iodine, xenon, and cesium from the γ-ray summaries at mass numbers A = 119, 118, 117 (see §3.3). The γ-ray summaries consists of all γ-ray spectra collected when the tape sample is moved in front of the detectors (i.e. during the COUNT portion of the measurement cycle (refer fig. 2.11)).

Nuclide	E_γ (keV)	Area under peak#	Error or {Bkgnd. Level}	$I_{\gamma,\text{rel.}}$ (%)	$I_{\gamma,\text{abs.}/@}$	Reference	$\varepsilon_{\text{detector}}$ (%)	Number of Parent Decays!
^{119g}Cs	176	-	{11000}	≈81	nda	[NN92]	12.5	< 1 037*
	257	-		57	nda		9	-
^{119}Xe	96	8 535	±255	38	4.18	[NN92]	20	1 020 933
^{119}I	257	122 987	±492	100	86.7	[NN92]	9	1 576 150
^{118}Cs	590	-	{1700}	12.8	nda	[Ta87]	4.6	< 6 963*
^{118}Xe	53	51 946	±857	(100)	nda	[Ta87]	20	259 730*
	117	7 569	±334	(100)	nda		17	44 523*
^{118g}I	605	63 351	±367	78&	83.5	[Ta87]	4.4	-
	1338	2 364	±114	8.11	8.7		2.3	1 181 409
^{118m}I	I.T. 114	10 330	±547	4.0T.W.	nda	[Ta87]	18	-
	605	-	-	22&	109		4.4	-
	614	7 946	±130	11.4	56		4.4	322 484
	929	1 031	±159	1.66	8.2		3.1	405 586
	944	2 029	±183	3.49	17.2		3.1	380 533
	1093	1 138	±125	2.48	12.3		2.7	342 668
^{117}Cs	271	-	{7067}	28.5	4.3	[Bl87]	8.5	< 23 116*
^{117}Xe	221	3 988	±204	100	10	[Bl87]	10.5	379 810
^{117}I	274	81 352	±421	27	21	[Bl87]	8.5	4 557 535
	325	288 579	±728	100	78		7.5	4 932 974

nda no data available

@ absolute intensity per 100 parent decays

! decays during the COUNT portion of the measurement cycle only

& from the proposed decay scheme for 13.7-min and 8.5-min combined isomers

* estimated

background subtracted

( ) assumed value

T.W. this work

We now consider the contamination present at mass number $A = 119$. The measured centroid for the $A = 119$ mass spectra represents the weighted average of iodine and xenon components (refer table 3.6). The mass corresponding to the measured centroid is given by

$$M_{119} = \frac{C_{Xe} M(^{119}\mathrm{Xe}) + C_I M(^{119}\mathrm{I})}{\sum_Z C_Z} \quad , \tag{3.12}$$

where C_{Xe} = parent-daughter feeding $\quad Xe^{beam} \rightarrow I$,

C_I = iodine component $\quad I^{beam}$,

$\sum_Z C_Z$ = sum of the coefficients .

The net contaminant correction, ΔM_{119}, may be identified as in equation (3.11b), if we write equation (3.12) as

$$M_{119} = M(^{119}\mathrm{I}) + \Delta M_{119} \quad , \tag{3.13a}$$

where

$$\Delta M_{119} = \frac{C_{Xe}}{\sum_Z C_Z} [\, M(^{119}\mathrm{Xe}) - M(^{119}\mathrm{I}) \,] \quad . \tag{3.13b}$$

The effect of the heavier isobar, ^{119}Xe, is to shift the ^{119}I centroid to a more massive value, that is $\Delta M_{119} > 0$. From table 3.7 we find $\sum_Z C_Z^{119} = 122\,987 \pm 492$. The coefficient for xenon parent-daughter feeding, C_{Xe}, is not directly obtained from table 3.7, but calculated from the observed xenon activity found there.

To begin the evaluation of C_{Xe}, we record the number of parent decays of the xenon contaminant from table 3.7. Knowing the decay constant and the measurement cycle times involved, we interpolate to the COLLECT portion of the measurement cycle and find the xenon production. Once the xenon production is known, we use the decay constant and cycle times again to determine the number of the iodine decays in the COUNT interval that are due to xenon parent feeding. The computer code RATE3 is used for this calcula-

tion. A description of the RATE3 program is given in Appendix A. From this calculation we find the number of observed iodine decays that are due to xenon feeding is C_{Xe} = 7 511. As a conservative estimate, we assign an uncertainty of ± 20% to this coefficient.

The coefficients for the contaminant corrections used in the evaluation of ΔM_{119} are found in table 3.8. A summary of the correction calculation is given in table 3.9. The ^{119}I mass correction, ΔM_{119}, is 330.0 ± 66.9 μu .

Table 3.8. Summary of the coefficients used in the evaluation of the contaminant correction, equation (3.11b).

Contaminant Source	Counts in the Iodine Decay Signature		Contaminant Label and Description
^{119}I :			
^{119}Cs	< 2	± 20%	C_{Cs} : ^{119}I populated via ^{119}Cs ß$^+$ß$^+$ grandparent-parent-daughter feeding
^{119}Cs	< 53	± 20%	$C_{Cs,\gamma}$: γ(Xe) from ^{119}Cs ß$^+$ decays which contaminate the ^{119}I decay signature @ 257 keV
^{119}Xe	7 511	± 20%	C_{Xe} : ^{119}I populated from ^{119}Xe ß$^+$ parent-daughter feeding
	122 987	± 492	$\sum_Z C_Z$: Total counts in the ^{119}I decay signature
^{118}I :			
^{118}Cs	< 37	± 20%	C_{Cs} : ^{118g}I populated via ^{118}Cs ß$^+$ß$^+$ grandparent-parent-daughter feeding
^{118}Xe	1 224	± 20%	C_{Xe} : ^{118g}I populated via ^{118}Xe ß$^+$ parent-daughter feeding
^{118m}I	1 652	± 20%	C_{mI} : ^{118g}I populated via ^{118m}I isomeric transitions
^{118m}I	17 400	± 20%	$C_{mI,\gamma}$: γ(Te) from ^{118m}I ß$^+$ decays which contaminate the ^{118g}I decay signature @ 605 keV
	63 351	± 367	$\sum_Z C_Z$: Total counts in the ^{118g}I decay signature
^{117}I :			
^{117}Cs	< 11 122	± 20%	C_{Cs} : ^{117}I populated via ^{117}Cs ß$^+$ß$^+$ grandparent-parent-daughter feeding
^{117}Xe	26 703	± 20%	C_{Xe} : ^{117}I populated via ^{117}Xe ß$^+$ parent-daughter feeding
	369 931	± 841	$\sum_Z C_Z$: Total counts in the ^{117}I decay signature

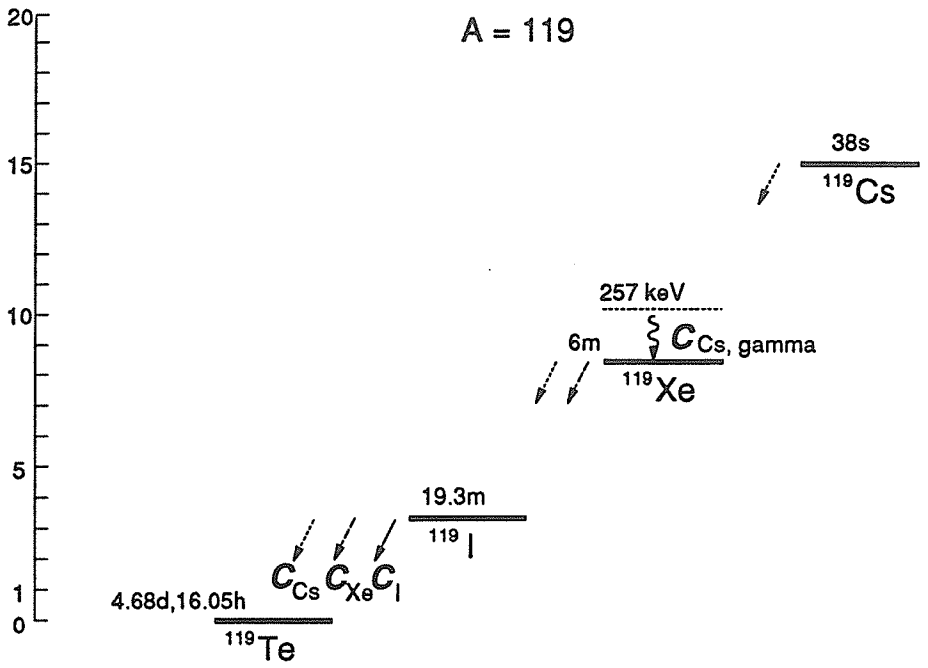

Fig. 3.8. Decay scheme and contaminants (bold italics) at mass number A = 119 in the ^{119}I mass correction. The vertical energy scale is in units of MeV. (The 257 keV state has been expanded for clarity.) The contaminants have previously been identified in § 3.7.1.

Table 3.9. Corrections at mass number A = 119. The contaminant ^{119}Cs was not observed in the experiment. The values for ^{119}Cs are based on background limits in the γ-ray spectra. ^{119}Cs corrections are not applied to the calculation of ΔM_{119}.

Reference masses [Wa88]			
$M(^{119}\mathrm{I})$		118 910 056.916 ± 103.124 μu	
$M(^{119}\mathrm{Xe})$		118 915 459.709 ± 149.872 μu	
$M(^{119}\mathrm{Cs})$		118 922 447.818 ± 110.067 μu	
Corrections			
Nuclide	Feeding to I (%)	Correction(μu)	Source
^{119}Cs	< 0.002	(< 0.201 ± 0.003)	$^{119}\mathrm{Cs}^{\mathrm{beam}}$ β⁺β⁺
^{119}Cs	< 0.043	(< 5.350 ± 1.110)	γ(Xe) from ^{119}Cs β⁺
^{119}Xe	6.1	329.957 ± 66.924	$^{119}\mathrm{Xe}^{\mathrm{beam}}$ β⁺
Total		ΔM_{119} = 329.957 ± 66.924	

Next, consider the contamination present in the ^{118}I mass spectra. The mass corresponding to the measured centroid is given by

$$M_{118} = \frac{C_{Xe} M(^{118}\mathrm{Xe}) + (C_{m_I} + C_{m_{I,\gamma}}) M(^{118m}\mathrm{I}) + C_{g_I} M(^{118g}\mathrm{I})}{\sum_Z C_Z} \quad , \tag{3.14}$$

where C_{Xe} = parent-daughter feeding $\mathrm{Xe}^{beam} \rightarrow {}^{118g}\mathrm{I}$,

C_{m_I} = contaminant γ-ray from the isomer decay $^{118m}\mathrm{I} \rightarrow \mathrm{Te} + \gamma$,

$C_{m_{I,\gamma}}$ = isomeric transition $^{118m}\mathrm{I}^{beam} \rightarrow {}^{118g}\mathrm{I}$,

C_{g_I} = main mass component $^{118g}\mathrm{I}^{beam}$,

$\sum_Z C_Z$ = sum of the coefficients .

The weighted average formula is re-written to identify the contributions of ^{118g}I and contaminants as

$$M_{118} = M(^{118g}\mathrm{I}) + \Delta M_{118} \quad , \tag{3.15a}$$

where

$$\Delta M_{118} = \frac{C_{Xe}}{\sum_Z C_Z} [\, M(^{118}\mathrm{Xe}) - M(^{118g}\mathrm{I})] + \frac{C_{m_I} + C_{m_{I,\gamma}}}{\sum_Z C_Z} [\, E_{\text{internal transition}} \,] \quad , \tag{3.15b}$$

and

$$E_{\text{internal transition}} = [\, M(^{118m}\mathrm{I}) - M(^{118g}\mathrm{I}) \,] \times 931.494\,32(28) \quad \mathrm{MeV/c^2 - u} \quad . \tag{3.15c}$$

As in the ΔM_{119} case, we find $\Delta M_{118} > 0$ due to the heavier isobar xenon, and the heavier isomeric state of iodine. Although the unknown ^{118}I mass appears in the correction term, an estimate of its value can be taken from the atomic mass table [Wa88] or the uncorrected value for $M(^{118}\mathrm{I})$ found in §3.6. This is justifiable because the uncertainty of the correction term is dominated by the C_Z coefficient uncertainties, i.e. ± 20%, whereas the mass uncertainties are of the order of 10^{-3}% or less. A schematic diagram labeling the various C_Z coefficients is presented in fig. 3.9.

From table 3.7 we find $\sum_Z C_Z^{118} = 63\ 351 \pm 367$. The coefficient for parent-daughter feeding from xenon is calculated in an entirely similar manner to the previous $A = 119$ case. The parent-daughter feeding result from the RATE3 calculation is $C_{Xe} = 1\ 224 \pm 20\%$.

The production of ^{118m}I leads to two contaminant coefficients; C_{m_I}, a parent-daughter component, and $C_{m_{I,\gamma}}$, a direct γ-ray component. Each is handled independently. The method of solution for the isomer feeding to the ground state iodine population is the same as the parent-daughter feeding described for $A = 119$. The parent-daughter feeding result from the RATE3 calculation yields $C_{m_I} = 1\ 652 \pm 20\%$. The direct feeding counts, $C_{m_{I,\gamma}}$, are given by $C_{m_{I,\gamma}} = C_{m_{I\,\text{parent decays}}} \times I_{\gamma,\text{absolute}} \times \mathcal{E}_{\text{detector}}$, where $C_{m_{I\,\text{parent decays}}}$ are the number of parent decays, $I_{\gamma,\text{absolute}}$ is the absolute branching ratio (or absolute intensity per 100 parent decays) for the 605 keV transition from ^{118m}I, and $\mathcal{E}_{\text{detector}}$ is the detector efficiency at 605 keV. The direct isomer γ-ray feeding coefficient is then $C_{m_{I,\gamma}} = 17\ 400 \pm 20\%$.

The grandparent-daughter feeding coefficient, C_{Cs}, due to cesium production is evaluated based on the background activity found in the $A = 118$ γ-ray sum spectra. (No cesium activity is found there.) The result from the RATE3 calculation is $C_{Cs} \leq 37 \pm 20\%$. This coefficient is not included in the contaminant correction ΔM_{118}.

The coefficients for the contaminant correction, equation (3.12), are summarized in table 3.8. A summary of the ΔM_{118} calculation is given in table 3.10. The ^{118}I mass correction, ΔM_{118}, is 96.7 ± 15.3 μu.

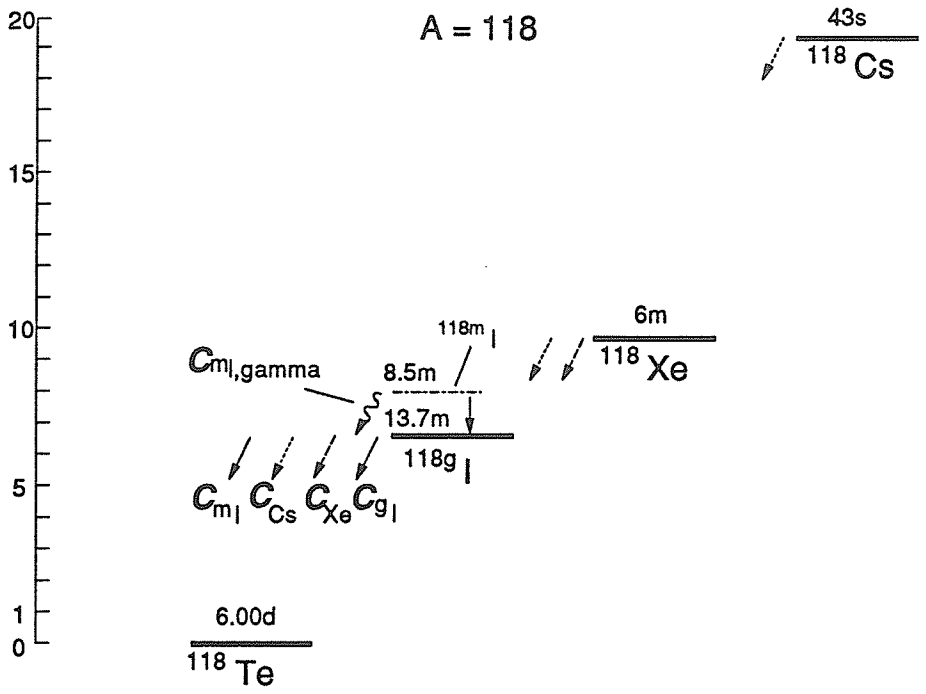

Fig. 3.9. Decay scheme and contaminants (bold italics) at mass number A = 118. The vertical scale is in units of MeV (^{118m}I is not drawn to scale). See § 3.7.1 for details.

Table 3.10. Corrections at mass number A = 118.

Reference masses			
$M(^{118}\mathrm{I})$	117 912 836 ± 159 μu		[this work. uncorrected]
$M(^{118}\mathrm{Xe})$	117 916 314 ± 305 μu		[Wa88]
$M(^{118}\mathrm{Cs})$	117 926 709 ± 140. μu		[Wa88]
Corrections			
Nuclide	Feeding to I (%)	Correction(μu)	Source
^{118}Cs	< 0.06	(< 7.896 ± 1.500)	^{118}Cs^{beam} β$^+$β$^+$
^{118}Xe	1.9	60.362 ± 13.792	^{118}Xe^{beam} β$^+$
^{118m}I	2.6	3.147 ± 0.629	^{118m}I^{beam} I.T.
^{118m}I	27.5	33.142 ± 6.638	γ(Te) from ^{118m}I^{beam} β$^+$
Total		ΔM_{118} = 96.651 ± 15.319	

Consider the contamination present in the ^{117}I mass spectra. The mass corresponding to the measured centroid is given by

$$M_{117} = \frac{C_{Xe}\, M(^{117}\mathrm{Xe}) + C_I\, M(^{117}\mathrm{I})}{\sum_Z C_Z} \quad , \tag{3.16}$$

where C_{Xe} is parent-daughter feeding $\mathrm{Xe}^{beam} \rightarrow \mathrm{I}$,

C_I is the main mass component I^{beam},

$\sum_Z C_Z$ = sum of the coefficients.

The weighted average formula is re-written to identify the mass contribution of ^{117}I and contaminants as

$$M_{117} = M(^{117}\mathrm{I}) + \Delta M_{117} \tag{3.17a}$$

where

$$\Delta M_{117} = \frac{C_{Xe}}{\sum_Z C_Z} [\, M(^{117}\mathrm{Xe}) - M(^{117}\mathrm{I}) \,] \tag{3.17b}$$

Again, we find $\Delta M_{117} > 0$ due to the heavier isobar xenon. The unknown ^{117}I mass appears in the correction term, and an estimate of its value can be taken from the atomic mass table [Wa88] or the uncorrected value for $M(^{117}\mathrm{I})$ found in §3.6. A schematic diagram labeling the C_Z coefficients is presented in fig. 3.10.

From table 3.7 we find $\sum_Z C_Z^{117} = 369\,931 \pm 841$. The coefficient for parent-daughter feeding from xenon is calculated in an entirely similar manner to the previous A = 119, 118 case. The parent-daughter feeding result from the RATE3 calculation is $C_{Xe} = 26\,703 \pm 20\%$.

The coefficients for the contaminant correction, equation (3.16), are summarized in table 3.8. A summary of the ΔM_{117} calculation is given in table 3.11. The ^{117}I mass correction, ΔM_{117}, is 446.5 ± 91.8 μu.

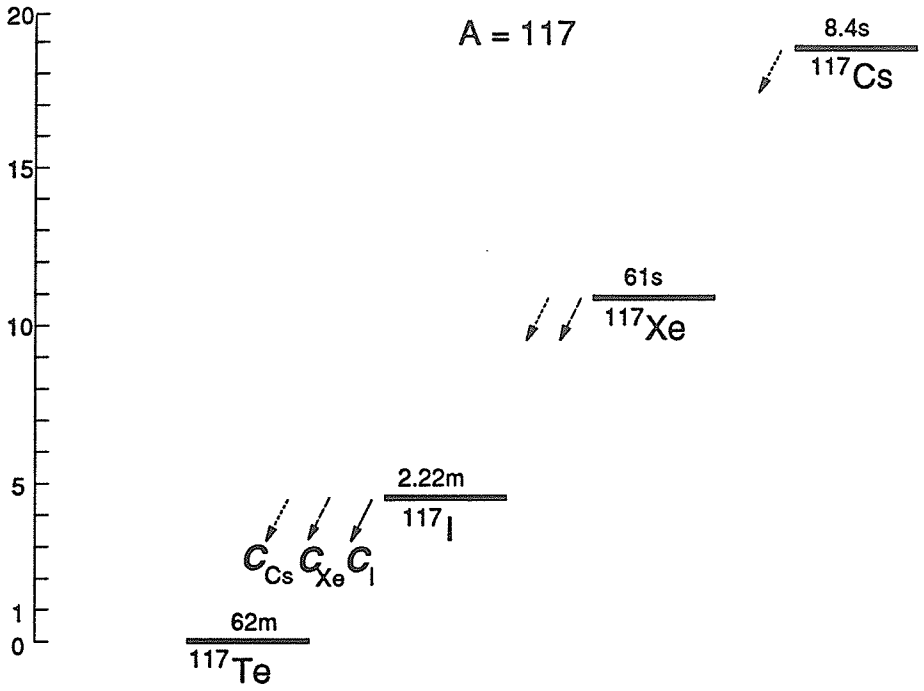

Figure 3.10. Decay scheme and contaminants (bold italics) at mass number A = 117. The vertical scale is in units of MeV. See §3.7.1 for details.

Table 3.11. Corrections at mass number A = 117.

Reference masses			
$M(^{117}\mathrm{I})$	116 913 808	± 152 μu	[this work. uncorrected]
$M(^{117}\mathrm{Xe})$	116 920 340	± 238 μu	[Wa88]
$M(^{117}\mathrm{Cs})$	116 928 865	± 189 μu	[Wa88]

Corrections			
Nuclide	Feeding to I (%)	Correction(μu)	Source
^{117}Cs	< 3.0	(< 442.280 ± 88.745)	$Cs^{beam} \rightarrow Xe \rightarrow I$
^{117}Xe	7.2	446.498 ± 91.820	$Xe^{beam} \rightarrow I$
Total		$\Delta M_{117} = 446.498 \pm 91.820$	

Finally, we summarize the mass corrections due to contaminant feeding in the table below.

Table 3.12. Corrections to measured iodine masses due to contaminants.

Mass number	Correction	
119	$\Delta M_{119} = 330 \pm 67$ μu	$\frac{\Delta M_{119}}{M(^{119}\mathrm{I})} = 3$ ppm
118	$\Delta M_{118} = 97 \pm 15$ μu	$\frac{\Delta M_{118}}{M(^{118}\mathrm{I})} = 0.8$ ppm
117	$\Delta M_{117} = 446 \pm 92$ μu	$\frac{\Delta M_{117}}{M(^{117}\mathrm{I})} = 4$ ppm

3.8 Corrected masses

To find the corrected masses of ^{118}I and ^{117}I, we begin by expanding the measured masses (cf §3.6). That is,

$$\begin{aligned} M_{119} &= M(^{119}\mathrm{I}) - M(e^-) + \Delta M_{119} \quad , \\ M_{118} &= M(^{118}\mathrm{I}) - M(e^-) + \Delta M_{118} \quad , \\ M_{117} &= M(^{117}\mathrm{I}) - M(e^-) + \Delta M_{117} \quad . \end{aligned} \tag{3.18}$$

Accordingly, we may write Bleakney's Theorem, including contaminants, as

$$\begin{aligned} &[\, M(^{118}\mathrm{I}) - M(e^-) + \Delta M_{118} \,]\, V_{118} = [\, M(^{119}\mathrm{I}) - M(e^-) + \Delta M_{119} \,]\, V_{119} \\ &M(^{118}\mathrm{I}) = M(^{119}\mathrm{I}) \left(\frac{V_{119}}{V_{118}} \right) + M(e^-) \left(1 - \frac{V_{119}}{V_{118}} \right) + \Delta M_{119} \left(\frac{V_{119}}{V_{118}} \right) - \Delta M_{118} \quad , \end{aligned} \tag{3.19}$$

and

$$\begin{aligned} &[\, M(^{117}\mathrm{I}) - M(e^-) + \Delta M_{117} \,]\, V_{117} = [\, M(^{119}\mathrm{I}) - M(e^-) + \Delta M_{119} \,]\, V_{119} \\ &M(^{117}\mathrm{I}) = M(^{119}\mathrm{I}) \left(\frac{V_{119}}{V_{117}} \right) + M(e^-) \left(1 - \frac{V_{119}}{V_{117}} \right) + \Delta M_{119} \left(\frac{V_{119}}{V_{117}} \right) - \Delta M_{117} \quad . \end{aligned} \tag{3.20}$$

Using the ΔM corrections from § 3.7.2 in these equations, we finally determine the corrected masses of ^{118}I and ^{117}I to be

$$M(^{118}\mathrm{I}) = 117\,913\,067 \quad \pm \quad 173 \quad \mu\mathrm{u} \quad , \tag{3.21a}$$

and

$$M(^{117}\mathrm{I}) = 116\,913\,686 \quad \pm \quad 189 \quad \mu\mathrm{u} \quad . \tag{3.21b}$$

The errors are obtained by adding, in quadrature, the error of terms on the right hand side of the equations (3.19) and (3.20). Summaries of the calculation for $M(^{118}\mathrm{I})$ and $M(^{117}\mathrm{I})$ are presented in tables 3.13 and 3.14.

Table 3.13. Calculation of the mass of ^{118}I.

Measured Mass Ratio	$\left(\frac{\nu_{119}}{\nu_{118}}\right)$	0.991 613 61 ± 0.000 001 02	
Corrections			
Nuclide		Correction (μu)	Source
^{119}Xe		327.2 ± 66.7	^{119}Xe β$^+$
^{118}Xe		-60.4 ± 13.8	^{118}Xe β$^+$
^{118m}I		-3.1 ± 0.6	^{118m}I I.T.
^{118m}I		-33.1 ± 6.6	γ(Te) from ^{118m}I β$^+$
Total	$\Delta M_{119}\left(\frac{\nu_{119}}{\nu_{118}}\right) - \Delta M_{118}$	230.6 ± 68.4	
Uncorrected mass	$M(^{118}\mathrm{I})_{\text{uncorrected}}$	117 912 836 ± 159 μu	
Corrected mass	$M(^{118}\mathrm{I})$	117 913 067 ± 173 μu	
Corrected mass ratio	$\frac{M(^{118}\mathrm{I})}{M(^{119}\mathrm{I})}$	0.991 615 60 ± 0.000 001 18	

Table 3.14. Calculation of the mass of ^{117}I.

Measured mass ratio	$\left(\frac{V_{119}}{V_{117}}\right)$	0.983 212 03 ± 0.000 000 94	
Corrections			
Nuclide		Correction (μu)	Source
^{119}Xe		324.5 ± 65.9	^{119}Xe β$^+$
^{117}Xe		-446.5 ± 91.8	^{117}Xe β$^+$
Total	$\Delta M_{119}\left(\frac{V_{119}}{V_{117}}\right) - \Delta M_{117}$	-122.0 ± 113.0	
Uncorrected mass	$M(^{117}\text{I})_{\text{uncorrected}}$	116 913 808 ± 152 μu	
Corrected mass	$M(^{117}\text{I})$	116 913 686 ± 189 μu	
Corrected mass ratio	$\frac{M(^{117}\text{I})}{M(^{119}\text{I})}$	0.983 211 08 ± 0.000 001 34	

3.9 Corrected mass and voltage ratios

We present the mass ratios of the iodine isotopes in addition to their directly determined mass values of the previous section. The mass ratios reflect the primary experimental result. That is, we measure the applied potentials for two different mass species that follow the same path through the isotope separator. The ratio of the potentials is equivalent to the mass ratio via Bleakney's Theorem. We may write directly the uncorrected mass ratios of the iodine isotopes in terms of the measured voltage ratios (refer equation (3.7)).

$$\frac{M(^{118}\mathrm{I})_{\mathrm{uncorrected}}}{M(^{119}\mathrm{I})_{\mathrm{uncorrected}}} = \left(\frac{V_{119}}{V_{118}}\right) + \frac{M(e^-)}{M(^{119}\mathrm{I})}\left(1-\frac{V_{119}}{V_{118}}\right) \qquad (3.22a)$$

$$= 0.991\,613\,65 \pm 0.000\,001\,02 \ ,$$

and

$$\frac{M(^{117}\mathrm{I})_{\mathrm{uncorrected}}}{M(^{119}\mathrm{I})_{\mathrm{uncorrected}}} = \left(\frac{V_{119}}{V_{117}}\right) + \frac{M(e^-)}{M(^{119}\mathrm{I})}\left(1-\frac{V_{119}}{V_{117}}\right) \qquad (3.22b)$$

$$= 0.983\,212\,11 \pm 0.000\,000\,94 \ .$$

We know that the separator beam is contaminated. Consequently, the measured voltage ratios reflect contaminated mass spectra. The mass ratios of the iodine isotopes, corrected for contamination, are then

$$\frac{M(^{118}\mathrm{I})}{M(^{119}\mathrm{I})} = \left(\frac{V_{119}}{V_{118}}\right)+\frac{M(e^-)}{M(^{119}\mathrm{I})}\left(1-\frac{V_{119}}{V_{118}}\right)+\frac{\Delta M_{119}}{M(^{119}\mathrm{I})}\left(\frac{V_{119}}{V_{118}}\right)-\frac{\Delta M_{118}}{M(^{119}\mathrm{I})} \qquad (3.23a)$$

$$= 0.991\,615\,60 \pm 0.000\,001\,18 \ ,$$

and

$$\frac{M(^{117}\mathrm{I})}{M(^{119}\mathrm{I})} = \left(\frac{V_{119}}{V_{117}}\right)+\frac{M(e^-)}{M(^{119}\mathrm{I})}\left(1-\frac{V_{119}}{V_{117}}\right)+\frac{\Delta M_{119}}{M(^{119}\mathrm{I})}\left(\frac{V_{119}}{V_{117}}\right)-\frac{\Delta M_{117}}{M(^{119}\mathrm{I})} \qquad (3.23b)$$

$$= 0.983\,211\,08 \pm 0.000\,001\,34 \ .$$

3.10 ^{118m}I Isomeric transition

The existence of an isomeric state in ^{118}I was first reported by Laudenbaur-Bellis and Bakhru [La68]. Their experiment used the reaction $^{12}C(^{nat.}Ag,xn)^{118}I$ to create the iodine activity. The reaction products were deposited on an Al catcher foil from which the iodine was chemically separated. They observed, in a singles γ-ray spectrum, a photo-peak at 104 ± 2 keV with an associated half-life of about 8 minutes. This photo-peak was assigned to the isomeric transition (I.T.) $^{118m}I \rightarrow {}^{118g}I + \gamma$. There have been no reports on the 104 keV isomer transition since [La68].

We did not observe a photo-peak at 104 keV in our γ-ray spectrum, but instead found an unaccounted peak at 114 keV. We generated a mass spectrum based on this unidentified activity. Based on this analysis, the corresponding mass of the γ-ray source is found to be $117\ 913\ 441 \pm 356$ μu which corresponds to a mass close to that of ^{118}I. Since no beta-active isotope or isomeric state is known to emit a γ-ray at this energy, the 114 keV γ-ray may be ascribed to the ^{118m}I isomeric transition to the ground state.

3.10.1 Analysis

3.10.1.1 γ-ray analysis

The γ-ray spectrum in the region of 104 keV is presented in fig. 3.11. The expected 104 keV photo-peak is not observed above the background level of 16 000 counts. The nearby small peak at 100 keV is from room background. To the right of 104 keV, we see two sizeable peaks. The first at channel 113.468 ± 0.015, is the ^{118m}I candidate, while the other at channel 118 is due to ^{118}Xe activity. The number of counts in the ^{118m}I candidate peak is 10330 ± 547 (refer table 3.7). This yields a relative branching ratio $I_{\gamma,rel.} = 4.0 \pm 0.6$ % as compared to the 605 keV transition ($I_{\gamma=605keV,rel.} = 100\%$). Using the energy calibration outlined in Appendix B, we assign an energy of 114.24 ± 0.72 keV to this peak.

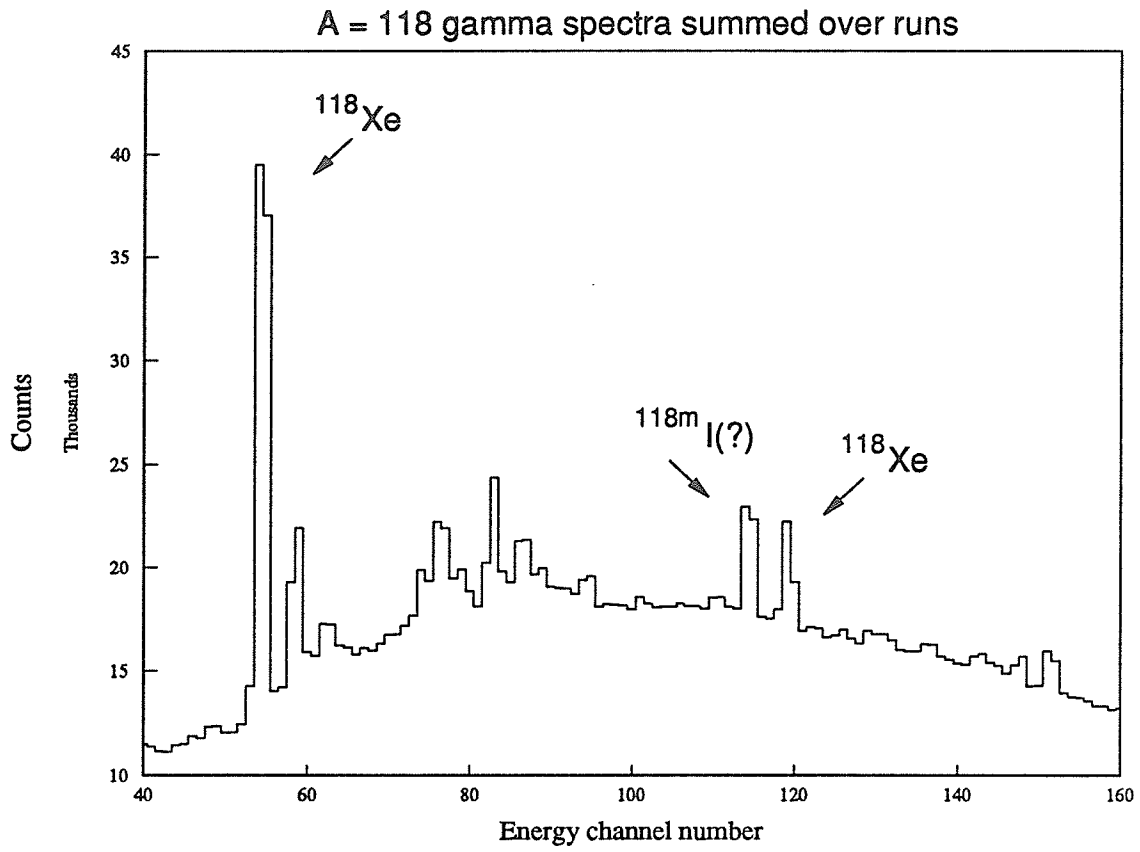

Figure 3.11. Sum γ-ray spectra for mass number A = 118. The peak at channel 100 is from room background. The peak at channel 114 is the candidate ^{118m}I I.T. peak. The peak at channel 118 is from ^{118}Xe.

3.10.1.2 Mass analysis

The high resolution of the Chalk River Isotope Separator gives us a unique tool to determine the mass of a γ-ray emitting nuclide present in the separator beam. The mass precision obtainable using our mass spectrometric technique is on the order of 100 keV. Since neighboring A = 118 isobars are separated in mass by approximately 5000 keV, we may unambiguously identify any isotope emitting a γ-ray.

The procedure for the mass spectrometric determination of the 114 keV photopeak at mass number 118 is identical to the mass analysis for the triplet ^{119}I, ^{118}I, ^{117}I. The only change is that we substitute a 114 keV γ-ray in place of the 605 keV γ-ray selected previously for ^{118}I. The selected energies and mass spectra for ^{119}I and ^{117}I remain unchanged from the §3.3. (Note that it is not necessary to include the mass analysis for ^{117}I. The unknown mass at A = 118 may be determined with respect to the known mass of ^{119}I alone.) The selected γ-ray energies used to generate the individual mass spectra are given in table 3.15.

Table 3.15. Selected γ(Te) from I β$^+$,EC decays for ^{119}I, and ^{117}I and the unknown A = 118 γ-ray transition. (T.W. = this work)

Isotope	γEnergy (keV)	I_γ (relative intensity,%)	Reference
^{119}I	257.5	100	[NN92]
^{118}(?)	114.2	4	T.W.
^{117}I	325.9	100	[B187]
	274.4	27	[B187]

A sample of the mass spectra (run 6) generated from the energies above is presented in fig. 3.12.

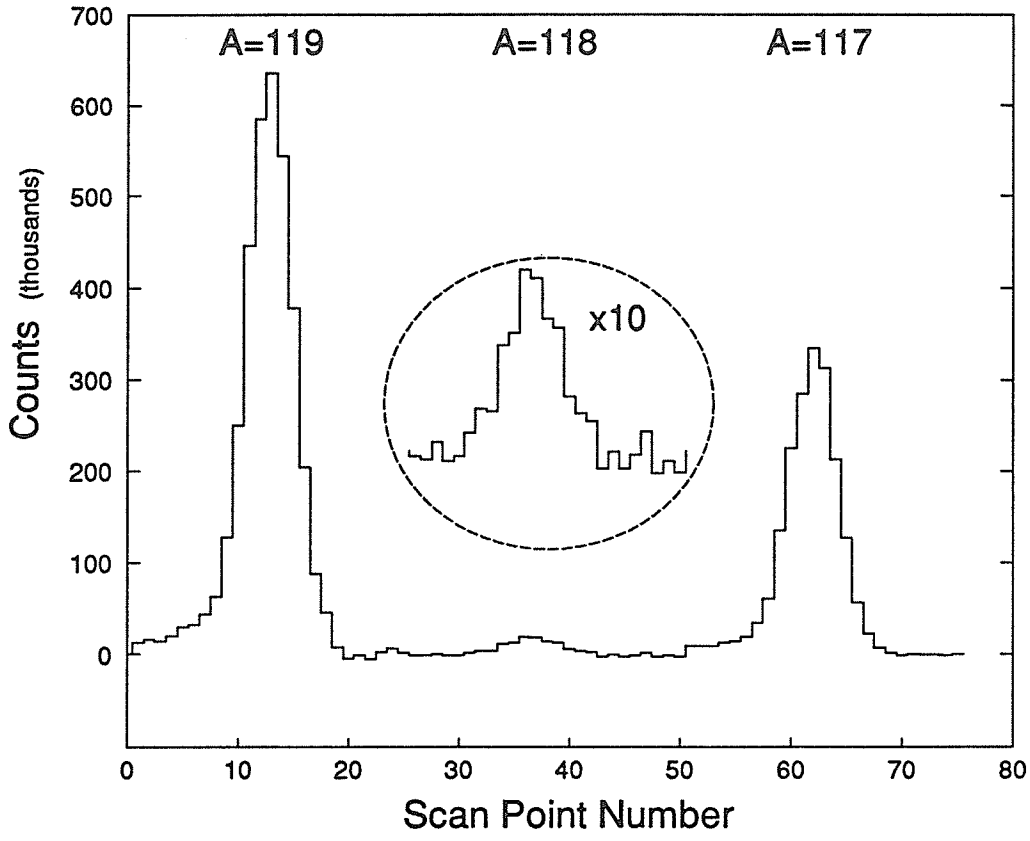

Fig. 3.12. Mass spectrum used to assign the unidentified 114 keV photopeak in the A = 118 γ-ray spectra. The mass peaks at A = 119 and 117 are generated by selecting the same iodine decay energies of §3.3.

The voltage centroids of the mass peaks generated are given in table 3.17. The centroid positions for mass numbers 119 and 117 are unchanged from table 3.4. The voltage ratios follow in table 3.16.

Table 3.16. Mass Centroids from Sum Mass Spectra (output of program MASSDIF)

Run	Mass Number	Centroid (volts)	Statistical Uncertainty	Voltage Uncertainty	Overall Uncertainty
3	119	39780.500	0.036	0.080	0.087
	118	40116.723	0.353	0.171	0.392
	117	40459.785	0.016	0.077	0.079
5	119	39779.883	0.021	0.077	0.080
	118	40116.711	0.176	0.131	0.215
	117	40459.207	0.012	0.082	0.083
6	119	39780.238	0.019	0.080	0.082
	118	40116.449	0.193	0.471	0.509
	117	40459.414	0.012	0.080	0.081
8	119	39779.930	0.022	0.077	0.080
	118	40116.383	0.245	0.188	0.309
	117	40459.137	0.013	0.076	0.077
9	119	39780.227	0.020	0.077	0.080
	118	40116.430	0.190	0.241	0.307
	117	40459.359	0.013	0.081	0.082
10	119	39780.227	0.026	0.080	0.084
	118	40116.258	0.192	0.171	0.257
	117	40459.594	0.013	0.076	0.077
13	119	39779.418	0.030	0.082	0.087
	118	40115.324	0.303	0.145	0.336
	117	40458.512	0.017	0.078	0.080
17.1	119	39780.465	0.030	0.079	0.085
	118	40116.063	0.306	0.257	0.400
	117	40459.738	0.016	0.072	0.074
17.2	119	39780.605	0.028	0.080	0.085
	118	40115.988	0.328	0.458	0.563
	117	40459.824	0.016	0.072	0.074

Table 3.17. Voltage ratios calculated from centroid data of table 3.16.

Run	$\frac{V_{119}}{V_{118}}$	Uncertainty	
3	0.991 618 9	0.000 009 9	
5	0.991 603 8	0.000 005 8	
6	0.991 619 1	0.000 012 8	
8	0.991 613 1	0.000 007 9	
9	0.991 619 3	0.000 007 8	
10	0.991 623 6	0.000 006 7	
13	0.991 601 8	0.000 008 6	
17.1	0.991 634 3	0.000 010 1	
17.2	0.991 639 7	0.000 014 1	
	0.991 615 7	0.000 002 8	⇐weighted mean, $\chi^2_{reduced}$= 1.9

To calculate the mass of the unknown species at A = 118, we again use Bleakney's Theorem given by equation (3.19)

$$M_{118} = M(^{119}\mathrm{I})\left(\frac{V_{119}}{V_{118}}\right) + M(e^-)\left(1 - \frac{V_{119}}{V_{118}}\right) + \Delta M_{119}\left(\frac{V_{119}}{V_{118}}\right) \quad , \tag{3.24}$$

where the ΔM_{119} correction is taken from table 3.12. (Note: no contaminant feeding correction at A = 118 has been included.) The mass of the unknown nuclide at A = 118, based on the 114 keV activity, is 117 913 445 ± 356 μu. This mass value is consistent with the mass of ^{118}I alone, as suggested by fig. 3.13.

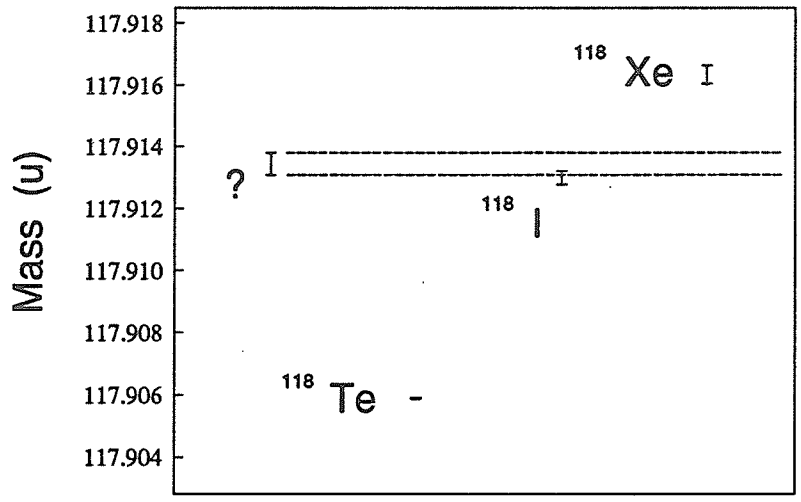

Fig. 3.13. The mass of the unknown species ("?") associated with the 114 keV γ-ray activity in the A = 118 γ-ray spectra. The masses of tellurium, iodine, and xenon are plotted to show that the mass of the unknown species is consistent only with the mass of iodine.

3.10.2 Summary

The data presented here represent the latest information available for the isomer transition in ^{118}I. The mass-spectrometric analysis is not sufficient to unambiguously prove the 114 keV γ-ray is the isomer transition in ^{118}I. There are, however, some observations that can be made.

No photopeak is observed at the previously reported energy, 104 ± 2 keV, for the isomer transition. Nevertheless, a new photopeak originating from ^{118}I at 114.24 ± 0.72 keV is observed. A half-life measurement is needed to gather a stronger body of evidence for the case that the 114 keV γ-ray is the isomer transition. As well, a conversion-electron spectroscopy experiment would make it possible to establish the electromagnetic character of the transition in the decay of ^{118m}I and support spin and parity assignments of the isomer and ground states.

4 Conclusion

The mass ratios summarized in table 4.1 have been combined with the known mass of ^{119}I to yield values for the atomic masses of ^{117}I and ^{118}I. The masses of ^{117}I and ^{118}I have been determined from the weighted average of nine independent measurements of the $\frac{^{117}\text{I}}{^{119}\text{I}}$ and $\frac{^{118}\text{I}}{^{119}\text{I}}$ mass ratios. The mass ratios have been corrected for contamination from Xe and ^{118m}I decays as required. The mass value for ^{117}I is in good agreement (0.5 σ) with the value predicted by Wapstra et al., which is based only on systematics [Wa88]. The mass value for ^{118}I is in excellent agreement (0.3 σ) with the value predicted by Wapstra.

Table 4.1. Summary of experimental mass results.

Measured Iodine Mass Ratios (corrected)			
$\frac{M(^{117}\text{I})}{M(^{119}\text{I})}$ = 0.983 211 1 (13)			
$\frac{M(^{118}\text{I})}{M(^{119}\text{I})}$ = 0.991 615 6 (12)			
Measured Iodine Masses (corrected)		**Predicted Iodine Masses**	**Reference**
$M(^{117}\text{I})$ = 116.913 69 (19) u		116.913 47 (40) u	[Wa88]
$M(^{118}\text{I})$ = 117.913 07 (17) u		117.912 99 (22) u	[Wa88]
Auxiliary Data			
$M(^{119}\text{I})$ = 118.910 06 (10) u			[Wa88]

The mass ratio uncertainties quoted here are at the 1 ppm level. This represents a higher level of precision than that of the deduced masses, $M(^{118}\text{I})$ and $M(^{117}\text{I})$, using the reference mass $M(^{119}\text{I})$. The reference mass is, to date, also determined to the 1 ppm level. The error, then, in $M(^{118}\text{I})$ and $M(^{117}\text{I})$ is approximately $\approx \sqrt{2} \times 1$ ppm. If in the

future, the mass of $M(^{119}\mathrm{I})$ is re-determined to a higher level of precision (i.e. << 1 ppm), then the precision of $M(^{118}\mathrm{I})$ and $M(^{117}\mathrm{I})$ will be limited only by our measured mass ratio as calculated by Blekney's Theorem.

The masses measured in this work are compared in fig. 4.1 with the values presented in the 1986-1987 Atomic Mass Predictions [Ha88], which are the results of nine different mass models fitted to the 1986 midstream atomic mass evaluation [Wa88]. Recent measurements with the Chalk River ISOL of other neutron deficient nuclei close to ^{100}Sn are also compared in the figure.

The nine mass models may be described briefly. They fall into one of several major classes of models; semi-empirical or phenomenological models, liquid drop or droplet models, mass models based on the shell model, and mass models based on mass relations.

Starting in the order of appearance in fig. 4.1, the macroscopic-microscopic model of P. Möller and J.R. Nix determines the potential energy (or mass) of a nucleus as a sum of a macroscopic energy term and a microscopic energy term, both calculated as a function of shape, Z, and N. A Yukawa-plus-exponential model is used for the macroscopic term and a folded-Yukawa single-particle potential as a starting point for the microscopic term. Another macroscopic-microscopic model by P. Möller et al. uses a finite-range droplet model for the macroscopic term plus a folded-Yukawa single-particle potential for the microscopic term.

The model of T. Tachibana et al. is an empirical atomic mass formula with shell corrections. It consists of three terms. The first "gross" term is a smooth function of Z and N representing the gross features of the nuclear mass surface. The second term includes the average behavior of even-odd neutron-proton energies, and the third term consists of empirical proton and neutron shell energies.

The model of L. Spanier and S. A. E. Johansson is a liquid-drop-type mass formula with deformation and shell corrections. The liquid drop is used as an analogy to the nucleus since the binding energy per nucleon and the density of nuclear matter are almost independent of A. This resembles liquid droplets, in that the heat of vaporization and the density of the liquid are independent of the size of the droplet. The droplet analogy leads to features of the mass formula related to nuclear structure such as volume and surface energies, for example.

L. Satpathy and R. C. Nayak present the masses of atomic nuclei in the infinite nuclear matter (INM) model. In the INM model, the ground state energy of a nucleus is equivalent to the energy of a perfect sphere made up of infinite nuclear matter plus residual characteristic energy, η, due to shell effects, deformations, etc.. The INM model is incorporated into their earlier work on a mass model based on mass relations. The previous mass relation becomes a mass formula when a recursion relation for η is obtained. Thus, long-range mass predictions are possible with the global property of the INM sphere together with the local energy η.

The Modified Ensemble Model of E. Comay, et al., the Garvey-Kelson Mass Relations Model by J. Jänenke and P. J. Masson, and the Inhomogeneous Partial Difference Equation with High-Order Isospin Contributions Model by P. J. Masson and J. Jänecke are all related to mass models based on Garvey-Kelson mass relations. This class of model is based on a Hartree-Fock or Nilsson-like single-particle picture of the nucleus. In the simplest case, a homogeneous partial difference equation in N and Z involving a few neighboring nuclei is written. The mass of all but one would have been experimentally determined. The remaining unknown mass is determined algebraically.

The model of G. Dussel, E. Caurier, and A.P. Zuker is based on α-line systematics. A plot of α separation energies along lines of constant isospin (*N-Z*) is used to predict new masses by performing a polynomial interpolation between gaps in the known masses.

The measured masses agree with most of the mass prediction models. In the case of ^{117}I there is a exception for the model of Satpathy and Nayak. Their Infinite Nuclear Matter Model is 4.1σ from our experimental work or using their stated uncertainty we are 1.8σ from their prediction. In the case of ^{118}I there are two models in poor agreement with our result. One of these is the model of Satpathy and Nayak. Our ^{118}I mass result is 4.2σ from their predicted value or 1.7σ from their prediction. Additionally, for the nuclei we have presented in fig. 4.1, the INM model is seen to under-estimate the nuclear binding energy before the $Z = 50$ proton shell closure and over-estimate the binding energy after closure. The second model that does not agree with our ^{118}I mass result is that of Dussel, Caurier, and Zuker. Their mass prediction based on α-line systematics is 3.1σ from our result or 3.0σ from their prediction using their stated uncertainty.

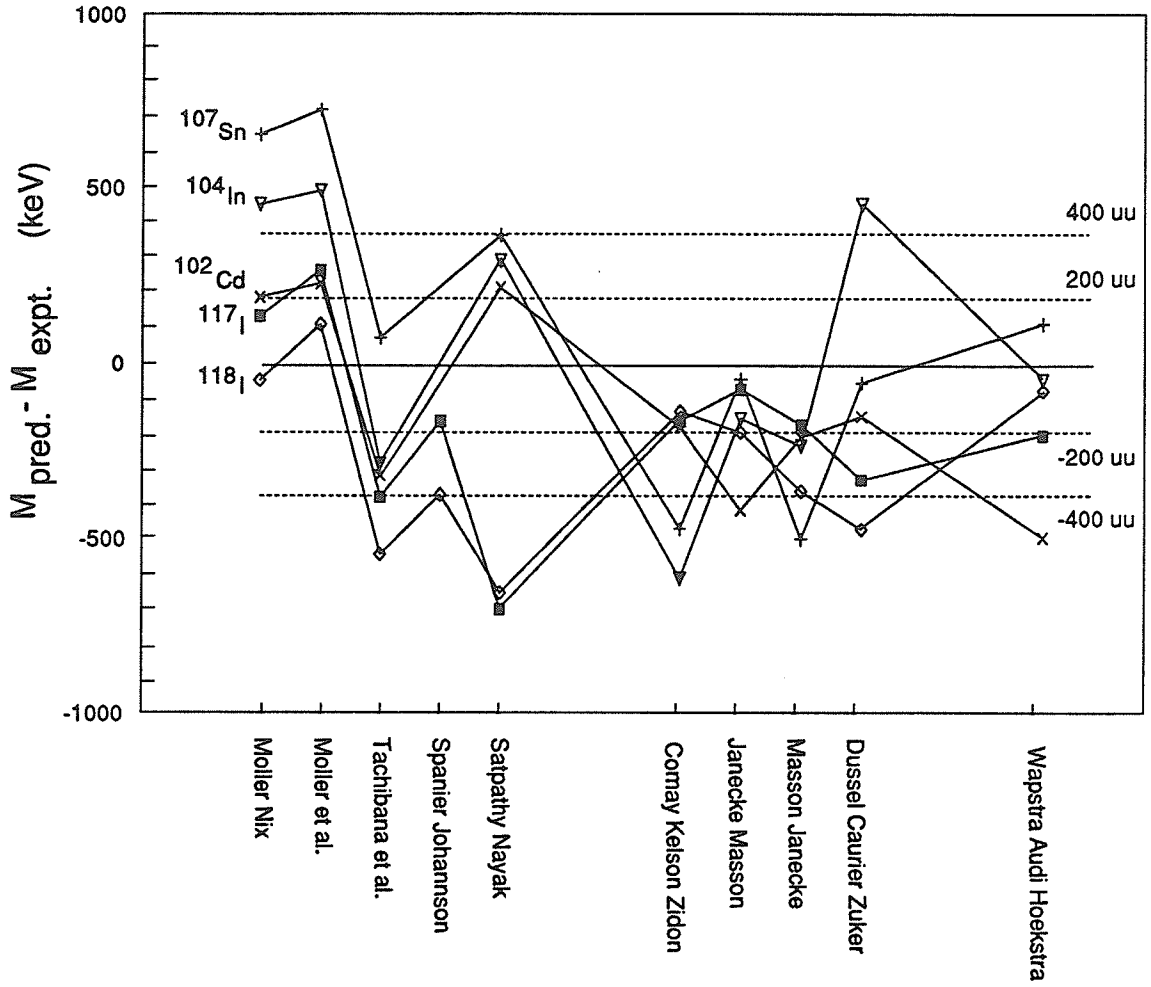

Fig. 4.1. Differences between measured masses and masses from the 1986-1987 Atomic Mass Predictions [Ha88] and the 1986 midstream mass evaluation [Wa88]. The predictions for a given nuclide are joined together with a line for easier examination. The mass predictions are grossly grouped according to the model from which they are based. The first group includes Unified Microscopic-Macroscopic Models, Semi-Emperical Model, Droplet Model, and a Infinite Nuclear Matter Model. The second group is based on mass relations and systematics. Our experimental iodine results are in agreement with all models except for Satpathy and Nayak (INM Model)(see text).

The measured masses in this work are included in a plot of S_{2n} values for nuclei in the region of ^{100}Sn, shown in fig. 4.2. The observed break in the iodine slope at N=65, 66 is the result of a slightly heavier measured mass of ^{117}I than the predicted mass of Wapstra et al.. Interestingly, a shape deformation maxima near the middle of the iodine neutron shell near $N = 66$ (i.e.^{119}I) is predicted [He83]. The deformation should decrease as N approaches the closed shell at $N = 50$. A broad hump in the S_{2n} curve would be evidence of a deformation. However, the error bars provided in the figure show that we can not discriminate this predicted feature.

Finally, the ^{118m}I isomeric transition at 104(2) keV is not observed in the collected γ-ray spectra. However a transition at 114.24(72) keV is mass spectrometrically identified to have originated from ^{118}I activity. We suggest that the transition at 114 keV is the isomer transition and the original assignment of the 104 keV γ-ray to this transition is in error.

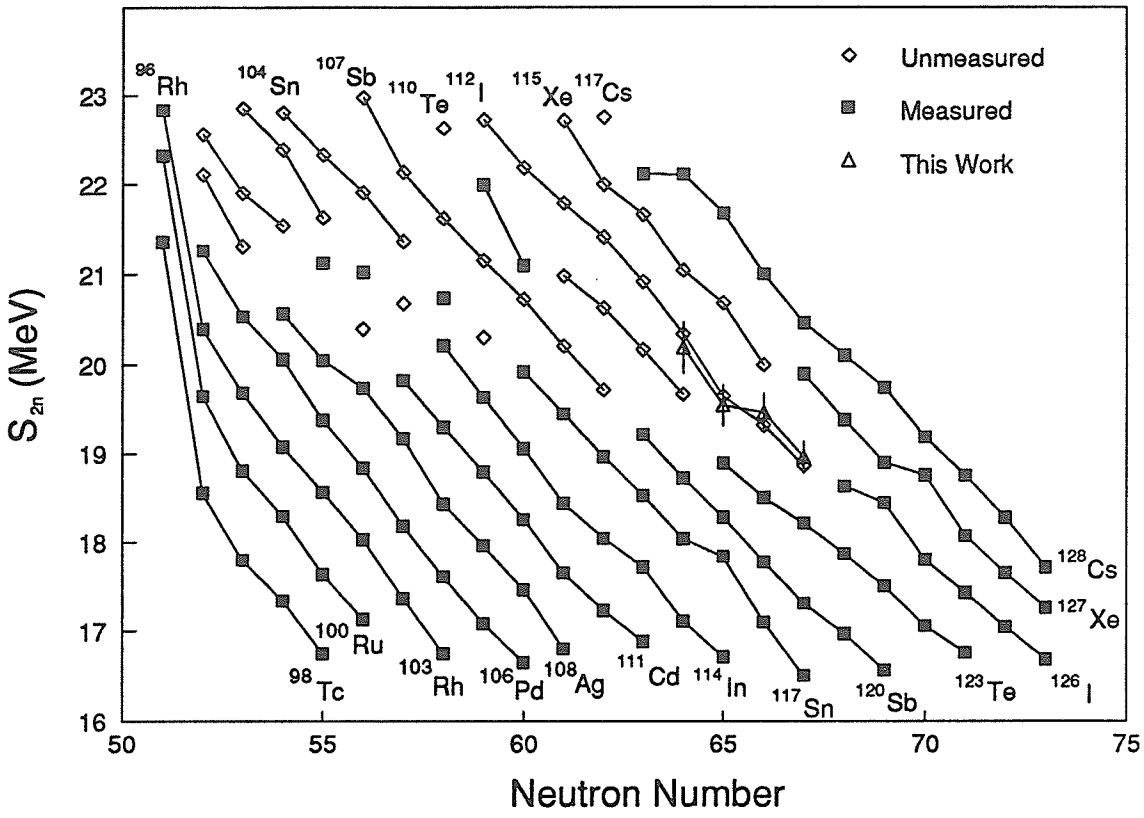

Fig. 4.2. Separation energies (in MeV) of two neutrons, $S_{2n} = -M(A, Z) + M(A - 2, Z) + 2n$, plotted as a function of N in the region of ^{100}Sn. Isotopes of an element are connected by a line. Error bars have been provided for the iodine masses measured in this work. They are based on our experimental uncertainty alone. Other error bars have been omitted for clarity.

Appendix A.

Radioisotope production by beam deposition and radioactive decay

Consider a beam of atoms comprised of three radioactive species. The three species are related to each other in that species 1 decays into species 2, species 2 decays into species 3, and species 3 decays. (Experimentally, Cs $\rightarrow$ Xe $\rightarrow$ I $\rightarrow$.)

Beginning at time $t=t_0$, the beam deposits a sample for a fixed time interval, $t_{\text{COLLECT}} = t_1 - t_0$. We may write the differential equations that describe the rate of accumulating each radioisotope in the sample as follows:

$$\frac{dN_1(t)}{dt} = P_1 - \lambda_1 N_1(t) \qquad ,0 < t < t_1, \tag{1a}$$

$$\frac{dN_2(t)}{dt} = P_2 + \lambda_1 N_1(t) - \lambda_2 N_2(t) \qquad ,0 < t < t_1, \tag{1b}$$

$$\frac{dN_3(t)}{dt} = P_3 + \lambda_2 N_2(t) - \lambda_3 N_3(t) \qquad ,0 < t < t_1, \tag{1c}$$

where P_1, P_2, P_3 are the constant production rates of substances 1, 2, 3

$\lambda_1, \lambda_2, \lambda_3$ are the decay constants for substances 1, 2, 3, and

$N_1(t), N_2(t), N_3(t)$ are the number of atoms of substances 1, 2, 3 at time t.

The solutions $N_i(t), 0 < t < t_1$ for the initial condition $N_i(0) = 0$ are

$$N_1(t < t_1) = \frac{P_1}{\lambda_1}\left(1 - e^{-\lambda_1 t}\right) \quad , \tag{2a}$$

$$N_2(t < t_1) = \frac{(P_1 + P_2)}{\lambda_2}\left(1 - e^{-\lambda_2 t}\right) + \frac{P_1}{(\lambda_2 - \lambda_1)}\left(e^{-\lambda_2 t} - e^{-\lambda_1 t}\right) \quad , \tag{2b}$$

$$N_3(t < t_1) = \frac{(P_1 + P_2 + P_3)}{\lambda_3}\left(1 - e^{-\lambda_3 t}\right) + \frac{\lambda_2 P_1}{(\lambda_2 - \lambda_1)(\lambda_3 - \lambda_1)}\left(e^{-\lambda_3 t} - e^{-\lambda_1 t}\right)$$
$$+\left(P_2 - \frac{\lambda_1 P_1}{(\lambda_1 - \lambda_2)}\right)\frac{(e^{-\lambda_3 t} - e^{-\lambda_2 t})}{(\lambda_3 - \lambda_2)} \quad . \tag{2c}$$

The experimental situation changes at time, $t = t_1$, when the beam production ceases. The only change to equations (1) is that $P_1 = P_2 = P_3 = 0$. The differential equations become, simply

$$\frac{dN_1(t)}{dt} = -\lambda_1 N_1(t) \qquad , t_1 < t, \tag{3a}$$

$$\frac{dN_2(t)}{dt} = \lambda_1 N_1(t) - \lambda_2 N_2(t) \qquad , t_1 < t, \tag{3b}$$

$$\frac{dN_3(t)}{dt} = \lambda_2 N_2(t) - \lambda_3 N_3(t) \qquad , t_1 < t. \tag{3c}$$

We solve these differential equations using the boundary condition that solutions $N(t > t_1) = N(t < t_1)$ at $t = t_1$. The solutions have the form

$$N_1(t > t_1) = N_1(t_1)e^{-\lambda_1(t-t_1)} \quad , \tag{4a}$$

$$N_2(t > t_1) = N_2(t_1)e^{-\lambda_2(t-t_1)} + \frac{\lambda_1}{(\lambda_2 - \lambda_1)} N_1(t_1)\left(e^{-\lambda_1(t-t_1)} - e^{-\lambda_2(t-t_1)}\right) \quad , \tag{4b}$$

$$N_3(t > t_1) = N_3(t_1)e^{-\lambda_3(t-t_1)} + \frac{\lambda_2}{(\lambda_3 - \lambda_2)} N_2(t_1)\left(e^{-\lambda_2(t-t_1)} - e^{-\lambda_3(t-t_1)}\right)$$

$$+ \frac{\lambda_2\lambda_1}{(\lambda_2 - \lambda_1)} N_1(t_1)\left(\frac{e^{-\lambda_1(t-t_1)}}{(\lambda_3 - \lambda_1)} - \frac{e^{-\lambda_2(t-t_1)}}{(\lambda_3 - \lambda_2)} + \frac{(\lambda_2 - \lambda_1)e^{-\lambda_3(t-t_1)}}{(\lambda_3 - \lambda_1)(\lambda_3 - \lambda_2)}\right) \quad . \tag{4c}$$

A1. Number of observed decays

We may find the number of decays, Δ, in a time interval $t_{COUNT} = t_3 - t_2$, by integrating the activity, $\mathcal{A}$, of the radioactive source over the time interval. That is

$$\Delta = \int_{t_2}^{t_3} \mathcal{A}(t)dt \qquad , \mathcal{A}(t) = \lambda N(t),$$

$$= \int_{t_2}^{t_3} \lambda N(t)dt$$

Notice however, that this integrand is part of our starting differential equations (3)

e.g. (3a) $$\frac{dN_1(t)}{dt} = -\lambda_1 N_1(t) \quad , t_1 < t \quad .$$

Integrating both side with respect to dt we get

$$\int_{t_2}^{t_3} \left(\frac{dN_1(t)}{dt} \right) dt = -\int_{t_2}^{t_3} \lambda_1 N_1(t) dt \quad .$$

On the left hand side we have

$$\int_{t_2}^{t_3} \left(\frac{dN_1(t)}{dt} \right) dt = N_1(t_3) - N_1(t_2) \quad .$$

On the right hand side we have

$$-\int_{t_2}^{t_3} \lambda_1 N_1(t) dt = -\Delta_1 \quad ,$$

$$\therefore N_1(t_2) - N_1(t_3) = \Delta_1 \quad . \tag{5a}$$

We may also integrate the rate equation for substance 2 with respect to time,

$$\int_{t_2}^{t_3} \left(\frac{dN_2(t)}{dt} \right) dt = -\int_{t_2}^{t_3} (\lambda_1 N_1(t) - \lambda_2 N_2(t)) dt \quad ,$$

to get

$$N_2(t_2) - N_2(t_3) = \Delta_2 - \Delta_1 \quad . \tag{5b}$$

Similarly for the rate equation for substance 3,

$$N_3(t_2) - N_3(t_3) = \Delta_3 - \Delta_2 \quad . \tag{5c}$$

These last three equations can be used to generate a triangular system of linear equations in $N_1(t_1), N_2(t_1), N_3(t_1)$. After solving for the $N_i(t_1)$ we can generate another triangular system of linear equations for $0 < t < t_1$, and solve for the production rates P_1, P_2, and P_3.

A2. Contaminant decays

We now wish to calculate the number of decays Δ_1, Δ_2, and Δ_3 occurring in the time interval $t_{COUNT} = t_3 - t_2$, which do not originate from direct beam production. To this end, it is instructive to examine the previous solutions for $N(t)$, (equations (2) and (4)) to identify terms arising from different production channels. To begin with the trivial case of N_1, we write

$$N_1 = N_1^{beam} \quad , \tag{6a}$$

where N_1^{beam} is the only channel of production of substance 1. The expression for N_2 may be written as

$$N_2 = N_2^{beam} + N_2^{F1} \quad , \tag{6b}$$

where N_2^{F1} is the production of substance 2 by feeding from substance 1 decays. Similarly for N_3

$$N_3 = N_3^{beam} + N_3^{F1} + N_3^{F2} \quad , \tag{6c}$$

where N_3^{F2} is the production of substance 3 by feeding from substance 2 decays, where the production of substance 2 is due to direct beam production. N_3^{F1} is the production of substance 3 by feeding from substance 2 decays where the production of substance 2 is due to substance 1 decays (all of substance 1 is from direct beam production). The next step is to re-write solutions for $N(t)$, identifying the channels on the right hand side of equations (6).

$$N_1(t<t_1)=N_1^{\text{beam}}(t<t_1)=\frac{P_1}{\lambda_1}\left(1-\mathrm{e}^{-\lambda_1 t}\right) \tag{7a,2a}$$

$$N_1(t>t_1)=N_1^{\text{beam}}(t>t_1)=N_1(t_1)\mathrm{e}^{-\lambda_1(t-t_1)} \tag{7b,4a}$$

$$N_2^{\text{beam}}(t<t_1)=\frac{P_2}{\lambda_2}\left(1-\mathrm{e}^{-\lambda_2 t}\right) \tag{8a}$$

$$N_2^{\text{beam}}(t>t_1)=N_2^{\text{beam}}(t_1)\mathrm{e}^{-\lambda_2(t-t_1)} \tag{8b}$$

$$N_2^{\text{F1}}(t<t_1)=\frac{P_1}{\lambda_2}\left(1-\mathrm{e}^{-\lambda_2 t}\right)+\frac{P_1}{(\lambda_2-\lambda_1)}\left(\mathrm{e}^{-\lambda_2 t}-\mathrm{e}^{-\lambda_1 t}\right) \tag{8c}$$

$$N_2^{\text{F1}}(t>t_1)=N_2^{\text{F1}}(t_1)\mathrm{e}^{-\lambda_2(t-t_1)}+\frac{\lambda_1}{(\lambda_2-\lambda_1)}N_1^{\text{beam}}(t_1)\left(\mathrm{e}^{-\lambda_1(t-t_1)}-\mathrm{e}^{-\lambda_2(t-t_1)}\right) \tag{8d}$$

$$N_3^{\text{beam}}(t<t_1)=\frac{P_3}{\lambda_3}\left(1-\mathrm{e}^{-\lambda_3 t}\right) \tag{9a}$$

$$N_3^{\text{beam}}(t>t_1)=N_3^{\text{beam}}(t_1)\mathrm{e}^{-\lambda_3(t-t_1)} \tag{9b}$$

$$N_3^{\text{F2}}(t<t_1)=\frac{P_2}{\lambda_3}\left(1-\mathrm{e}^{-\lambda_3 t}\right)+\frac{P_2}{(\lambda_3-\lambda_2)}\left(\mathrm{e}^{-\lambda_3 t}-\mathrm{e}^{-\lambda_2 t}\right) \tag{9c}$$

$$N_3^{\text{F2}}(t>t_1)=N_3^{\text{F2}}(t_1)\mathrm{e}^{-\lambda_3(t-t_1)}+\frac{\lambda_2}{(\lambda_3-\lambda_2)}N_2^{\text{beam}}(t_1)\left(\mathrm{e}^{-\lambda_2(t-t_1)}-\mathrm{e}^{-\lambda_3(t-t_1)}\right) \tag{9d}$$

$$N_3^{\text{F1}}(t<t_1)=\frac{P_1}{\lambda_3}\left(1-\mathrm{e}^{-\lambda_3 t}\right)+\frac{\lambda_2 P_1}{(\lambda_2-\lambda_1)(\lambda_3-\lambda_1)}\left(\mathrm{e}^{-\lambda_3 t}-\mathrm{e}^{-\lambda_1 t}\right)-\frac{\lambda_1 P_1(\mathrm{e}^{-\lambda_3 t}-\mathrm{e}^{-\lambda_2 t})}{(\lambda_2-\lambda_1)(\lambda_3-\lambda_2)} \tag{9e}$$

$$N_3^{\text{F1}}(t>t_1)=N_3^{\text{F1}}(t_1)\mathrm{e}^{-\lambda_3(t-t_1)}+\frac{\lambda_2}{(\lambda_3-\lambda_2)}N_2^{\text{F1}}(t_1)\left(\mathrm{e}^{-\lambda_2(t-t_1)}-\mathrm{e}^{-\lambda_3(t-t_1)}\right)$$
$$+\frac{\lambda_2\lambda_1}{(\lambda_2-\lambda_1)}N_1^{\text{beam}}(t_1)\left(\frac{\mathrm{e}^{-\lambda_1(t-t_1)}}{(\lambda_3-\lambda_1)}-\frac{\mathrm{e}^{-\lambda_2(t-t_1)}}{(\lambda_3-\lambda_2)}+\frac{(\lambda_2-\lambda_1)\mathrm{e}^{-\lambda_3(t-t_1)}}{(\lambda_3-\lambda_1)(\lambda_3-\lambda_2)}\right) \tag{9f}$$

The number of decays in the time interval t_{COUNT} may also be broken down according to their decay channels.

$$\Delta_1 = \Delta_1^{beam} \quad , \tag{10a}$$

$$\Delta_2 = \Delta_2^{beam} + \Delta_2^{F1} \quad , \tag{10b}$$

$$\Delta_3 = \Delta_3^{beam} + \Delta_3^{F2} + \Delta_3^{F1} \quad . \tag{10c}$$

In particular, we want to find Δ_3^{F2} and Δ_3^{F1}. (Experimentally, Δ_3^{F2} represents the iodine decays due to parent-daughter feeding of the iodine population via $Xe^{beam} \rightarrow I$, and Δ_3^{F1} represents the iodine decays due to grandparent-daughter feeding of the iodine population via $Cs^{beam} \rightarrow Xe \rightarrow I$.) The number of observed decays of substance 3 which originated from substance 2 produced directly by the beam, is given by

$$\Delta_3^{F2} = \int_{t_2}^{t_3} \lambda_3 N_3^{F2}(t > t_1)\mathrm{d}t$$

$$= N_3^{F2}(t_1)\left(e^{-\lambda_3(t_2-t_1)} - e^{-\lambda_3(t_3-t_1)}\right) + \frac{\lambda_3}{(\lambda_3-\lambda_2)} N_2^{beam}(t_1) e^{-\lambda_2(t_2-t_1)}\left(1 - e^{-\lambda_2(t_3-t_2)}\right)$$

$$- \frac{\lambda_2}{(\lambda_3-\lambda_2)} N_2^{beam}(t_1) e^{-\lambda_2(t_2-t_1)}\left(1 - e^{-\lambda_3(t_3-t_2)}\right) \quad . \tag{11}$$

Lastly, the number of observed decays of substance 3 which originated from substance 1 produced directly by the beam, is given by

$$\Delta_3^{F1} = \int_{t_2}^{t_3} \lambda_3 N_3^{F1}(t > t_1)\mathrm{d}t$$

$$= N_3^{F1}(t_1)\left(e^{-\lambda_3(t_2-t_1)} - e^{-\lambda_3(t_3-t_1)}\right)$$

$$+\frac{\lambda_2\lambda_3}{(\lambda_3-\lambda_2)}N_2^{F1}(t_1)\left(\frac{(e^{-\lambda_2(t_2-t_1)}-e^{-\lambda_2(t_3-t_1)})}{\lambda_2}+\frac{(e^{-\lambda_3(t_2-t_1)}-e^{-\lambda_3(t_3-t_1)})}{-\lambda_3}\right)$$

$$+\frac{\lambda_1\lambda_2\lambda_3}{(\lambda_2-\lambda_1)}N_1^{beam}(t_2)\left(\frac{(1-e^{-\lambda_1(t_3-t_2)})}{-\lambda_1(\lambda_3-\lambda_1)}+\frac{(1-e^{-\lambda_2(t_3-t_2)})}{\lambda_2(\lambda_3-\lambda_2)}+\frac{(\lambda_2-\lambda_1)(1-e^{-\lambda_3(t_3-t_2)})}{-\lambda_3(\lambda_3-\lambda_1)(\lambda_3-\lambda_2)}\right). \quad (12)$$

A3. RATE3 program

INPUT	OUTPUT
$\lambda_1, \lambda_2, \lambda_3$	P_1, P_2, P_3
$\Delta_1, \Delta_2, \Delta_3$	$\Delta_2^{F1}, \Delta_3^{F2}, \Delta_3^{F1}$
$t_{COLLECT}$ $(= t_1 - t_0)$	
t_{WAIT} $(= t_2 - t_1)$	
t_{COUNT} $(= t_3 - t_2)$	

As a conservative estimate, we assign an uncertainty of ± 20% to coefficients as calculated by the computer code RATE3. There are several factors that affect our estimate of uncertainty. For example, our formalism used to obtain these results implicitly assumes the level of contaminants - xenon, cesium, and iodine isomer - remained the same over the course of the mass measurement experiment. This assumption considers details such as the ion source operating conditions, resolving power of the separator, and the set of {COLLECT, WAIT, COUNT} cycle times to remain unchanged throughout the experiment. This assumption is not strictly, but only approximately satisfied. The

assignment of an error to the correction must take these assumptions into account. (The measurement cycle times used represent an average over all runs: COLLECT 137.33(3) s, WAIT 7.54(5) s, and COUNT 138.07(2) s.)

In addition there are "fixed" parameters in the RATE3 calculation that are subject to uncertainty; e.g. decay constants, branching ratios, detector efficiency, and counting statistics. The assignment of uncertainty to the coefficients must also include these parameters.

Appendix B.

Energy Calibration of the γ-ray spectra

The γ-ray spectra for the two detectors is set to represent 1 keV per channel over a 2,000 channel spectrum. Ordinarily, a precision calibration of the energy axis is required to the limit of uniquely identifying the iodine activity in the spectra. The mass determination experiment is interested only in changes in intensity of the iodine γ-rays. The discovery of the ^{118m}I isomer transition, approximately 10 keV from its published energy, causes us to perform such a calibration in order to present a new value for the isomer transition energy.

Since the interest in the energy axis is motivated by post-experimental analysis, we do not have data with the usual calibration sources. However, we do have a plethora of other gamma activity in our spectra that have been energetically assigned by other experiments. The precision of this γ-ray energy data is not known as well as the conventional sources, but is adequate for our purposes.

The γ-rays used in the calibration are presented in Table B.1 below. For ease of calculation we assume the errors in the channel positions are negligable with respect to the the errors in the assigned energies. Let the channel data be represented by the variables x_i, and the energy data be represented by $y_i \pm \sigma_i$, such that we determine the coefficients of the linear function $y(x) = a + b\,x$. Following a least-squares fitting procedure [Be69], we minimize χ^2 with respect to each of the coefficients simultaneously. The coefficients of the weighted least-squares fitting are then

$$a = \frac{1}{\Delta}\left(\Sigma\frac{x_i^2}{\sigma_i^2}\Sigma\frac{y_i}{\sigma_i^2} - \Sigma\frac{x_i}{\sigma_i^2}\Sigma\frac{x_i\,y_i}{\sigma_i^2}\right)$$

$$b = \frac{1}{\Delta}\left(\Sigma\frac{1}{\sigma_i^2}\Sigma\frac{x_i\,y_i}{\sigma_i^2} - \Sigma\frac{x_i}{\sigma_i^2}\Sigma\frac{y_i^2}{\sigma_i^2}\right)$$

$$\Delta = \Sigma\frac{1}{\sigma_i^2}\Sigma\frac{x_i^2}{\sigma_i^2} - \left(\Sigma\frac{x_i}{\sigma_i^2}\right)^2$$

$$\chi^2 = \Sigma\left[\frac{1}{\sigma_i^2}(y_i - a - b\,x_i)^2\right]$$

The uncertainties in the coefficients are given by

$$\sigma_a^2 \approx \frac{1}{\Delta}\Sigma\frac{x_i^2}{\sigma_i^2}$$

$$\sigma_b^2 \approx \frac{1}{\Delta}\Sigma\frac{1}{\sigma_i^2}$$

Data points 1. - 10., of Table B.1, are fit to a linear function in order to obtain the so-called global fit. The differences of the real energy data from the calculated global fit are plotted in Fig. B.1. The data fits a straight line well, except in the lower energy region (30 - 300 keV). Since this the energy region of interest for the isomeric transition, we performed a second fit of the data in Table B.1 using only the first four data points, that is, the calibration data in the range 30 - 300 keV. This second fit is the so-called local fit. The difference between the global fit and the local fit is superimposed on Fig B.1.

Table B.1. Raw data and the linear fit for an energy calibration of the channel axis. The channel data are taken from spectra identifications 193, 194, 195 (A = 119, 118, 117 respectively) of the data file IODGAM.SPK.

Data:

	Calibration Source	Channel	Energy
1	^{119}Xe	94.813 ± 0.023	96.0 ± 0.600
2	^{119}Xe	99.322 ± 0.009	100.0 ± 0.600
3	^{119}I	258.171 ± 0.002	247.52 ± 0.040
4	^{117}I	275.209 ± 0.003	274.4 ± 0.200
5	^{117}I	326.549 ± 0.001	325.9 ± 1.
6		512.088 ± 0.007	510.999 ± 0.001
7	^{118}I	878.193 ± 0.045	876.4 ± 0.3
8	^{228}Ac	913.129 ± 0.024	911.1 ± 0.1
9	^{41}Ar	1296.642 ± 0.012	1293.7 ± 0.1
10	^{214}Bi	1768.642 ± 0.079	1764.5 ± 0.1

Linear fit parameters:

$$(Energy = a + b \times Channel)$$

global fit (1 - 10)	$a = 0.070$	± 0.036
	$b = 0.998\,827$	± 0.000 068
local fit (1 - 4)	$a = 1.88$	± 0.66
	$b = 0.990\,2$	± 0.002 6

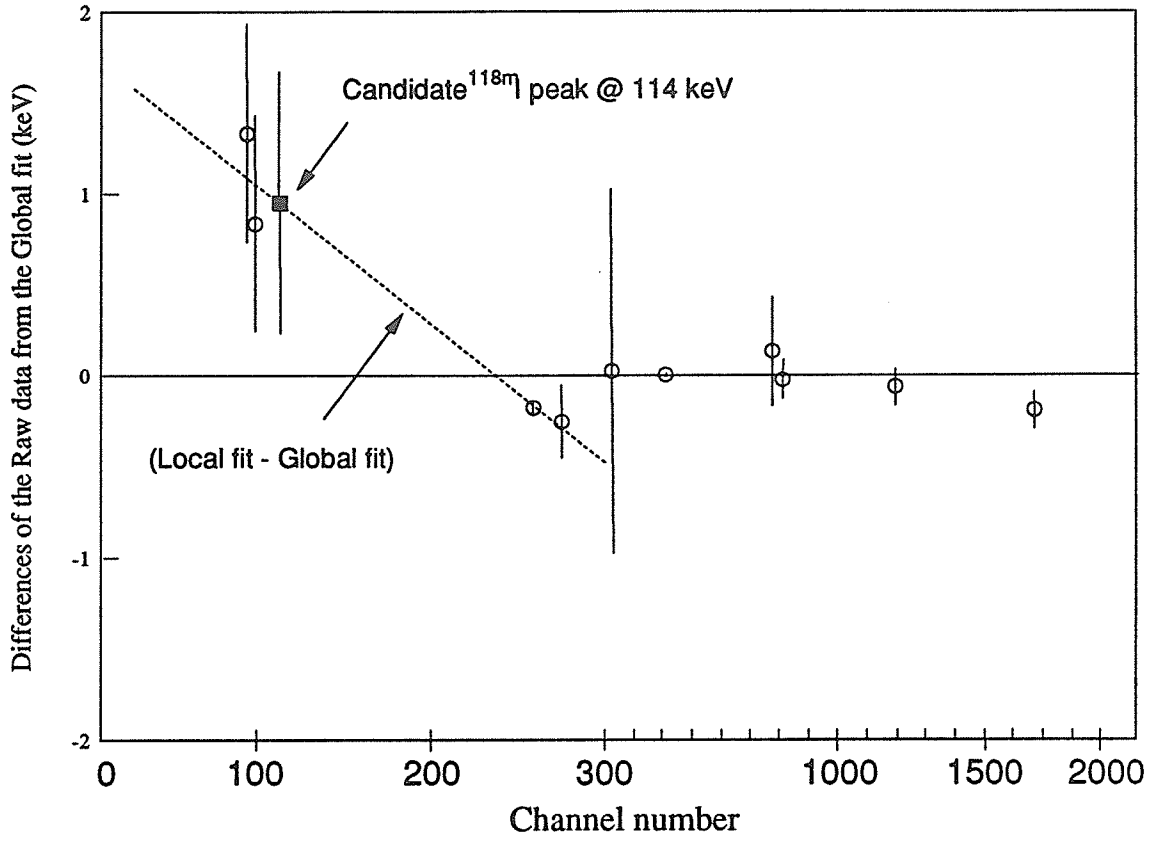

Figure B.1. Differences of the energy calibration data and a linear fit of the data. Actually, two fits are presented here. The first is the fit for energies from 30 - 2000 keV (global fit). The global fit represents the calibration data well in the energy range 300 - 2000 keV (the linear fit passes through almost all the calibration data in this region). Since the region of interest is around channel number 113, we fit the nearby data to a second line. The so-called local fit, for energies in the range 30 - 300 keV, better reflects the precision obtainable in this lower energy regime, given the precision of the calibration data. It is presented in the plot above (dotted line) as the difference *local fit - global fit*. The unknown gamma peak at channel 113.468 ± 0.015 (darkened square) is then assigned an energy of 114.24 ± 0.72 keV.

References

[As20] F.W. Aston, *Philosophical Magazine*, **38**, 709

[Be69] *Data Reduction and Error Analysis for the Physical Sciences*, P.R. Bevington, McGraw-Hill Inc., Toronto © 1969

[Be70] E. Beck, H. Kugler, H. Schrader, R. Stippler, D, Hnatowich, A. Kjelberg, and F. Munnich, *Intern. Conf. Nuclei far from Beta-Stability*, CERN **70-30** 1970, p. 353-360

[Bl36] W. Bleakney, *Am. Phys. Teacher* **4**, 12, (1936).

[Bl78] M. Blann, *University of Rochester Report*, URNSRL - 181 (1978)

[Bl79] J.M. Blair, J. Halverson, W.H. Johnson, Jr., and R. Smith, in *Atomic Masses and Fundamental Masses 6*, J.A. Nolen, Jr. and W. Benenson, eds. ©1980 Plenum Press, New York p. 267

[Bl87] J. Blachot, G. Marguier, *Nucl. Data Sheets*, 50 (1987) 63

[Ca81] J. Camplan, R. Meunier, *Nucl. Instr. and Meth.* **133**, 445 (1981).

[Ch67a] J.Chavet and R. Bernas, *Nucl. Instr. and Meth.* **47**, (1967) 77

[Ch67b] J.Chavet and R. Bernas, *Nucl. Instr. and Meth.* **51**, (1967) 77

[Co87] E.R. Cohen and P. Giacomo, *Physica*, **146A**, (1987) 1-68

[Ep80] M. Ephere, G. Audi, C. Thibault, R. Klapisch, G. Huber, F. Touchard, and H. Wollnik, *Nucl. Phys.*, **A340** (1980) 1

[Gi87] A. Gillibert, W. Mittig, L. Bianchi, A. Cunsolo, B. Fernandez, A. Foti, J. Gastebois, C. Grégoire, Y. Schutz, and C. Stephan *Phys. Lett. B* **192** (1987) 39

[Ha88] P.E. Haustein *At. Data Nucl. Data Tables* **39**, 185 (1988).

[Ha91] E. Hagberg, K.S. Sharma, G.R. Dyck, V.T. Koslowsky, P.P. Unger, J.C. Hardy, H. Schmeing and R.C. Barber, *Nucl. Instrum. and Methods in Phys. Res.*, **B70** (1992) 546

[He83] K. Heyde, P. Van Isacker, M., Waroquier, J.L. Wood, R.A. Meyer, *Phys. Reports*, **102**, Nos. 5 & 6, 1983, 291-393

[Hu83] P. Hungerford, T. von Egidy, H.H. Schmidt, S.A. Kerr, H.G. Borner, E. Monnand, *Zeitschrift fur Physik A*, 313 (1983) 349.

[Ke84] U. Keyser, F. Munnich, B. Pahlmann, M. Graefenstedt, H. Faust, H. Weikard, and B. Pfeiffer, *Proc. 7' th Inter. Conf. Atomic Masses and Fund. Constants, AMCO-7*, (1984) 143

[Ki76] R. Kirchner and E. Roeckl, *Nucl. Instr. and Meth.* 133, 187 (1976).

[Ko91] V.T. Koslowsky, M.J. Watson, E. Hagberg, J.C. Hardy, W.L. Perry, M.G. Steer, H. Schmeing, P.P. Unger and K.S. Sharma, Nucl. *Instrum. and Methods in Phys. Res.*, B70 (1992) 245

[La86] I. Landenbaur-Bellis and H. Bakhru, *Phys. Rev.* 175, 1507 (1968).

[Me72] J.O. Meredith, F.C.G. Southon, R.C. Barber, P.Williams and H.E. Duckworth, *Int. J. Mass Spectrom. Ion Phys.*, 10 (1972/73) 359

[NN92] National Nuclear Data Center, Online Data Service @ 31 August 1992

[Pl79] A. Plochocki, G.M Gowdy, R. Kirchner, O. Klepper, W. Reisdorf, E. Roeckl, P. Tidemand-Petersson, J. Zylicz, U.J. Schrewe, R. Kantus, R.D. Von Dincklage, and W.D. Schmidt-Ott, *Nucl. Phys.*, A332 (1979) 29-40

[Pl81] A. Plochocki, J. Zylicz, R. Kirchner, O. Klepper, E. Roeckl, P. Tidemand-Petersson, I.S. Grant, P. Misaelides, and W.D. Schmidt-Ott, *Phys. Lett.*, 106B (1981) 285-288

[Sc79] D. Schart, R. Kirchner, O. Klepper, W. Reisdorf, E. Roeckl, P. Tidemand-Petersson, G.T. Ewan, E. Hagberg, B. Jonson, S. Mattsson, and G. Nyman, *Nucl. Phys.*, A326 (1979) 65-82

[Sc81] H. Schmeing, J.C. Hardy, E. Hagberg, W.L. Perry, J.S. Wills, J. Camplan and B. Rosenbaum, *Nucl. Instr. and Methods* 133, 187 (1981).

[Sh85] T.L. Shaw, V.R. Green, N.J. Stone, J. Rikovska, P.M. Walker, S. Collins, S.A. Hamada, W.D. Hamilton, I.S. Grant, *Phys. Letters*, 153B, 221 (1985)

[Sh89] K.S. Sharma, H. Schmeing, H.C. Evans, E. Hagberg, J.C. Hardy, and V.T. Koslowsky, *Nucl. Instum. Methods In Phys. Res.* A 275, 123 (1989).

[Sp69] E.H. Spejewski, P.K. Hopke, and F.W. Loeser, Jr., *Phys. Rev.* 186, 1270 (1969).

[Sw31] W.F.G. Swann, *J. Franklin Inst.*, 212 (1931) 439.

[Ta87] T. Tamura, M. Miyano. S. Ohyai, *Nucl. Data Sheets*, 51 (1987) 359

[Wa59] A.H. Wapstra, G.J. Nijgh, and R. van Lieshout, *Nuclear Spectroscopy Tables*, North-Holland Publ. Co., Amsterdam (1959)

[Wa85] A.H. Wapstra, G. Audi, and R. Hoekstra, *Nucl. Phys.*, A432 (1985) 185-362

[Wa88] A.H. Wapstra, G. Audi, and R. Hoekstra, *At. Data Nucl. Data Tables* 39, 281 (1988).

[Wo85] J.M. Wouters, D.J. Vieira, H. Wollnik, H.A. Enge S. Kowalski, and K.L. Brown, *Nucl. Instrum. Methods* A240 (1985) 77

[Wo87] J.M. Wouters, D.J. Vieira, H. Wollnik, G.W. Butler, R.H. Kraus, Jr., and K. Vaziri, *Nucl. Instrum. Methods* B26 (1987) 286-293